THESE DE DOCTORAT
DE
L'UNIVERSITE LILLE 1
PREPAREE AU
SERVICE DE PHYSIQUE DE L'ETAT CONDENSE

ECOLE DOCTORALE N° 072
Ecole doctorale Science pour l'ingénieur Université Lille Nord de France

Spécialité de doctorat : physique

Par
Mme Chloé ROLLAND

Strong coupling Quantum Electrodynamics of a voltage biased Josephson junction

Electrodynamique quantique d'une jonction Josephson polarisée en tension en régime de couplage fort

Réalisée au sein des groupes GNE et Quantronique
SPEC, CEA-Saclay & CNRS

Thèse présentée et soutenue à Saclay, le 14 décembre 2016 :

Composition du Jury :

Dr, Kontos, Takis	Laboratoire Pierre Aigrain	Rapporteur
Dr, Buisson, Olivier	QUEST, Institut Néel, CNRS	Rapporteur
Dr, Gabelli, Julien	Laboratoire de physique des solides	Examinateur
Dr, Seidelin, Signe	PLUM, Institut Néel, CNRS	Examinatrice
Dr, Portier, Fabien	SPEC, CEA Saclay	Directeur de thèse
Dr, Melin, Thierry	Groupe PHYSIQUE, IEMN	Co-directeur de thèse
Dr, Letrucq, Renaud	Luxembourg institue of science and technology	Invité
Prof, Dambrine, Gilles	Groupe PHYSIQUE, IEMN	Invité

A mon Blacky,

Tout bruit ecouté longtemps devient une voix,

V. Hugo, faits et croyance (1840)

1 Remerciements

Comme l'a si justement souligné Fabien lors de ma soutenance, il y a tellement de personnes à remercier qu'un ordre autre que chronologique impliquerait inévitablement des oublis.

Commençons donc par le commencement, je tiens à remercier Renaud Leturcq, pour m'avoir donné envie de faire de la physique avec lui et pour m'avoir accueillie en thèse dans un premier temps. Ces deux années passées avec toi auront été à la fois passionnantes et un excellent tremplin pour la suite de mon parcours.

Je tiens également à remercier tous les habitués de la capsule à l'IEMN pour les déjeuners et les pauses choco animées. Enfin, un immense merci à Florence Senez et Thierry Melin pour m'avoir accompagnée tout au long de ma thèse, et ce même après mon départ, avec une bienveillance incroyable.

Après 18 mois de thèse à Lille, nouveau départ, pour rejoindre le SPEC !

Olivier, merci pour toutes les explications, ta pédagogie et ta joie de vivre. Un immense merci à Marc aussi, pour avoir rythmé toutes ces semaines dans la bonne humeure, de les avoir ponctuées de jurons et d'humour "rire & chanson", quand Chantal faisait des siennes ! Merci aussi pour m'avoir rassurée dans les moments de doute et aidé à comprendre toutes les subtilités des mesures micro-ondes.

Je suis très reconnaissante envers Iouri, le géo-trouve-tout de la manip pour tous les débugs à distance et les programmes Labview construits en deux temps trois mouvements ! Merci aussi de m'avoir initiée aux bobines plates et à la destruction de ponts aériens.

Un grand merci aussi à Benoit, Matthieu et Maelle pour l'ambiance musicale à la cave, mais aussi à Leandro pour les discussions animées, à Camille pour son esprit critique, Audrey, Vivien, Kiddi, Ramiro, et tous ceux que j'oublie pour l'ambiance entre thésards.

Ces années au SPEC auraient également été bien moins riches sans tous les moments passés au contact du groupe Quantro. Que ce soit les blagues d'Hugues, le sourire de Marcelo ou la sagesse et l'humanité de Cristian.

Je tiens en particulier à rendre hommage à:

- Pief, pour ton accueil et ta bienveillance infinie. Merci de m'avoir montré comment fabriquer et observer mes echantillons, mais aussi pour m'avoir fait découvrir les alentours à vélo !
- Denis pour ta générosité et ta disponiblité sans limites ; pour avoir passé tant de temps à traquer les fautes dans ce manuscrit et m'avoir appris que le travail paie !
- Daniel pour ton enthousiasme inébranlable, ton aide précieuse pour la rédaction (et le financement de ma dernière année !) et ton énergie et ta persévérance contagieuses.
- Hélène et Philippe, le soutien que vous m'avez apporté aura contribué grandement a l'aboutissement de cette thèse et j'espère pouvoir profiter encore longtemps de votre compagnie (et de votre four) lors de "soirées pizzas".

Plus généralement, merci à tous pour toutes ces discussions passionnées et passionnantes sur tous types de sujets et merci d'avoir toujours su faire honneur à mes essais culinaires. La patte un brin irrévérencieuse mais si pertinente du groupe me manque déjà.

Quant aux têtes de GNE....

Merci Carlès, pour les discussions de physique, de gastronomie ou des deux à la fois, au bas de l'escalier. Je me souviendrai avec plaisir des remarques ingénieuses, des discussions de physique ou des courses pour visser des atténuateurs avec Patrice. Merci aussi à celles et ceux qui m'ont initiée à la pratique du "jogg", mes jambes se plaignent encore du goût (douteux?) de François pour les côtes.

Plus largement, au sein du laboratoire, je voudrais également remercier Nathalie et Corine pour leur aide avec la partie administrative et également, tout le personnel administratif du SPEC et sa direction qui ont contribué à me rendre la vie facile.

Merci aux compagnons de l'atelier, Dominique, Vincent, et Jean-Claude; à Philippe Forget, Matthieu et Pépé pour leur aide sur le frigo et leurs explications sur son fonctionnement. Merci à Patrice Jacques aussi, pour les joints indiums et la gestion parfaite des approvisionnements en Hélium, sans oublier Pierre Janvier, qui m'a sauvée une ou deux fois quand j'avais besoin d'un peu de rab' à la dernière minute.

Et enfin, le plus important, un immense merci à toi Fabien, d'avoir accepté, un peu à l'aveugle, de m'accueillir ! Merci de m'avoir donné l'opportunité de travailler avec toi sur cette super manip', d'avoir mis ma pugnacité à l'épreuve tout en croyant en ce projet malgré les difficultés. Merci de m'avoir donné un aperçu de ta manière de penser si enthousiaste, donné quelques-unes de ces intuitions dont tu es le spécialiste, d'avoir eu la patience me redonner des explications quand j'en avais besoin et de m'avoir montré que si, même pour un rapide calcul mental, on peut garder quatre décimales de pi.

Parce qu'il y avait aussi une deuxième vie après le labo, merci à mes amies "du poney" d'avoir su me faire rire et atterrir après les journées avec le frigo, à Rossignol aussi qui a subi tous mes déménagements et états d'âme sans trop pouvoir broncher. Merci à mes amies de toujours, Valérie, Sabine, Anne-Marie et à ma cousine Alizée pour m'avoir épaulée, dans les mauvais comme dans les bons moments et pour avoir rendu ces années plus belles. Pour conclure, il paraît que les chiens ne font pas des chats, et je n'aurais probablement pas atterri ici sans la curiosité transmise par mon père et son soutien logistique, alors merci, merci beaucoup.

2 Résumé de la thèse

Dans cette thèse, nous avons étudié le couplage entre le transport de charge dans un conducteur quantique et le rayonnement émis dans son environnement électromagnétique. En effet, le caractère probabiliste du transport électrique dans ce type de conducteurs engendre des fluctuations de courant qui dissipent de l'énergie dans l'environnement sous forme de photons.

Pour caractériser cette interaction, nous avons utilisé un circuit dans lequel une Jonction Josephson polarisée avec une tension continue est couplée à un résonateur micro-onde.

Quand le travail fourni par la source de tension pour faire passer une charge 2e à travers la jonction correspond à un nombre entier de quanta d'énergie dans le résonateur, on observe un courant continu de paires de Cooper associé à l'émission de rayonnement dans le résonateur. Ce rayonnement est ensuite collecté dans une ligne de mesure micro-onde.

En fabriquant des résonateurs hautes impédances basés sur des inductances planaires, nous avons pu atteindre le régime de fort couplage et observer les effets spectaculaires de cette interaction lumière-matière. D'une part, le régime de fort couplage exacerbe les processus multi-photoniques et nous avons observé jusqu'à l'émission simultanée de neuf photons part une paire de Cooper.

De plus en utilisant un montage de type Hanbury-Brown and Twiss, nous avons pu mesurer la statistique des photons émis. Nous avons ainsi démontré que la rétroaction de l'environnement sur la dynamique du transport permet de créer une source non-classique de photons sous-Poissonniens, en accord avec les prédictions théoriques.

3 Summary of the thesis

In this thesis, we investigate the coupling between the charge transport in a quantum conductor and the associated radiation emitted in the electromagnetic environment. In fact, the probabilistic character of the electric transport in this type of conductors generates current fluctuations which dissipate energy in the environment in the form of photons.

To characterize this interaction, we used a circuit in which a Josephson junction is coupled to a microwave resonator and dc voltage biased.

When the work provided by the voltage source to transfer a charge 2e through the junction corresponds to an integer number of energy quanta in the resonator, we observe a dc current of Cooper pairs associated with the emission of radiation in the resonator. This radiation is then collected in a microwave measuring line.

By carefully engineering high impedance resonators based on planar inductances, we were able to reach the strong coupling regime and observed the dramatic effects of this light-matter interaction. Firsr, the strong coupling regime favors multi-photon processes and we observed up to the simultaneous emission of nine photons by a single tunneling Cooper pair.

In addition, using a Hanbury-Brown and Twiss type, we were able to measure the statistics of the emitted photons. We have demonstrated that the feedback of the environment on the transport dynamics creates a non-classical source of antibunched photons, in agreement with the theoretical predictions.

Table of contents

1 Introduction and summary: Quantum Electrodynamics of quantum conductors

A quantum conductor (QC) is a device through which electrons are transmitted while keeping their phase coherence [52][14]. As a consequence, electric transport in quantum conductors can be described from an electronic wave scattering point of view [61]. This implies that the transfer of electrons is probabilistic, which results in quantum current fluctuations called Shot Noise that are directly connected to the charge carrier properties [11].

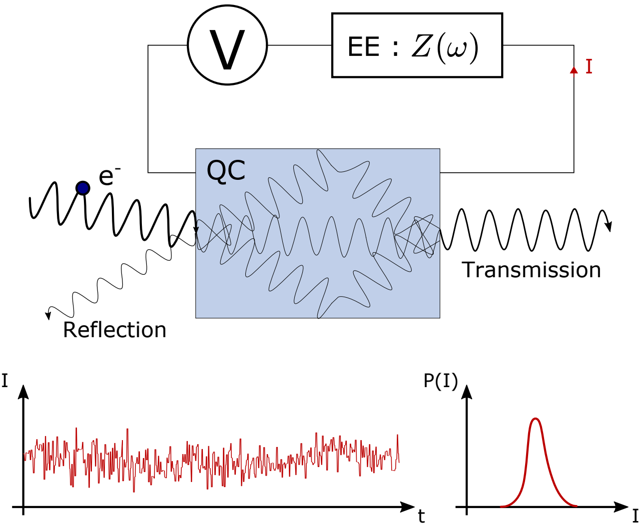

Figure 1. Top : Electron transport across a quantum coherent conductor embedded in an Electromagnetic Environment (EE) and voltage biased.

Bottom : Shot noise current fluctuations and current histogram.

These fluctuations of the current can be characterized by their probability distribution and compared to the statistics of random fluctuations associated to a Markovian process where the currents results from the emission of electrons with a constant probability per unit of time, which leads to Poissonian fluctuations [70]. Due to the fermionic nature of electrons, the Shot noise associated with a normal quantum conductor is Sub-Poissonian, revealing a natural anti-bunching of the transmitted electrons.

When coupled to an electromagnetic environment (EE) these current fluctuations may excite its modes, which leads to inelastic electron tunneling. This phenomenon called Dynamical Coulomb Blockade (DCB)[38] raises two questions:

1. What are the consequences of this QC-EE coupling on the transport properties of the quantum conductor ?

2. What is the connection between the quantum properties of the emitted radiation and those of the charge transferred through the QC? [9][34]

Although a full description is still missing, the first question is fairly well understood for quantum electron transport in tunnel elements in the presence of an electromagnetic environment within the framework of the so called $P(E)$ theory of Dynamical (or environmental) Coulomb Blockade [46].

The latter point was adressed by Beenakker and Schomerus in a pioneering paper [9] who, neglecting the feedback of the electromagnetic environment (i.e. DCB effect) showed that one can use a quantum conductor to imprint the anti-bunched behavior of the electron on photons, which usually obey super Poissonian distribution.

During the last twenty years, experiments mainly focused on the "electronic" part of tunneling, investigating the current through conductors by measuring I(V) characteristics [18][43][22][23][31][19][32][49]. Inspired by these developments and huge progress in low temperature microwave electronics pushed by radio-astronomy, the Quantronics and Nano electronics group of CEA Saclay embarked on a project investigating the quantum properties of photons emitted by a quantum conductor coupled to well designed microwave environments. By carefully engineering the environment, one can obtain a single mode resonator in the microwave range which can be thought as the microwave equivalent of low frequency LC circuits. Its coupling to a superconducting tunnel junction, i.e. a Josephson junction, is then characterized by the coupling constant $r = \pi Z_C / R_Q$, where $R_Q = h/(2e)^2 \simeq 6.5k\Omega$ is the quantum of impedance relevant for superconducting circuits and Z_C is the characeristic impedance of the mode $= \sqrt{L/C}$. If one applies a dc bias voltage V to the junction, Cooper pair inelastically tunnel through the junction, associated with the emission of photons into the resonator provided that the energy of a Cooper pair transferred through the junction $2eV$, corresponds to the energy of an integer number of photons in the resonator. One thus obtains a dc current through the voltage biased junction, associated with the emission of photons into the environement

In 2011, Hofheinz *et al.* [41] performed the first measurement of the current fluctuations in such systems, i.e. photons emitted by the quantum conductor in a resonator. By collecting the emitted radiation and measuring the associated current, they showed that the photon emission rate is in quantitative agreement with the Cooper pair tunneling rate. This proves that Dynamical Coulomb Blockade is imprinted on the emitted photons. However, they were not able to reach the strong coupling regimes ($r \sim 1$), for which recent theories [51][20] predict that successive tunnel events become correlated and show non-classical statistics.

The aim of this thesis was to build high impedance resonators in order to reach this strong coupling regime ($r \sim 1$), where the electromagnetic environment has a strong back-action on the quantum conductor itself. Indeed, we do observe strong Dynamical Coulomb Blockade effects and non-classical radiation.

1 Dynamical Coulomb blockade of a dc biased Josephson junction

The name of Dynamical Coulomb **Blockade** comes from the reduction at low bias voltage of the differential conductance of a tunnel junction embedded in an electromagnetic environment [43][2]. As shown in Fig. 2 : the low bias suppression of inelastic tunneling processes which transfers energy to the environment impedance Z, hence a reduction of the conductance at low bias voltage.

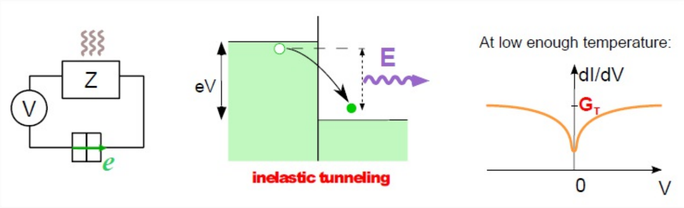

Figure 2. Dynamical Coulomb Blockade in normal tunnel junctions: inelastic tunneling that transfers energy to the environment impedance Z yields a reduction of the number of possible tunneling processes and thus of the conductance at low bias voltage.

In our experiments, we couple a dc biased superconducting tunnel junction to a high impedance single mode resonator. As depicted in Fig. 3, when the potential difference between the two electrodes reaches $2e\,V = k\,h\,f_0$, where f_0 is the resonance frequency of the mode, inelastic tunneling through the junction is allowed, with the simultaneous emission of k photons in the resonator. These photons then leak in the measurement line.

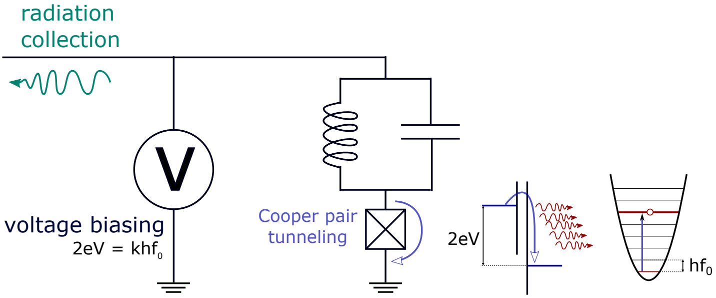

Figure 3. Description of the experiment. A Josephon junction is voltage biased through a single mode resonator. When a Cooper pair tunnels, it emits photons in the resonator which leak in the measurement chain.

Description of the circuit

Our simple circuit consists of :

- a low noise dc voltage source
- a SQUID which is used as a tunable Josephson junction

– a single mode microwave resonator.

The Josephson junction behaves as a pure tunneling element in parallel with its geometric capacitance that participates to the junction's environment. The total Hamiltonian of this system reads

$$H = H_{\mathrm{env}} + H_{\mathrm{el}} + H_T, \tag{1}$$

where H_{env} is the Hamiltonian of the electromagnetic environment, H_T describes the tunneling of Cooper pairs and H_{el} account for the two electrodes.

Our experimental set-up has the following features :

- The electromagnetic environment can be modeled to some extent by a single mode with the Hamiltonian

$$H_{\mathrm{env}} = \hbar\omega_0\left(\hat{a}^\dagger\hat{a} + \frac{1}{2}\right),$$

where a and $a^\dagger$ are respectively photon annihilation and creation operators at the resonance pulsation ω_0. The phase operator of this harmonic oscillator is defined as :$\hat{\varphi}_{\mathrm{env}} = \sqrt{r}\,(\hat{a} + \hat{a}^\dagger)$. Zero-point phase fluctuations are related to the coupling constant

$$r = \frac{\pi Z_C}{R_Q}, \tag{2}$$

with $Z_C = \sqrt{L/C}$ the characteristic impedance of the mode. For a resonator with a finite quality factor, this coupling constant takes the form

$$r = \frac{2}{R_Q}\int_0^\infty \frac{\mathrm{Re}(Z_{\mathrm{env}}(\omega))}{\omega} d\omega. \tag{3}$$

- The sample is at low temperature so that $\hbar\omega_0 \gg k_B T$ and biased below the gap $e\,V \ll 2\Delta = 360\ \mu\mathrm{eV}$. As a consequence, the superconducting electrodes stay in their ground state and one can consider only Cooper pair tunneling. The two electrodes are thus defined by the phase of their macroscopic order parameter $\hat{\varphi}_{r,l}$, a pure electromagnetic degree of freedom.

- The last part of the Hamiltonian H_T describes the tunneling of Cooper pairs between the right and left electrodes

$$H_T = -\frac{E_J}{2}(e^{2i\hat{\varphi}_J} + e^{-2i\hat{\varphi}_J}), \tag{4}$$

where $\hat{\varphi}_J = \hat{\varphi}_l - \hat{\varphi}_r$ is the phase difference accross the junction and E_J the Josephson energy which is related to the normal tunnel resistance R_T and the superconducting gap Δ through the Ambegaokar-Baratoff formulas

$$E_J = \frac{\hbar I_C}{2e} \qquad I_C = \frac{\pi\Delta}{2\mathrm{eR}_T}.$$

According to Kirchhoff's laws, and following the schematic of Fig. 4, the phase $\hat{\varphi}_J$ accross by the Josephon junction is

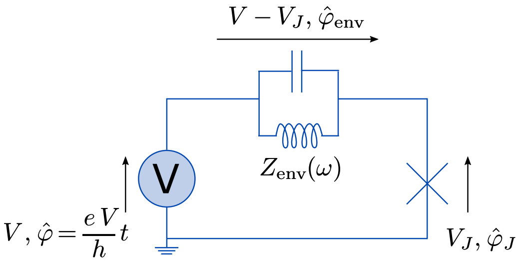

Figure 4. Circuit phase and voltage definitions.

$$\hat{\varphi}_J = \hat{\varphi} + \hat{\varphi}_{\mathrm{env}} = \frac{eV}{h}t + \sqrt{r}(\hat{a} + \hat{a}^\dagger) \tag{5}$$

One notes that the phase across the Josephson junction $\hat{\varphi}_J$ is related to the phase of the electromagnetic environment and that it appears explicitly in the tunnel Hamiltonian H_T. At equilibrium the phase fluctuations of $\hat{\varphi}_J$, from thermal and quantum origin, are stationary and depend on the impedance of the whole circuit as shown by Eq. 5 and Eq. 2.

Josephson relations link these phase fluctuations and charge transfer across the junction through :

$$I = I_C \sin\hat{\varphi}_J$$

$$2e\,V_J = \hbar\dot{\hat{\varphi}}_J.$$

The inelastic tunneling of Cooper pairs in the Coulomb blockade regime is well accounted for by the $P(E)$ theory.

Main results of the $P(E)$ theory in superconducting tunnel junctions

We recall here the main results of the so-called $P(E)$ theory in the superconducting case. The P (E) function describes the probability to release the energy E into a linear electromagnetic environment during a tunnel event [46]. It is valid:

- in a regime where the electrons tunnel independently from each other
- considering that the electromagnetic environment is separable from the electrons onto the electrodes
- considering that the electromagnetic environment, as well as the electrodes of the junction are constantly in the thermal equilibrium it would have in the absence of tunneling

The $P(E)$ function only depends on temperature and on the impedance of the environment. In the case of single resonant mode, it is defined as

$$P(E)=e^{-r}\sum_{k=0}^{\infty}\frac{r^k}{k!}\delta(E-k\hbar\omega_0) \tag{6}$$

where r is the coupling contant defined in Eq. 2.

This function is different from zero only when the energy provided by the voltage bias can be absorbed is a multiple of the quantum of excitation of the resonator, directly reflecting its spectrum.

The global Hamiltonian 1 of the system gives acess to the Cooper pair tunneling rate

$$\Gamma^{\mathrm{Cp}}(V)=\frac{\pi}{2\hbar}E_J^2P'(2\mathrm{eV}),$$

and the associated current accross the junction $I(V)=2e\Gamma^{\mathrm{Cp}}(V)$.

In pratice, when a Josephson junction is biased below the gap and coupled to a single mode resonator, Dynamical Coulomb blockade appears throught dc current peaks thanks to the absorption of energy by the electromagnetic environment as shown in Fig. 5 and already observed in previous experiments [43][41] as shown in Fig. 6

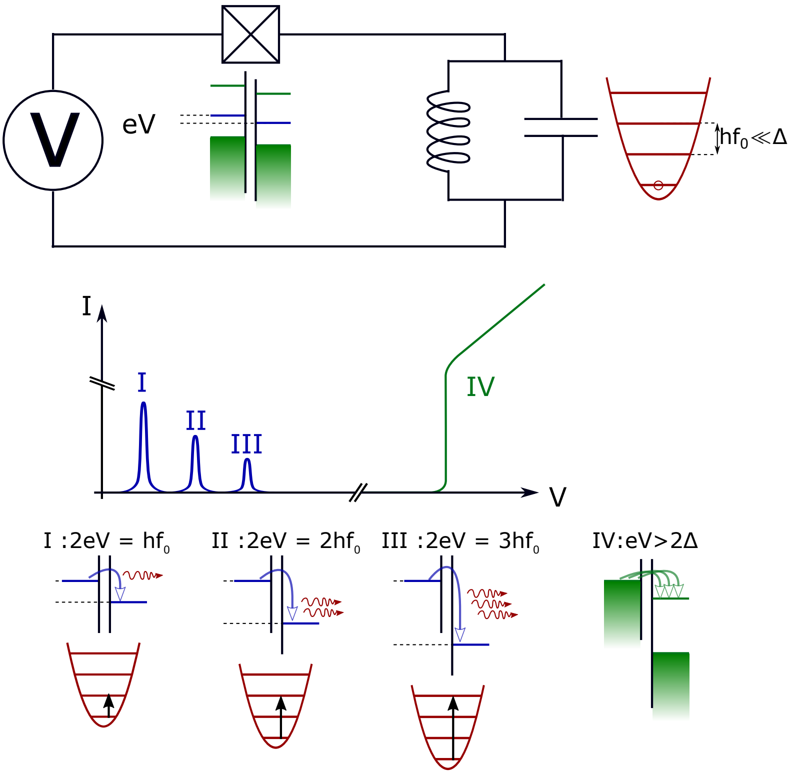

Figure 5. Dynamical Coulomb Blockade in a Josephson junction coupled to a single mode environment. When the junction is biased below the superconducting gap, dc current peaks appear when the energy $2e\,V$ carried by a Cooper pair can be transmitted to the environment through the emission of k photons. the label I, II, and III corresponds to the single, 2 and 3 photon emission peaks. When the Josephson junction is biased above the gap, the external voltage source provide enough energy to break Cooper pairs and quasiparticles can tunnel, the system behaves as a normal tunnel junction (IV).

Without the influence of DCB, one would expect no current peaks when the junction is voltage biased below the superconducting gap $e\,V \ll 2\Delta$. Thanks to inelastic tunneling associated with the emission photons in the environment, current peaks appears when the applied voltage reaches $2e\,V = k\,h\,f_0$ (process I to III in Fig. 5). When the junction is biased above the gap, the system provide enough energy to break Cooper pairs and current is carried by quasiparticles. The system thus behaves as a normal tunnel junction (process IV in Fig. 5). This phenomenon has been experimentally observed as shown by the $I(V)$ curve of Fig. 6.

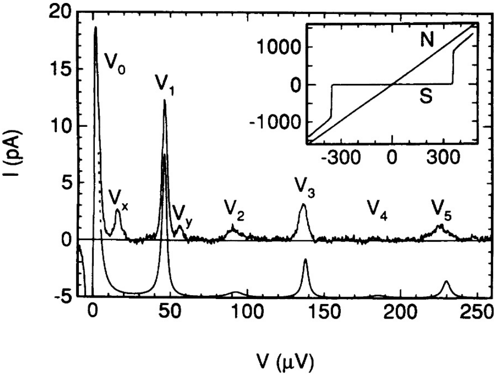

Figure 6. Dynamical Coulomb Blockade of a Josephson junction.

I(V) characteristics of a JJ placed in series with a microwave resonator. Current is allowed when the energy acquired by a Cooper pair tunneling matches one excitation quantum of the resonator. The top curve represents experimental data and the lower one, DCB based theoretical predictions shifted for convenience. The inset on the upper right corner shows quasi-particle current for biases $\mathrm{eV} > 2\Delta$. Reproduced from ref. [43]

Since we are not measuring the current but the emitted radiation, this theory needs to be extended to field quantities (spectrum, high-order correlations) as in [41]. However, this formalism is only valid for low coupling (small impedance resonators).

In the case of finite, but small quantum fluctuations of the phase, it is predicted that the Josephson relations still hold, but with a renormalized Josephson energy E_J [71].

In the strong coupling regime, large phase fluctuations across the resonator can induce correlations between tunnel events. Recent theoretical works [51][50][1][20] have calculated the statistical properties of the emitted radiation.

Building high impedance resonators

Microwave resonators with a characteristic impedances significantly larger than the vacuum impedance ($Z_0 = \sqrt{\mu_0/\varepsilon_0} = 377\Omega$) are difficult to achieve using distributed elements. One must thus design resonators based on lumped elements.

Using planar coil geometries, one can reach inductances up to several tens of nH. In order to stay in our microwave measurement band (4-8 GHz) where $h\ f_0 \gg k_B T$ and far below the gap of the aluminum Josephson junction $h\,f \ll 2\Delta \sim 360\mu\text{eV}$, such an inductance must be coupled to a capacitance of the order of 10 fF, which is already the order of magnitude of the parasitic capacitance to ground.

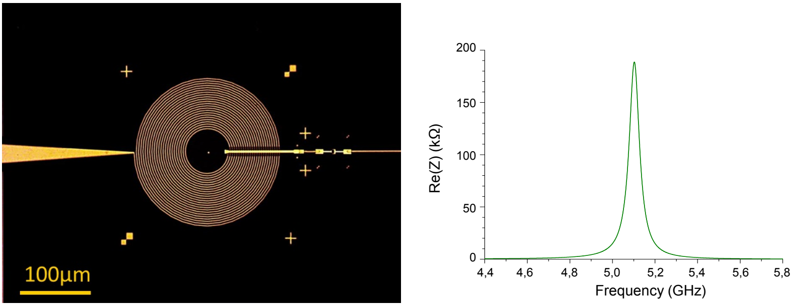

Figure 7. Optical microscope image of the planar coil and simulation results of the resonator impedance.

Using microwave simulation results, we have designed and fabricated planar inductors as shown in Fig. 7 and used their parasitic stray capacitance to achieve characteristic impedances of $2.2\,\mathrm{k}\Omega$, corresponding to a coupling constant $r \simeq 1$.

2 From Cooper pair current to microwave power measurement

This thesis focuses on the photonic side of the Dynamical Coulomb Blockade as we want to measure the statistics of the emitted radiation. A previous experiment of Hofheinz *et al.* [41] has demonstrated quantitative agreement (within less than 5%) between the measurements of the current and the associated power, validating the Dynamical Coulomb Blockade model.

In this experiment, the sample is connected to a bias tee, separating low and high frequency signals. A dc voltage bias is applied to the junction through the low frequency port and the emitted radiation is collected through the high frequency port.

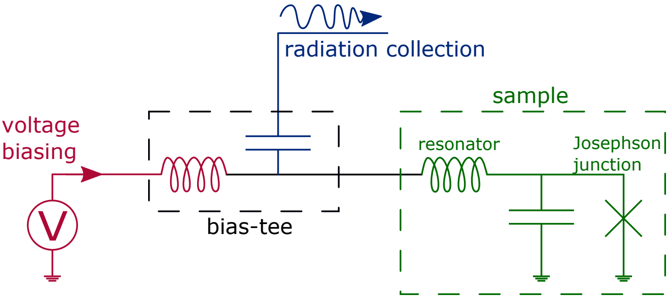

Figure 8. Measurement principle. Using a bias-tee, the sample is dc biased through the low-frequency port and the emitted radiations are collected in the measuremet line, connected to the high frequency port of the bias-tee.

The respective rates of emitted photons Γ^{Ph} and tunneling Cooper pair Γ^{Cp} are

$$\Gamma^{\mathrm{Ph}} = \frac{P}{\hbar\omega_0} \quad \text{and} \quad \Gamma^{\mathrm{Cp}} = \frac{I_{\mathrm{dc}}}{2e}$$

where P is the microwave power emitted by the sample in the measurement chain and I_{dc} is the dc current crossing the Josephson junction. The result of their experiment is shown in Fig. 9.

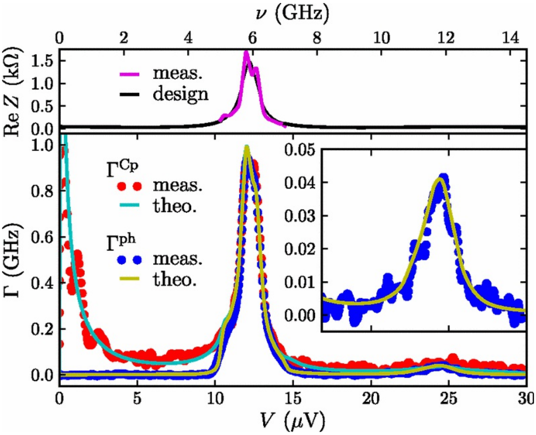

Figure 9. Photon and Cooper pair rates (taken from Hofheinz *et al.* [41]). Top : real part of the impedance seen by the junction, calculated from the resonator geometry (black line) and reconstructed (magenta) from a quasi-particle shot noise measurement. Bottom : Measured Cooper pair Γ^{Cp}(red) and Photon Γ^{ph} (blue) rates extracted from current and microwave power measurements. The first resonance is hit when one CP emits one photon while tunneling : $V = \hbar\omega_0/2e \simeq 12\mu V$. The inset is a zoom on the photon rate at voltage 2eV = $2\hbar\omega_0$, corresponding to the two photon emission process.Solid lines are $P(E)$ theory fits.

In this experiment, the coupling was low ($r = 0.08$) and two-photon processes had much lower rates than the single photon processes as predicted by equation 6. With our high impedance resonators, we probe the strong coupling regime consequences on the emitted photons.

This thesis aims at characterizing the quantum properties of the emitted radiation. Using a similar experimental set-up, we thus simplified the experimental set-up and suppressed the current measurement, assuming that

$$\Gamma^{\mathrm{Ph}} = k\Gamma^{\mathrm{CP}},$$

with k, the number of photons emitted by each Cooper pair.

More over, they showed that extending the standard DCB theory allows to account for the spectral density of the emitted radiation

$$S_{II}(\omega, V) = \frac{2\pi e^2 E_J^2}{\hbar}(P'(\hbar\omega - 2eV) + P'(\hbar\omega + 2eV)),$$

where $P'(2\mathrm{eV} \pm \hbar\omega)$, corresponds to the probability to emit/absorb one photon of energy $\hbar\omega$. This spectrum can be directlty accessed by measuring the spectral density of the emitted radiation.

3 Spectral measurements results

Single photon emission peak : calibration of the environment

Here, we measure the power spectrum of the radiation emitted by the Josephson junction as a function of the bias voltage when each tunneling Cooper pair emits one photon. The Josephson junctions emits photons at the Josephson frequency $f=(2e/h)V$, when this frequency matches the microwave resonance frequency, one observes radiation emitted in the measurment line thanks to inelastic tunneling associated with photon emission.

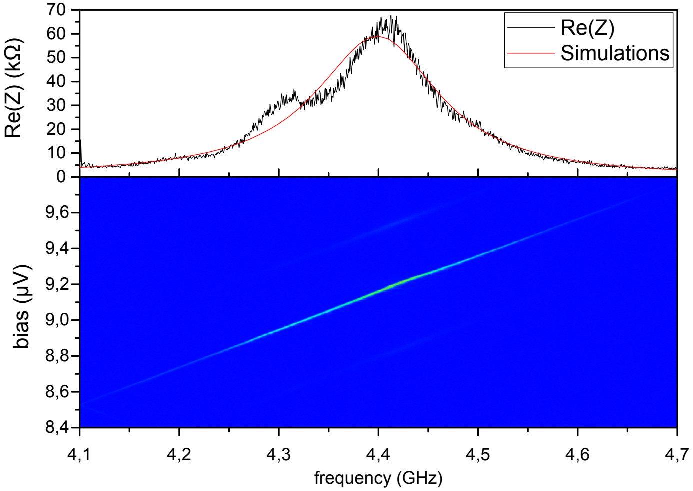

Figure 10. Single photon emission. Bottom : Map of the radiation emitted by the Josephson junction when the voltage is swept around $V=(h/2e)f_0$. Top : Black line : the extracted impedance of the environment assuming that the emitted power follows the $P(E)$ theory as described in section 1.3. Red line : Sonnet simulation of the circuit geometry.

If we consider the process where each Cooper pair emits one photon in the resonator, the emitted power P_1 is

$$P_1 \propto \mathrm{Re}(Z(\nu))\,\delta(\mathrm{eV} - h\nu).$$

As the emitted power is directly proportionnal to the real part of the impedance, by following the line $V = (h/2e)f$ on the map of Fig. 10, we can reconstruct the shape of the electromagnetic environment (top panel). The extension of the $P(E)$ theory predicts an infinitely narrow line but, in practice, its width is finite and determined by the voltage bias noise (5MHz). This measurement of the mode impedance gives us access to the characteristic impedance of the resonator Z_C and thus to the coupling constant r.

Multiphoton emission peaks

Increasing further the voltage bias across the junction, we reach resonance where the bias correponds to the emission of several photons in the environment as shown in the map of Fig. 11.

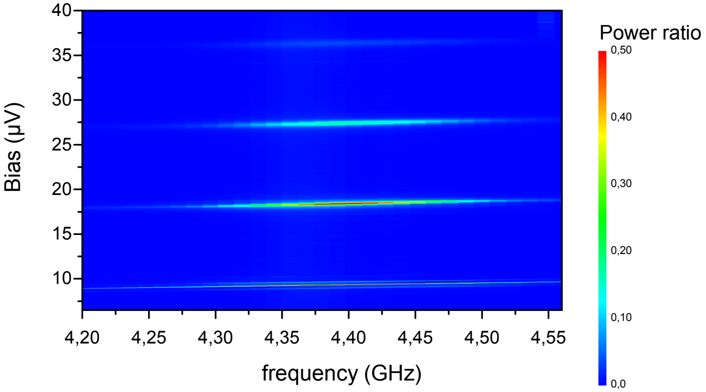

Figure 11. Multiple photon emission map: we measure the power associated to processes where a tunneling Cooper pair emits simultaneously up to 4 photons.

On this map, we can see different peaks corresponding to processes where up to 4 photons are emitted simultaneously. We have then performed measurements integrating the power emitted in the whole resonator.

In previous experiments, peaks corresponding to first and second order processes have been observed [41] and were well described by the $P(E)$ theory. As the coupling factor was rather low ($r < 0.1$), the amplitude of higher order peaks was too low to be observed. Enhancing the coupling, we can now see peaks in the emitted power in Fig. 12, corresponding to processes where a single Cooper pair emits simultaneously up to 9 photons to tunnel.

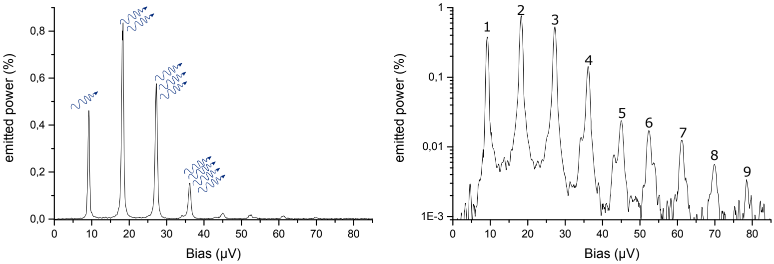

Figure 12. Multiphoton processes. Emitted power integrated over the resonator bandwidth (Linear and logarithmic scales) at the maximum value of E_J.

As described by the $P(E)$ theory, the height of the respective current peaks is supposed to behave according to a Poisson distribution of parameter r [46]. As $\Gamma^{\mathrm{Ph}} = n\Gamma^{\mathrm{CP}}$, the result on power emission should then be:

$$P_n \propto e^{-r}\frac{r^n}{(n-1)!}.$$

Poisson distribution gives a qualitative shape of the peaks for low values of E_J, but it does not quantatively describe the behavior of the peaks at higher Josephson energies of Fig. 12. We nevertheless compare with a fit using the coupling factor r obtained from the measurement of the environment impedance (sec 1.3) as shown in Fig. 13.

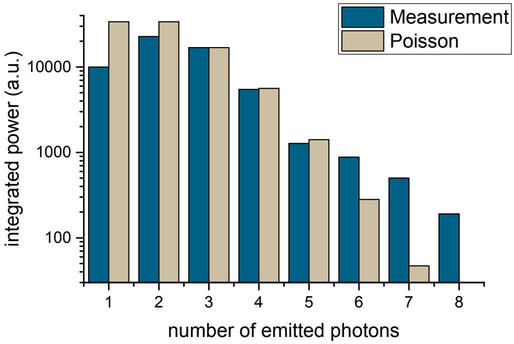

Figure 13. Integrated power of k photon emission (green bars) and fit with the $P(E)$ theory with $r = 1$ and an adjustable scaling factor (grey bars).

We observe that few and several photon processes do not follow the predictions of the $P(E)$ theory.

Breakdown of the E_J^2 scaling rule

We use a SQUID as a tunable Josephson junction. By modulating the flux threading the SQUID, we can tune the coupling between the eletrodes E_J. As the emitted power scales like E_J^2

$$E_J^2(\Phi) = E_{J\,\mathrm{max}}^2 \cos^2\left(\pi\frac{\Phi}{\Phi_0}\right),$$

we expect a sinsuoidal behavior when varying the flux. We observe that this scaling rule does not apply for large values of E_J where 1 and 2 photon processes saturate whereas higher order processes are enhanced, as shown in Fig. 14.

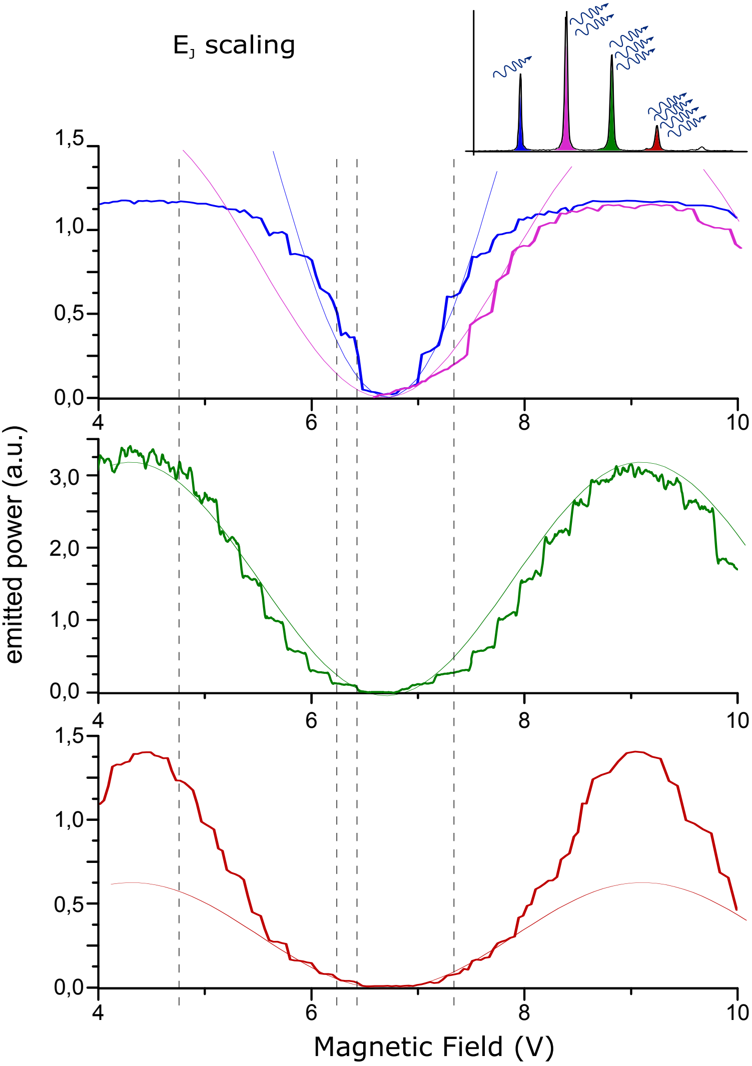

Figure 14. Evolution of the photon emission power with magnetic field for single (blue line), two(pink line), three (green line) and four photon processes (red line). The three photon process is the only one which scales like E_J^2 predictions (black line).

To characterize the statistics of photons emitted sequentially by tunneling Cooper pairs through the Josephson junction, we focus on the single photon regime.

4 Emission of anti-bunched photons

Two papers by Beenakker and Schomerus pointed out the connection between quantum electronic transport and quantum optics [10][9]. These high frequency properties of quantum conductors have recently been extended to Josephson junctions in the Dynamical Coulomb Blockade regime [54][51].

The first steps towards the experimental investigation of these predictions were :

- to detect the photons emitted by a single mode quantum conductor [77][41]
- to develop and validate a Hanbury-Brown-Twiss set-up to probe the statistics of microwave photons emitted by a quantum conductor [78][65]

These two measurements were previously performed in the group in the case of low impedance environment coupled to a tunnel junction. We thus use tools provided by quantum optics and perform a Hong-Ou-Mandel experiment [44] on the emitted radiations [78][33] to extract the second order correlator $g^{(2)}$.

Intensity correlator $g^{(2)}$

The intensity correlator was first used by Hanbury-Brown and Twiss [39] who showed that intensity-intensity correlations yield more precise measurements of star diameter. Radioastronomy essentially focuses on classical thermal radiation sources, but in quantum optics, where a much wider range of sources are characterized, such correlators also probe the non-classical nature of radiation [56].

In order to characterize the statistics of the emitted radiation, we use the intensity-intensity correlator $g^{(2)}$ defined as :

$$g^{(2)}(\tau) = \frac{\langle \hat{I}(t)\,\hat{I}(t+\tau)\rangle}{\langle \hat{I}(t)\rangle^2} = \frac{< \hat{a}^\dagger(t)\hat{a}^\dagger(t+\tau)\hat{a}(t+\tau)\hat{a}(t) >}{< \hat{a}^\dagger \hat{a} >^2}$$

It quantifies correlations between subsequent photon emission with a delay τ. For $\tau = 0$, $g^{(2)}(0)$ measures the probability to emit two photons simultaneously and characterizes radiation statistics:

- if $g^{(2)}(0) < 1$, the field is anti-bunched
- if $g^{(2)}(0) > 1$, the field is bunched
- for a Poissonian process $g^{(2)}(0) = 1$
- for thermal radiation $g^{(2)}(0) = 2$

Hanbury-Brown and Twiss microwave set-up

In order to be able to extract second order correlators, and get rid of any measurement chain influence, the sample is placed in an Hanbury-Brow and Twiss like experiment [78] as described in Fig. 15.

We define the operators a and $a^\dagger$ for photons anihilation and creation and $f_{A/B}, f^\dagger_{A/B}$ for the intrinsic noise contribution of the amplifiers.

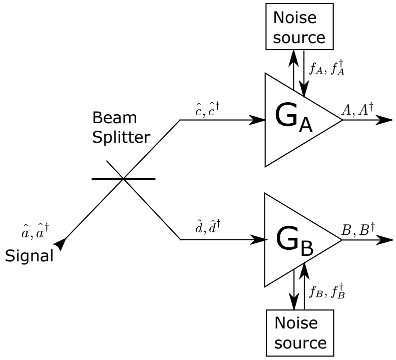

Figure 15. Measurement scheme. Splitting the signal before amplification prevent pollution from the amplifier noise.

Performing correlation measurements at the output of the two lines, one obtains

$$\langle A^\dagger B^\dagger B A\rangle - \langle A^\dagger A\rangle\langle B^\dagger B\rangle = \frac{G_A G_B}{4}(\langle \hat{a}^\dagger \hat{a}^\dagger \hat{a}\hat{a}\rangle - \langle \hat{a}^\dagger \hat{a}\rangle^2)$$

In order to extract $g^{(2)}$, one also needs to measure the contribution of $\langle\hat{a}^\dagger\hat{a}\rangle$

$$\langle A^\dagger A\rangle = \frac{G}{2}\langle\hat{a}^\dagger\hat{a}\rangle + (G-1)^2\langle f_A^\dagger f_A\rangle.$$

The $\langle f_A^\dagger f_A\rangle$ contribution can be easily removed by performing On-off measurements. Performing cross-correlation measurements gives access to the $g^{(2)}(\tau)$ correlator according to

$$g^2(\tau) = \frac{<\hat{a}^\dagger(t)\hat{a}^\dagger(t+\tau)\hat{a}(t+\tau)\hat{a}(t)>}{<\hat{a}^\dagger\hat{a}>^2} = 1 + \frac{<\delta P_A(t).\delta P_B(t+\tau)>}{P_A.P_B}$$

where $\delta P_{A/B}$ is the excess of power due to the signal and $P_{A/B}$ is the total mean power. We have used this microwave Hanbury-Brown and Twiss set-up to show that the photons emitted by a Josephson junction can display non classical properties.

Photon anti-bunching in strong coupling regime

For characteristic impedances of the order of R_Q, sequential tunnelings of Cooper pairs are predicted to be correlated. The tunneling of a Cooper pair shifts the charge across the resonator by $2e$, according to :

$$e^{2i\hat{\varphi}}Q e^{-2i\hat{\varphi}} = Q - 2e$$

Where $\hat{\varphi} = \sqrt{r}(\hat{a}+\hat{a}^\dagger)$. The probability that tunneling occurs is related to the probability to add a photon in the resonator initially populated by N photons

$$P_{N\rightarrow N+1} \propto \left|<N+1\middle|e^{-2i\sqrt{r}(\hat{a}^\dagger+\hat{a})}\middle|N>\right|^2\delta(2eV - h\,f_0)$$

At low temperature, the resonator is empty at equilibrium as vacuum fluctuations of the charge $\delta Q \ll e$. When $2eV = h\ f_0$, one photon is emitted by each CP and we can first consider only transistions from $|0>$ to $|1>$ and from $|1>$ to $|2>$ photons in the resonator.

For strong coupling, i.e. large values of r, $P_{0\rightarrow 1}$ has a finite value but $P_{1\rightarrow 2}$ is strongly reduced and even null for a coupling contant $r=2$ as decribed by Fig. 16.

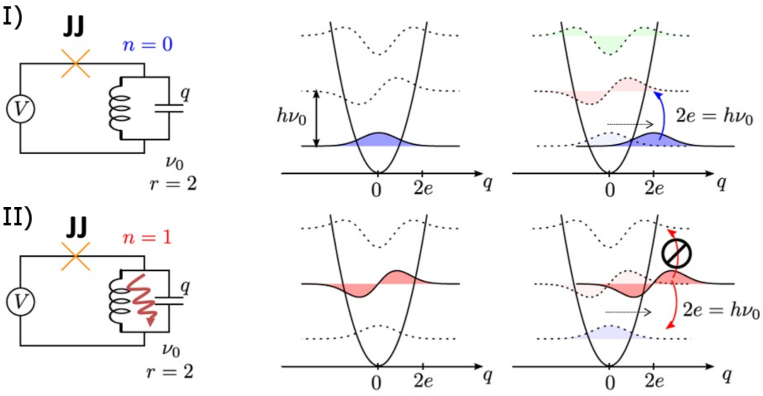

Figure 16. Anti-bunched photon source proposed by Gramich *et al.* [37]. Figure reproduced from ref. [65].

I : assuming the resonator is initally empty, the first tunneling Cooper pair emits one photon and the resonator goes from $|0\rangle$ to $|1\rangle$. The probability of this event is directly related to the overlap between the shifted $|0\rangle$ state wave function and the $|1\rangle$ state wavefunction.

II : The probability for a second Cooper pair to tunnel is then related to the overlap between the shifted $|1\rangle$ state wave function and the $|2\rangle$ state wavefunction. For $r = 2$, this overlap $|\langle 1|e^{-2i\hat{\varphi}}|2\rangle| = 0$. As a consequence, when a Cooper pair tunnels and emits one photon in the resonator, it prevents further photon emission until the first one leaks into the measurement chain. This mechanism generates anti-bunched photons.

As a result, the emission of a first photon in the resonator blocks the inelastic tunneling of a second Cooper pair that would require the emission of a second photon. Due to the finite lifetime in the resonator, the second tunneling event is forbiden until the first photon escape the resonator and leak in the measurement chain. This ideal case correponds to perfect anti-bunched photon source.

For lower coupling constant, the transition $P_{1\to 2}$ is not forbidden but has a vanishing probability. Exploiting this mechanism, we can imprint the anti-bunched behavior of Cooper pairs on emitted photons. Recent theoritical work [51] made predictions for $g^{(2)}(0)$ at low photon occupancy of the resonator in the strong coupling regime

$$g^{(2)}(0) = (1 - {}^{r}\!/_{2})^2$$

where $r = {}^{\pi Z_C}\!/R_Q$ is the coupling constant, as previously described.

Experimental validation

Performing measurement with HBT set-up and high impedance resonator ($r \simeq 1$), we reached $g^{(2)}(0) = 0.28$, meaning non-classical and strongly anti-bunched photons, in agreement with theoretical predicitions. We measure the second order correlator at zero time delay $g^{(2)}(0)$ as a function of the emission rate Γ as shown in Fig. 17.

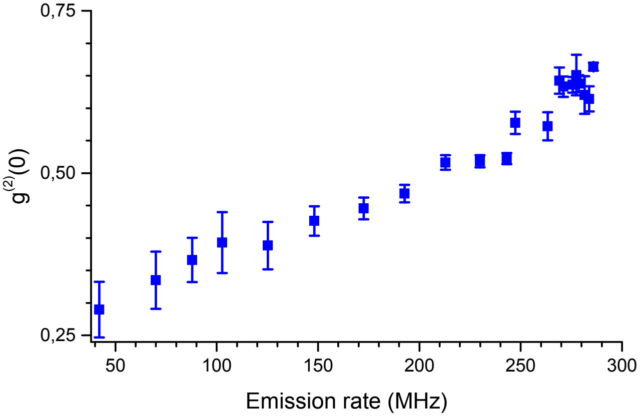

Figure 17. Second order correlator at zero time delay $g^{(2)}(0)$ as a function of the measured emission rate.

One first observes that $g^{(2)}(0)<1$, meaning that the emitted photons have a non-classical behavior and are anti-bunched. Furthermore, the value obtained at the lowest rate is in good agreement with the predicted 0.25 theoretical limit for $r = 1$ [51].

However, this theoretical value is only valid when the resonator is almost empty, i.e. when the assumption that only the transitions $P_{0\rightarrow 1}$ and $P_{1\rightarrow 2}$ are relevant is valid. When the emission rate of the Josephson junction increases, the mean occupation of the resonator increases as well and the initial condition of an empty resonator is no longer fulfilled. Higher order transitions such as $P_{2\rightarrow 3}$ are not identically affected by strong coupling and are not "blocked" identically. As expected, we observe less anti-correlations for high rates and $g^{(2)}(0)$ increases towards 1.

Time resolved correlator : $g^{(2)}(\tau)$

By adding a delay between the two lines, one can also probe the timescale of these anti-correlations, which are supposed to be proportional to the lifetime of a photon in the cavity. This measurement gives access to the timescale of correlations, as predicted in [20]

$$g^{(2)}(\tau) = \left(1 - \frac{r}{2} e^{-\gamma\tau/2}\right)^2, \tag{7}$$

where $\gamma = 2\pi\,\mathrm{FWHM}$ is the photon leakage rate of the resonator.

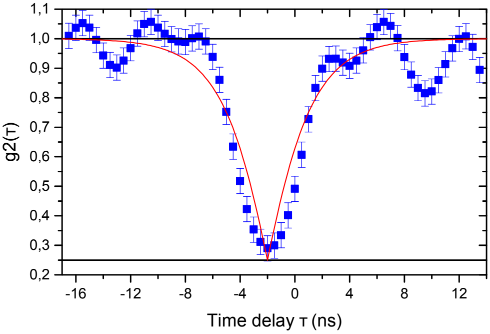

Figure 18. Time resolved evolution of the second order correlation factor $g^{(2)}(\tau)$ (blue) and theoretical fit [20]. The horizontal lines correspond to the theoretical prediction for $g^{(2)}(0) = 0.25$ and the long time limit $g^{(2)}(\tau) = 1$. For this measurement, the emission rate was tune to 42 MHz.

One first observes that the timescale over which $g^{(2)}(\tau)$ reaches one is in consistent with theoretical predictions [20]. The additionnal fluctuations that one can see on Fig. 18 correspond to noise on the correlated signal.

2 Theoretical background & state of the art

In this chapter, we first briefly introduce the main physical ingredients underlying the coupling between quantum conductors (QC) and electromagnetic radiation in their electrical environement. We then describe the physics of electronic transport through a normal tunnel junction (well-known QC), introduce its coupling to radiation, and present first experimental results. In a second part, we move on the case of a Josephson junction, which is at the heart of this work.

Finally, we will focus on the "bright side" of this problem, i.e. on the emission of radiation by the junction. In particular, we show that one can extend the standard theory to account for the spectral density of the emitted radiation. We then present two approaches, which allow us to go beyond this first step and get a full description of the quantum properties of the emitted radiation. This last part especially focus on the strong coupling regime and show that a voltage-biased Josephson junction can be used to emit anti-bunched photons in its environment.

Let's first consider a voltage biased tunnel junction, connected to a resistive environment of impedance $Z(\omega)$ (see Fig. 20). A tunnel junction consists in two electrodes separated by a thin insulating barrier through which electrons can tunnel. This element can be modeled as a capacitance which sees charge accumulation on each electrode in parallel with a pure tunneling element. The charge accumulation on the capacitor plates is due to a continuous collective displacement of the electronic fluid, in which each electron is surrounded by a screening cloud, all electrons thus moving in a highly correlated manner. Such collective charge motion can be described in terms of low-energy collective excitations of the Fermi sea consisting of surface plasmons, which are of bosonic nature. In contrast, in the limit of a low transparency tunnel barrier, charge transport through the pure tunnel element is due to the individual tunneling of genuine electrons, as shown by the schematic of Fig.19.

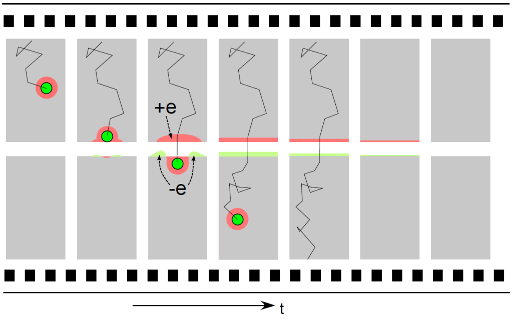

Figure 19. Cartoon description of a tunneling event. At the left, a quasielectron diffuses in the top electrode. The quasielectron is made of an electron (green dot) surrounded by its screening cloud (red surrounding). When it reaches the tunnel barrier, only the bare electron can tunnel, leaving its screening cloud on the first side and rebuilding a new one it in the bottom electrode. This leaves a charge ±e on the plates of the junction's capacitor. This charge is then evacuated in the rest of the circuit to restore equilibrium. We assume that the tunneling time during which the electron crosses the barrier is infinitely short on the timescale of other phenomena. (taken from Philippe Joyez's master lectures and F. Pierre PhD thesis [66])

When an electron tunnels through the barrier, it undresses of its screening charge leaving a $+e$ surface (plasmonic) charge in the first electrode and dresses again on the other side, creating another $-e$ surface charge. Microscopically, tunneling thus consists in the annihilation of a quasiparticle (an electron and its screening cloud) on one side and the creation of another quasiparticle on the other side accompanied by an electromagnetic excitation of charge e that will eventually propagate in the circuit connected to the junction. This description will lead to the Hamiltonian discussed in section 1.2.

The relaxation of this charge excitation in the environment circuit (see Fig 20) will generally lead to Joule dissipation in the real part $\mathrm{Re}[Z(\omega)]$ of the impedance is hardly ever stricly zero at all frequencies), making tunneling an inelastic process [22][38].

At low bias voltages, energy conservation results in a reduction of the phase space for the tunneling quasiparticle and consequently to a reduction of the tunnel conductance at low bias voltages, hence the name of Dynamical Coulomb Blockade (DCB).

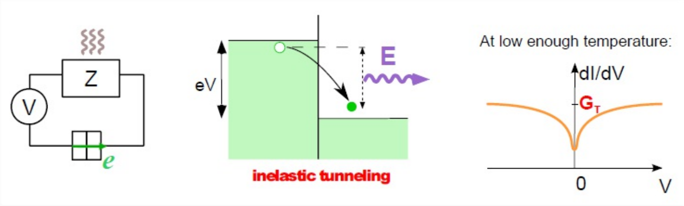

Figure 20. Dynamical Coulomb Blockade : inelastic tunneling that transfers energy to the environment impedance Z yields a reduction of the number of available states, hence a reduction of the conductance at low bias voltage.

This dissipation can be described as the emission of photons in the environment [76]. The higher $\mathrm{Re}[Z(\omega)]$, the stronger the dissipation and the stronger the coupling between the conductor and the environment.

More precisely, we will see that the dimensionless parameter characterizing the strength of this coupling is the characteristic impedance of the environment, divided by the resistance quantum. One can thus increase the coupling between the environment and the conductor by engineering $\mathrm{Re}[Z(\omega)]$. This contrasts with the physics of atoms coupled to radiation, for which the coupling strength is of the order of the fine structure constant and which are thus always in the weak coupling regime. This coupling of tunnel junctions with the electromagnetic environment has been extensively studied over the twenty past years [23][13][22][31][19].

One can ask how this phenomemon affects electron transfer in quantum conductors that are not tunnel junctions. In that case one may use the Landauer-Buttikker-Martin scattering formalism, to describe electrical transport as an electronic wave scattering problem. More specifically, one uses a multi-terminal block description : a phase coherent region is connected to several fermionic reservoirs where the electrons loose their phase coherence and thermalize. These reservoirs are connected to a macroscopic biasing circuit, which impose their electrochemical potential μ_n and temperature T_n, as described by Fig. 21.

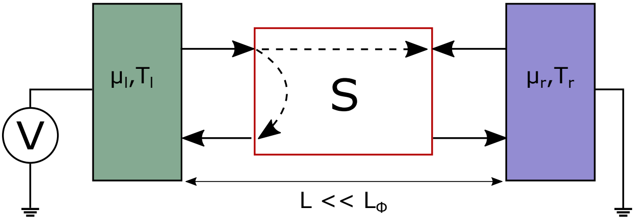

Figure 21. manque Ain A out avec noms des reservoirs!!

Scattering matrix description of a quantum conductor between two reservoirs l, r with chermical potentials $\mu_{r,l}$ and temperature $T_{r,l}$. For each mode of energy $\hbar\omega$, the amplitudes $a_{n,\mathrm{in}}(\omega)$ and $a_{j,\mathrm{out}}(\omega)$ of the inpout and output waves are related by **formule landauer !! scattering matrix**

One then introduces electronic modes at angular frequency ω, propagating toward or from the reservoir n with amplitudes $a_{n,\mathrm{in}}(\omega)$ and $a_{n,\mathrm{out}}(\omega)$, respectively. The current going in/out of the reservoir can be expressed in terms of $a_{n,\mathrm{in}}(\omega)$ and $a_{n,\mathrm{out}}(\omega)$ operators as well. The next step is to describe the phase coherent conductor by a scattering matrix S which allows to express particular $a_{n,\mathrm{in}}$ amplitude as a linear combination of the $a_{j,\mathrm{out}}(\omega)$ amplitudes leaving the other reservoirs j. Using this model, one can then calculate the current through the sample as a function of temperature and of the voltage bias across the conductor.

As in any quantum scattering problem, the transmisssion or reflection of an electron is a probabilistic process. As a consequence, due to the discrete nature of the charge carriers, the current through reservoirs will exhibit quantum current fluctuations called shot noise even for a perfectly quiet potential difference at zero temperature. As any fluctuating current, they will emit radiation into the electromagnetic environment, resulting in inelastic charge tunneling, which affects the dynamics of the charge transfer as already mentionned. This shows that the phenomenon Dynamical Coulomb Blockade is a generic feature of the coupled dynamics of charge transfer and electromagnetic radiations. Let us note finally that the theory of Dynamical Coulomb Blockade originally formulated for tunnel junctions was recently generalized to quantum conductors of arbitrary transmission, provided the dwell time of the electron in the scaterrer is shorter that the inverse of the high frequency cutoff of the environment impedance [1].

In this work we will restrict to the case of tunnel element connected to a linear environment at thermal equilibrium. The theory of Dynamical Coulomb Blockade that describes light-matter interactions in this simple case [46], successfully describes experimental observations on normal and superconducting tunnel junctions [32][23]. Its main results will be presented in sections 1 and 3.

1 Quantum description of the circuit : normal tunnel junction

We now consider a circuit where a normal tunnel element is placed in series with an electromagnetic environment, assumed to be linear, according to a model close to our experimental situation. As shown by Fig. 22 : the tunnel junction is dc voltage-biased through the impedance Z_0.

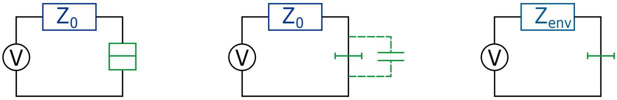

Figure 22. Description of the effective environment impedance. The junction capacitance is included in the environment.

The junction behaves as a tunneling element in parallel with its own geometric capacitance C_J. In the following, we consider the junction as a pure tunnel element only and include its intrinsic capacitance in the environment impedance

$$Z_{\text{env}}(\omega) = \frac{Z_0(\omega)}{1 + \mathrm{jC}_J \omega Z_0(\omega)}.$$

We now give a quantum description of the junction and of this electromagnetic environment. Then, we turn on the coupling, present its consequences and discuss previous experimental results proving that the dissipation induced by the impedance, results in inelastic electron tunneling and suppresses the low bias voltage conductance of the normal tunnel junctions [18][22][31][43].

1.1 Electromagnetic environment

The effective impedance $Z_{\mathrm{env}}(\omega)$ in series with the tunnnel element, see Fig. 22, can always be described as the impedance of a (possibly infinite) series of LC oscillators having different resonant frequencies [16].

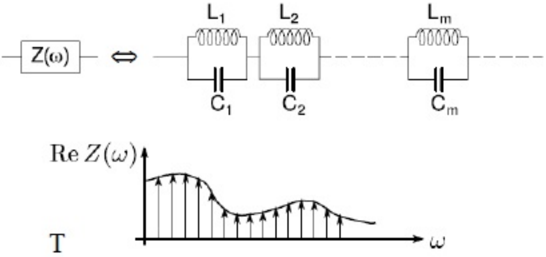

Figure 23. Description of an impedance by a series of LC oscillators.

In our experiments, the environment consist in a single LC mode.

Single mode environment

We first consider a single LC resonator with $\omega_i = \frac{1}{\sqrt{L_i C_i}}$ its resonant frequency and $Z_i = \sqrt{\frac{L_i}{C_i}}$ its impedance. Althought it is a purely reactive element, its dissipative response can be obtained from the Kramers-Kronig relation

$$\mathrm{Re}(Z_i) = \frac{\pi}{2} Z_i \, \omega_i \, \delta(\omega - \omega_i). \tag{8}$$

Second quantization of this LC resonator yields the Hamiltonian

$$H_0 = \hbar \omega_i \left(a_i^\dagger a_i + \frac{1}{2} \right),$$

where a_i and $a_i^\dagger$ are respectively bosonic annihilation and creation operators for an excitation of pulsation ω_i. The conjugated variable of the charge is a flux that, normalized by $\hbar/e$, takes the form of the phase

$$\varphi_i = \sqrt{r_i}(a_i + a_i^\dagger), \tag{9}$$

where

$$r_i = \frac{\pi}{R_K}\sqrt{\frac{L_{\omega_i}}{C_{\omega_i}}}$$

corresponds to the amplitude of the zero-point fluctuations of the phase of the oscillator.

To describe an environment consisiting in a finite number of LC oscillators, we sum over all the N discrete resonator frequencies and get the following Hamiltonian

$$H_{\mathrm{env}} = \sum_{i=0}^{N} \hbar\omega_i\left(a_i^{\dagger}a_i + \frac{1}{2}\right), \tag{10}$$

the characteristic impedance

$$Z_C = \sum_{i=0}^{N} Z_i\delta(\omega - \omega_i) = \frac{2}{\pi}\int_0^{\infty}\frac{\mathrm{Re}(Z(\omega))}{\omega}d\omega, \tag{11}$$

and the corresponding zero point fluctuations of the phase

$$r = \frac{\pi Z_C}{R_K}. \tag{12}$$

1.2 Normal tunnel junction

In the absence of tunneling, a tunnel junction behaves like a capacitor, the applied bias simply shifts the electronic cloud from the ion lattice. This capacitive behavior, is separated from the pure tunnel element behavior and included in the environment, as previously mentionned.

For the following, we introduce the definition of the phase φ_J as the time integral of voltage across the junction

$$\varphi_J = \frac{e}{\hbar}\int_{-\infty}^{t}\mathrm{dt}\, V_J, \tag{13}$$

The consequences of tunneling, due to the quantum nature of the junction will be addressed in the following

Quantum treatment of the electrodes

In the absence of tunnel coupling, the electrons in the electrodes can be described as free neutral Landau particles [62] distributed in energy ε with a continuous density of states $\rho(\varepsilon)$ around the Fermi level μ. The Hamiltonian of these electrodes is

$$H_e = H_r + H_l \tag{14}$$

with

$$H_{l,r} = \int d\varepsilon_{l,r}\rho_{l,r}(\varepsilon_{l,r})\varepsilon_{l,r}\, c_{l,r}\, c^{\dagger}_{l,r} \tag{15}$$

where c (resp. $c^{\dagger}$) corresponds to quasi-particle annihilation (resp. creation) operators, and the indices r and l comes to differentiate right and left electrodes.

Tunneling

The description of tunneling given in the introduction leads to the following Hamiltonian :

$$H_T = T_e\Theta + h.c, \tag{16}$$

where

$$\Theta = \sum_{l,r} \mathcal{T}_{\mathrm{lr}}\, c_l\, c^{\dagger}_r \tag{17}$$

describes the tunneling of a quasiparticle from the left to the right electrode, where $\mathcal{T}_{l,r}$ is the tunnel matrix element corresponding to the tunneling of a quasiparticle. The operator

$$T_e = e^{-j\varphi_J} \tag{18}$$

transfers an elementary charge e through the environment impedance and verifies

$$e^{i\varphi_J}Q\, e^{-i\varphi_J} = Q - e.$$

1.3 Full circuit : From charge tunneling to environmental fluctuations

Embedding a tunnel junction with its electromagnetic environment in a circuit, yields the total Hamiltonian

$$H = H_{\text{env}} + H_e + H_T \tag{19}$$

where H_{env}, H_e and H_T are given by Eqs. 10, 14-15 and 16, respectively. H_T is treated below as a perturbation yielding the so called P(E) theory.

According to Kirchhoff's laws, and following the schematic of Fig. 24 , the phase φ_J accross the junction is

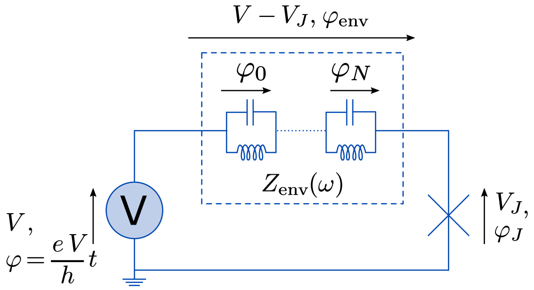

Figure 24. Circuit phase and voltage definitions.

$$\varphi_J = \varphi_{\text{ext}} + \sum \varphi_i = \frac{\text{eV}}{h} t + \sum \varphi_i$$

and appears directly in the Hamiltonian describing electron tunneling H_T. This points out that phase fluctuations across the junction are strongly correlated to those in the electromagnetic environment, and as a consequence, to its impedance.

When an electron tunnels through the barrier, its screening charge remains in the lead, producing an excess of charge e, which has to relax generating fluctuations of the "Fermi" liquid. The collective motion of the electronic cloud is called a plasmon and corresponds to an excitation of the modes of the electromagnetic environment.

The charge-light interaction in this single mode model is quantified by the ratio between the charging energy E_C of the tunnel capacitance and the energy carried by one electromagnetic excitation or photon of pulsation ω_0:

$$r = \frac{E_C}{\hbar\omega_0} = \frac{\pi Z_C}{R_{K/Q}} \tag{20}$$

This coupling constant also compares the characteristic impedance of the environment to R_K or R_Q, quantum of resistance for a normal or superconducting channel.

2 Theoretical description of Dynamical Coulomb Blockade in a normal tunnel junction

The theory of Dynamical Coulomb Blockade was derived in references [23][32]. It is well summarized in chapter 2 [46] of *Single Charge Tunneling* [38].

2.1 Expression of the tunneling current

If we first make the assumption of a perfect dc voltage bias, the tunneling of a charge does not have any influence on latter processes by environmental fluctuations contribution which are associated with T_e. Here, we recall main results developped in details in Olivier Parlavecchio's PhD Thesis [65] using the $P(E)$ theory of DCB.

The current operator associated with the tunneling of electron through the junction is

$$I = \dot{q} = \frac{dH}{d\varphi_J} = -j\frac{e}{\hbar}(T - T^\dagger) \tag{21}$$

where q is the charge that has tunneled through the junction. This equation, takes into account forward and backward tunneling.

A perturbative treatment at the lowest order of the tunneling Hamiltonian gives [69] for the mean current value

$$\langle I(t)\rangle = -\frac{e}{\hbar^2}\int_{-\infty}^{t} dt' \langle [H_T(t'), I_0(t)]\rangle, \tag{22}$$

where $\langle ... \rangle = \mathrm{Tr}[\rho_0 ...]$, with ρ_0 the total unperturbed density matrix. By defining $\tau = t - t'$ and using tunneling operators one gets

$$\langle I(t)\rangle = -\frac{j}{\hbar}\int_{-\infty}^{t} d\tau(\langle T(t)T^{\dagger}(t+\tau)\rangle - \langle T^{\dagger}(t)T(t+\tau)\rangle) + h.c. \tag{23}$$

One sees here that the average current is directly related to the correlators $\langle T(t)T^{\dagger}(t+\tau)\rangle$ and $\langle T^{\dagger}(t)T(t+\tau)\rangle$.

By assuming that there is initially no correlations between the electrodes and the environment, meaning that the system is at thermal equilibrium, one gets

$$\langle T(t)T^{\dagger}(t+\tau)\rangle = \langle \Theta(t)\Theta^{\dagger}(t+\tau)\rangle_{\mathrm{el}} \langle e^{-j\varphi(t)} e^{j\varphi(t+\tau)}\rangle_{\mathrm{env}}\, e^{j\frac{eV}{\hbar}\tau} \tag{24}$$

$$\langle T^{\dagger}(t)T(t+\tau)\rangle = \langle \Theta^{\dagger}(t)\Theta(t+\tau)\rangle_{\mathrm{el}} \langle e^{j\varphi(t)} e^{-j\varphi(t+\tau)}\rangle_{\mathrm{env}}\, e^{-j\frac{eV}{\hbar}\tau} \tag{25}$$

where $\langle \mathcal{O}\rangle_{\mathrm{el/env}} = \mathrm{Tr}[\rho_{\mathrm{el/env}}\mathcal{O}]$ denote averaging over the electronic and environmental degrees of freedom, assumed to be uncoupled. One then computes these three factors separately.

- The Fourier transform of $\langle \Theta^{\dagger}(t)\Theta(t+\tau)\rangle$ describes the ability of the electrodes to absorb the energy $h\,f = \epsilon_r - \epsilon_l$ from the voltage source [49][65], as shown in Fig. 25.

$$\gamma(h\,f) = \frac{1}{h}\int_{-\infty}^{+\infty} d\tau\, \langle \Theta^{\dagger}(t)\Theta(t+\tau)\rangle_{\mathrm{el}}\, e^{-2jf\tau} \tag{26}$$

$$\gamma(h\,f) = |\mathcal{T}|^2 \int_{-\infty}^{+\infty} d\epsilon_l\, \rho_l(\epsilon_l)\rho_r(\epsilon_l + h\,f) f_{\beta}(\epsilon_l)[1 - f_{\beta}(\epsilon_l + h\,f)] \tag{27}$$

where $f_{\beta}(E)$ is the Fermi function, $\epsilon_{l,r}$ are the energies of the right and left electrodes and $\mu_{l,r}$ corresponds to the chemical potential of the electrodes.

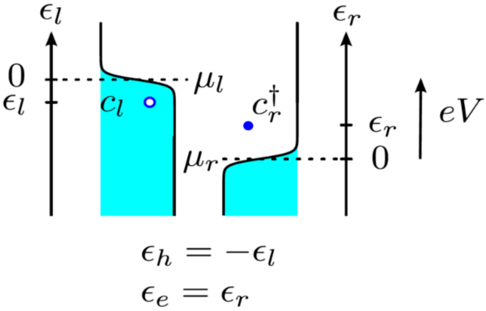

Figure 25. Description of tunneling rates at finite-temperature. When an electron tunnels, a quasi-electron is destroyed on one electrode (left) at the energy ϵ_l, and a quasi-electron is created on the other one (right), at the energy ϵ_r. The left electrode is excited with respect to thermal state by the appearance of an hole with the energy ϵ_h = -ϵ_l, and the right electrode is excited with an electron with energy ϵ_l = -ϵ_r. The pictured process is inelastic because the energy difference E, defined as eV = ϵ_h + ϵ_e + E is sent to an other degree of freedom. Reproduced from Ref. [65].

This quasi-particle correlators $\langle\Theta(t)\Theta^\dagger(t+\tau)\rangle_{\rm el}$ looks very similar to the Landauer-Büttiker formalism [15], where there is no correlator for the electromagnetic environment, and where the voltage source is included into the energy of the Fermi seas.

In the situation where the densities of state are flat over the energy scales $k_B T$ and eV , they can be factorized in equation 27, which leads to

$$\gamma(h\,f) = |\mathcal{T}|^2 \rho_l \rho_r \frac{h\,f}{1 - e^{-\beta f}}.$$

This function is represented in Fig.25b). Note that there is a direct relation between the microscopic parameters ρ_l, ρ_r, $|T|^2$ and the tunnel resistance of the junction [4]

$$R_N = \frac{\hbar}{2\pi e^2 \rho_l \rho_r |\mathcal{T}|^2}.$$

One can calculate the other correlator of equation 25 and get the same result, which is expected, as long as electron hole symmetry is preserved.

- The second factor $\langle e^{-j\varphi_t} e^{j\varphi_{t+\tau}}\rangle$ in the correlator $\langle T(t)T^\dagger(t+\tau)\rangle$ (see Eqs. 24-25) describes the dynamics of the electrodynamic field at thermal equilibrium. We define the phase-correlation function

$$J(\tau) = \langle [\varphi(t) - \varphi(0)]\, \varphi(0)\rangle. \tag{28}$$

This function $J(\tau)$ is obtained from the impedance of the electromagnetic environment by

$$J(\tau) = 2\int_0^{+\infty} \frac{d\,\omega}{\omega} \frac{\mathrm{Re}(Z(\omega))}{R_K} \left\{ \coth\left(\frac{\beta\hbar\omega}{2}\right)[\cos(\omega\tau) - 1] - j\sin(\omega\tau)\right\}. \tag{29}$$

Since, for a linear electromagnetic environment at thermal equilibrium, fluctuations of the phase are Gaussian and stationary, it yields to the following relation [46]

$$\langle e^{j\varphi(t+\tau)}\, e^{-j\varphi(t)}\rangle_{\mathrm{env}} = e^{J(\tau)}$$

The physical meaning of this correlator appears when Fourier transformed. The function $P(E)$ thus defined as [46]

$$P(E) = \frac{1}{h}\int_{-\infty}^{\infty} d\tau\, \langle e^{j\varphi(t)}\, e^{-j\varphi(t+\tau)}\rangle_{\mathrm{env}}\, e^{-j\omega\tau}, \tag{30}$$

$$P(E) = \frac{1}{h}\int_{-\infty}^{\infty} d\tau \exp\left[J(\tau) + \frac{i}{\hbar}E\tau\right] \tag{31}$$

is actually the analogous of $\gamma(f)$ for the environment, i.e. it is the density probability that the electromagnetic environment absorbs the energy E when a charge tunnels through the barrier.

One can demonstrate in the same way that the other phase correlator $\langle T(t)T^\dagger(t+\tau)\rangle$ gives $\langle e^{-j\varphi(t+\tau)}\, e^{j\varphi(t)}\rangle_{\mathrm{env},t} = e^{J(\tau)}$ and thus the same FT and function $P(E)$.

One can now access the average current using γ and $P(E)$ functions according to the equation 23.

$$\langle I(V)\rangle = \frac{2\pi e}{\hbar}[\gamma \otimes P(eV) - \gamma \otimes P(-eV)] \tag{32}$$

where $\otimes$ is the convolution product which "counts" all the possible ways to split the energy $\pm eV$ between the electronic degrees of freedom and electromagnetic ones of the environment. The current results from the difference between forward and backward tunneling. This equation 32 is one of the main results of the $P(E)$ theory.

Its predictions have been probed in numerous works over the past thirty years [22][31][19][43][13].

2.2 Current fluctuations : Shot Noise

The shot noise quantum fluctuations of the current, directly connected to the charge carrier properties, provide a direct link between DCB and current noise.

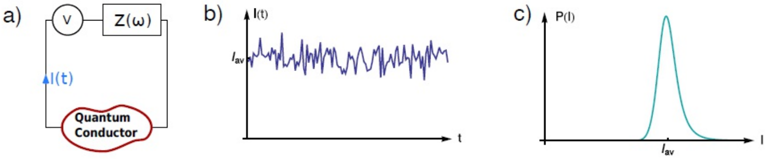

Figure 26. Current noise induced by charge tunneling and associated probability density function.

Indeed, one finds that the Joule dissipation associated to shot noise current fluctuations is identical to the energy transferred to the environment by inelastic tunneling in the $P(E)$ theory.

The power spectral density, and higher order correlation functions can provide a quantitative description of the dynamics of the charge transfer. As we will describe it in chapter 4, the current noise power spectral density can be accessed in our measurement set-up.

Current probability density function

In classical statistics, the moments of a function are obtained using a generating function. For quantum systems, that are defined by the so called Full Counting Statistics. If one precisely knows the model of a circuit, one can access all the moments of the current distribution. These moments may reflect the dynamics of electrons in the quantum conductor, but most often they are only fixed by the response time (inverse bandwidth) of the measurement apparatus which is generally much slower. Furthermore, the higher the order the more difficult to observe because of several noise sources influence.

Hopefully, as any linear electromagnetic environment is supposed to experience Gaussian fluctuations, it is then fully described only by its first and second moments (as all the following moments are products of them). The properties of the current crossing the tunnel junction are then given by

$\langle \hat{I}(t) \rangle$: mean current is proportional to the tunneling rate

$\langle \hat{I}(t)\hat{I}(t+\tau) \rangle$: variance / central moment characterize photon statistics

Correlator and power spectral density

One characterizes the current noise by its power spectral density given by Wiener-Khintchine theorem

$$S_i^0(\omega) = 2\int_{-\infty}^{\infty} d\tau [\langle I(t)\, I(t+\tau) \rangle - \langle I(t)^2 \rangle_t] e^{j\omega\tau}, \tag{33}$$

$$S_i^0(\omega) = h\sum_{\alpha}^{\gamma} \rho_{\alpha\alpha} \langle |\langle \alpha | \hat{I} | \gamma \rangle|^2 \rangle_t\, \delta(\hbar\omega + (E_\gamma - E_\alpha)). \tag{34}$$

The fluctuations of currents at a given frequency appear as the probability to jump from the eigenstate $|\alpha\rangle$ to an eigenstate $|\gamma\rangle$ which have an energy difference $\hbar\omega$,

- for positive energy difference, $E_\alpha < E_\gamma$, meaning that the energy $\hbar\omega$ is released by the conductor into the environment,
- for negative energy difference, $E_\gamma < E_\alpha$, meaning that the conductor absorbs the energy $\hbar\omega$ from its environment.

As the system is at thermal equilibrium, we have $\langle I(t)^2\rangle_t = 0$ at zero perturbation order [65]. We can now calculate the first part of the correlator

$$\langle I(t)\, I(t+\tau)\rangle = \left(\frac{e}{\hbar}\right)^2 [\langle T^\dagger(t) T(t+\tau)\rangle + \langle T(t) T^\dagger(t+\tau)\rangle],$$

and the associated noise spectral density

$$S_i^0(\omega) = 2\left(\frac{e}{\hbar}\right)^2 \int_{-\infty}^{\infty} d\tau [\langle T^\dagger(t) T(t+\tau)\rangle + \langle T(t) T^\dagger(t+\tau)\rangle] e^{j\omega\tau}. \tag{35}$$

Using the previous equations, one gets

$$S_i^0(\omega, V) = \frac{4\pi e^2}{\hbar} [\gamma \otimes P(eV - \hbar\omega) + \gamma \otimes P(-eV - \hbar\omega)]. \tag{36}$$

This result is quite similar to the dc current of equation 32. However, the power spectral density takes the possibility to emit/absorb the energy $\hbar\omega$ in/from the environment. Furthermore, both tunneling directions have a positive contribution on the noise, current fluctuations are thus symmetric with respect to the voltage.

2.3 Case of a single mode environment

A finite quality factor resonator can be treated, to a certain extent, as a single mode. This case is relatively simple and will illustrate the first experiments performed using normal tunnel junction. Furthermore, it will lead to the experiment of this thesis when applied to the case of a superconducting tunnel junction.

The treatment of discrete modes in the perturbation formalism described above requires that the environment remains in a thermal state. We use superconducting resonators which are dissipationless, but couple them to a $50\,\Omega$ detection chain. This measurement line acts as a relaxation channel, giving photons of the resonator a finite lifetime. The resonator should be treated, more rigorously, as a continuum of modes [56].

We consider here an environment made of one single parallel LC-resonator having the resonant frequency $f_0 = \left(2\pi\sqrt{\mathrm{LC}}\right)^{-1}$ and whose real part of its impedance is

$$\mathrm{Re}(Z(\omega)) = \frac{\pi^2}{C}[\delta(\omega-\omega_0)+\delta(\omega+\omega_0)].$$

Using equations 29 and 31, the $P(E)$ function take the form [46]

$$\begin{aligned} P(E) = \exp\left[-r\coth\left(\frac{\hbar\omega}{2k_BT}\right)\right] \\ \sum_{k=-\infty}^{\infty} I_k\left[\frac{r}{\sinh\left(\frac{\hbar\omega}{2k_BT}\right)}\right]\exp\left(\frac{k\hbar\omega}{2k_BT}\right)\delta(E-k\hbar\omega) \end{aligned} \tag{37}$$

where r is the coupling parameter (see Eq. 20) and I_k is the modified Bessel function of order k. As shown by the factor $\delta(E-k\hbar\omega)$, the resonator can only exchange quantum of energy $\hbar\omega$.

At low temperature $k_BT \ll \hbar\omega$, this expression takes a very simple form

$$P(E) = e^{-r}\sum_{k=0}^{\infty}\frac{r^k}{k!}\delta(E-k\,\hbar\omega). \tag{38}$$

The factor $e^{-r}r^k/k!$ is the probability to produce k oscillator quanta in a single tunnel event, transfering an energy $k\,\hbar\omega$ into the environment. One can note that it follows a Poisson distribution of parameter r. In addition, the larger the coupling r, the stronger the multi-photon probability as shown in Fig. 29.

Experimental evidence

Experiments in the case of a single mode environment are reported in [43][64].

The data of O. Parlavecchio in [64][65] are shown in Fig. 27. The steps in the differential conductance dI(V)/dV are the signature of the opening of new tunneling channels, corresponding to production of 1, 2 or 3 excitations in the resonator during a single tunnel event.

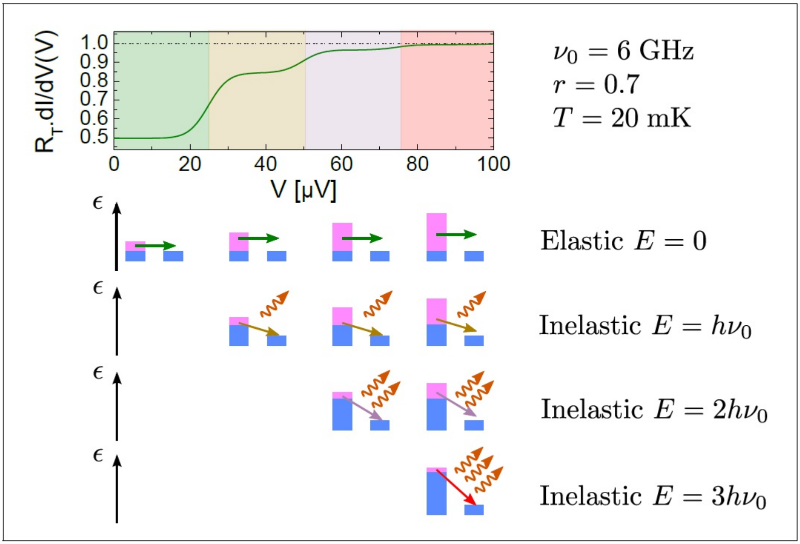

Figure 27. Conductance of a normal tunnel junction coupled to a single mode as a function of bias voltage. Theoretical plot of the $\mathrm{dI}(V)/\mathrm{dV}$ curve extracted from equation 37, for a normal tunnel junction coupled to a single mode with resonant frequency $f_0 = 6$ GHz and a characteristic impedance $Z_C = 1.4 k\Omega$ at 20 mK.

The conductance has step-like features caused by inelastic tunneling of electrons. For small voltage $\mathrm{eV} < \mathrm{hf}_0$ only the elastic process is allowed. Each time $e\,V$ is a multiple of $h\,f_0$, another inelastic process is activated: the electron can tunnel releasing n photons at frequency f_0. The pink part of the density of states of the electrodes represents the energy window in which are located eligible electrons for the tunneling.Reproduced from Olivier Parlavecchio's PhD Thesis.

3 Dynamical Coulomb Blockade in Josephson junctions

We now consider the case of a tunnel junction between superconducting electrodes, i.e. a Josephson junction.

3.1 Description of the Josephson junction :

In this thesis, we consider superconducting metallic electrodes that are described by the BCS theory of superconductivity [8]. In these metals, a phonon-mediated electron-electron interaction provokes an instability of the normal state Fermi sea below a critical temperature, which results in a phase transition to a new state, *the superconducting state*. The superconducting ground state consists of a coherent superposition of time-reversed electronic states and is characterized by a complex order parameter $\Delta = |\Delta| e^{i\varphi}$; it can be roughly seen as a "superfluid condensate of Cooper pairs" which can support dissipationless currents. In a Josephson junction one can observe manifestations of both the modulus and the phase of the order parameter, as we now explain.

The excitation spectrum of the superconductor has a well defined energy gap of $|\Delta|$ between this ground state and the exited states, known as the (Bogoliubov) quasiparticle states [12]. This energy gap, predicted by BCS theory, is an intrinsic property of the material ($\Delta_{\mathrm{Al}} = 180 \mu\mathrm{eV}$). Breaking a Cooper pair yields two Bogoliubov quasi-particle excitations, which requires adding a minimum energy of 2Δ to the system. As a consequence, for a Josephson junction connected to a voltage source V such that $|V| < 2|\Delta| / e$, the voltage source does not deliver enough energy to break Cooper pairs in a tunnel event and consequently no quasiparticle current can flow. This threshold for quasiparticle tunneling is clearly visible in the $I - V$ characteristics of a Josephson junction, were the current sharply rises at $|V| \geqslant 2|\Delta| / e$.

Furthermore, since the order parameter describes a "fluid" of charged particules, its phase is a degree of freedom which is linked to the electromagnetism of the system. Indeed, Josephson pointed out that the phase difference between the two electrodes is simply related to the potential difference applied to the junction according to

$$\frac{d}{dt}(\varphi_l - \varphi_r) = \frac{2e\,V_J}{\hbar} \tag{39}$$

where V_J, is the bias between the two electrodes [1]. Introducing the shorthand notation $\varphi_J = \varphi_l - \varphi_r$, the above equation leads to

$$\varphi_J(t) = \frac{1}{\varphi_0}\int_{-\infty}^{t} V_J(\tau)d\tau \tag{40}$$

with $\varphi_0 = \frac{\hbar}{2e}$, the reduced flux quantum. This equation is the same we have used in the normal case (Eq. 13) except for the change $e \rightarrow 2e$ signaling that now charge carriers are Cooper pairs.

By combining electron tunneling with the BCS Hamiltonian of the junction electrodes, Josephson demonstrated in 1963 that the tunneling of Cooper pairs is non vanishing and can be described as an interaction term [48]

$$H_J = -E_J \cos\varphi_J. \tag{41}$$

The energy E_J is called the Josephson energy; it is related to the normal state resistance R_N of the junction through

$$E_J = \pi\Delta\,\frac{R_Q}{R_N}, \tag{42}$$

where $R_Q = h/(2e)^2$ is the superconducting quantum of impedance.

As the phase difference across the junction is conjugated with the number of Cooper pairs N_J transfered through it, the Josephson Hamiltonian can be rewritten as

$$H_J = \frac{-E_J}{2}[T_J + T_J^\dagger] \tag{43}$$

where $T_J = e^{-i\varphi_J}$ transfers a charge $2e$ through the tunnel junction.

---

[1] This relation assumes we use a gauge where the vector potential $\boldsymbol{A}$ is constant. Otherwise there is an extra term $V_J = \frac{\hbar}{2e}\frac{\partial}{\partial t}(\varphi_r - \varphi_l) + \int_l^r \frac{\partial \boldsymbol{A}}{\partial t} d\ell$.

Finally, the supercurrent through the junction is given by $I = 2e\frac{d}{dt}N_J$ can be obtained from the Hamilton relation, yielding

$$I = 2e\frac{d}{d\varphi_J}H_J = I_C \sin\varphi_J,$$

where the maximum supercurrent I_C that can flow through the junction[3] is related to the Josephson energy

$$E_J = \frac{\hbar I_C}{2e}. \tag{44}$$

3.2 The Josephson junction and its electromagnetic environment

When a Josephson junction is inserted in a circuit and biased at subgap voltages, quasiparticle tunneling can be disregraded and the total Hamiltonian of the system can be written as[2]

$$H = H_{\text{env}} + H_J \tag{45}$$

where H_J is the Effective Josephson Hamiltonian given above (Eqs. 41 or 43) and H_{env} describes the rest of the circuit. As in the normal case, the Kirchhoff's loop relation relevant for Fig. 24 allows to write the phase across the Josephson junction as

$$\varphi_J = \frac{2eV}{\hbar}t + \varphi_{\text{env}},$$

where φ_{env} is the phase accross the environment, which contains zero point phase fluctuations. For low coupling constants, these fluctuations are small and do not influence the behavior of the junction and the usual textbook description of Josephson junctions applies. In this thesis we consider the opposite case where the electromagnetic environment exhibits sizeable zero point phase fluctuations whose effect cannot be disregarded.

By making use of the Josephson Hamiltonian 43, the Hamiltonian 45 of a Josephson junction with an environment appears as a simplified

---

[2] One should be aware that in this derivation of the effective Hamiltonian 41, 43, Josephson did not take into account the environment of the junction. One can show however that its form is quite generally valid in presence of an environment, with simply a renormalization of the Josephson energy.

version of the Hamiltonian 19 describing a normal junction in its environment: all the quasiparticle degrees of freedom are now absent. The differences are that (i) H_J describes now tunneling of Cooper pairs instead of electron (that is with a charge twice larger), and (ii) that during a tunnel event the whole work provided by the source can only go into excitations of the environment. Given the similarity of the Hamiltonians, this case can also be accounted for by $P(E)$ theory presented above which was originally derived for normal state junctions. In the following we do not rederive all the corresponding results: they are obtained in a similar way, albeit simpler, than in the normal case.

3.3 $P(E)$ theory for a Josephson junction coupled to a single-mode environment: Incoherent Cooper pair tunneling rate

From now on, we consider a Josephson junction coupled to a single mode of frequency $f_0 \ll \Delta / h$ (See Fig. 28) and we restrict to cases where it is always biased well within the superconducting gap $0 < eV \ll 2\Delta$ (we assume $V \neq 0$ in order to exclude the supercurrent branch of the junction).

From the discussion in the preceeding section we see that Cooper pairs will be able to tunnel through the junction only when $2eV = k\,h\,f_0$, i.e. when the electrostatic energy $2eV$ of a single pair creates an integer number k of excitations in the resonator[3]. One sees that in Josephson junctions, Dynamical Coulomb blockade appears through dc current peaks below the gap, thanks to the **absorption** of energy by the resonant environment. These processes are depicted in Fig. 28 and were first investigated in the experiment of Holst *et al.* [43].

Main results of the $P(E)$ theory for a Josephson junction

The coupling constant r is now

$$r = \pi \frac{Z_C}{R_Q},$$

where $R_Q = 4e^2/h \sim 6.4 k\Omega$.

---

[3] We assume the superconducting electrodes are and remain in their ground state in these processes, which is valid as long as $k_B T \ll \Delta$.

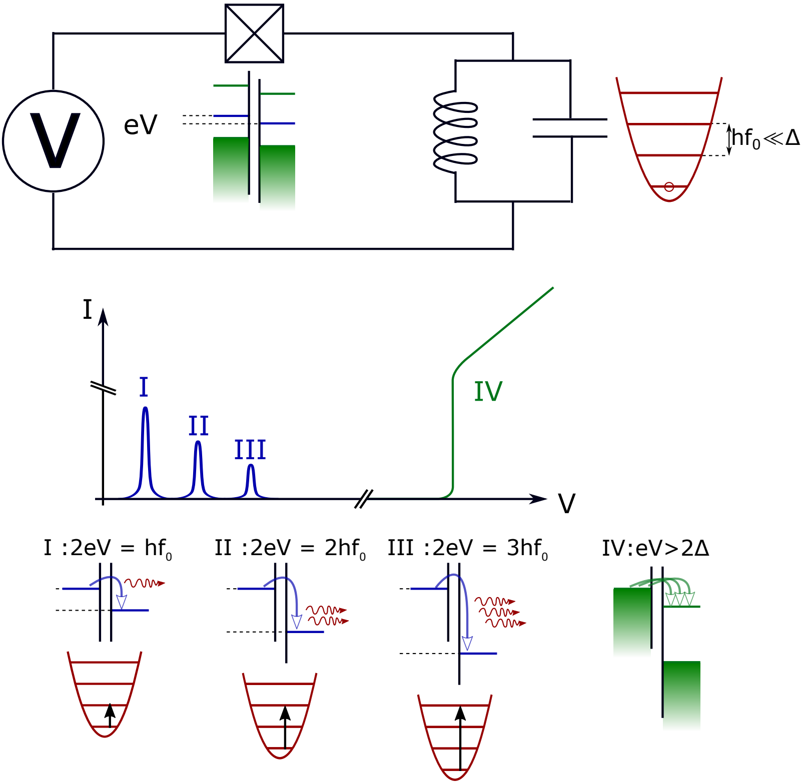

Figure 28. Dynamical Coulomb Blockade consequences for a Josephson junction. For biases eV $<2\Delta$, the superconductor remains in its ground state (blue). There is no additionnal degree of freedom due to quasiparticles in the lead and Cooper pair carry dc current when inelastic tunneling is allowed by $P(E)$, i.e. when 2eV$=k\,\hbar\omega_0$ (I to III).

For biases eV $>2\Delta$, we provide enough energy to the system to break Cooper pairs (green). The current is then carried by quasiparticles and we observe the behavior of normal tunnel junction in Shot Noise regime.

By perturbatively treating Josephson equations 41 in E_J, one obtains the Cooper pair current

$$I(V)=\frac{\pi e E_J^2}{\hbar}(P'(2eV)-P'(-2eV)). \tag{46}$$

In this equation, the previously defined $P(E)$ function becomes $P'(E)$, describing the probability density for a **Cooper pair** to cross the junction while emitting photons with a total energy E in the environment.

At low temperature, $k_BT \ll eV$, $P'(-2eV) \sim 0$ and backward tunneling can be neglected in $I(V)$ calculation and the equation 46 takes the simple form

$$I(V) = \frac{\pi e E_J^2}{\hbar} P'(2eV).$$

The pair current directly measures $P'(E)$.For quantum systems, that are defined by the so called Full Counting Statistics.

In the case of a single mode whose real part of the impedance was defined by equation 8, one gets :

$$P'(E) = \frac{1}{2\pi\hbar} \int_{-\infty}^{\infty} dt e^{4J(t) + \frac{i}{\hbar}\mathrm{Et}} = e^{-r} \sum_{k=0}^{N} \frac{r^k}{k!} \delta(E - k\hbar\omega). \tag{47}$$

The current peak amplitudes are proportionnal to E_J^2 and scale as a Poisson function of parameter r. The figure 29 shows the relative height of the current peaks for different coupling constant r.

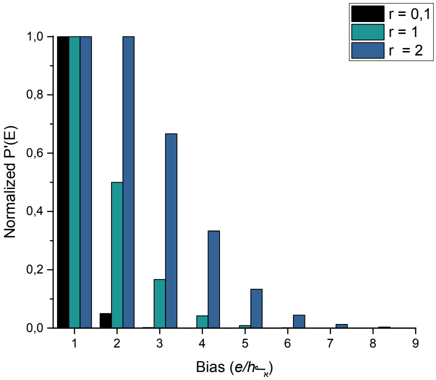

Figure 29. Current peak amplitudes predicted for a Josephson junction coupled to a single mode environment for different values of the coupling factor r, normalized to the amplitude of the single photon peak.

Noise current spectrum

The previous expression of the current noise correlator (see equation 35), yields to

$$S_{II}(\omega) = \frac{1}{2\pi}\int_{-\infty}^{\infty} \frac{2e^2}{\hbar^2} E_J^2 \cos\left(\frac{2e\,Vt}{\hbar}\right) e^{J(t)} e^{i\omega t} d\,t, \qquad (48)$$

from which, using equation 47, one derives the voltage dependent current noise spectrum

$$S_{II}(\omega, V) = \frac{2\pi e^2 E_J^2}{\hbar}(P'(k\,\hbar\omega + 2eV) + P'(k\,\hbar\omega - 2eV)), \qquad (49)$$

where $P'(2e\,V \pm k\hbar\omega)$ corresponds to the probability to emit/absorb k photon of energy $\hbar\omega$.

Note, however, that this perturbative treatment is only valid when the system stays at thermal equilibrium. It is not compatible with correlations between successive events (tunneling of CP), a regime that we will also probe. This situation will be addressed in section 3.4.

First experimental evidence

In this first experiment[43], the current-voltage characteristics of a small capacitance Josephson junction coupled to a coplanar waveguide microwave resonator was measured in both superconducting and normal cases as shown in Fig. 30.

The resonator had several resonant modes with angular frequencies

$$\omega_{2p+1} = (2p+1)\,\omega_0$$

with ω_0 the fundamental mode angular frequency. In addition, the modes had a low impedance,

$$\left(\sqrt{\frac{L}{C}}\right)_n \ll R_{Q,K}.$$

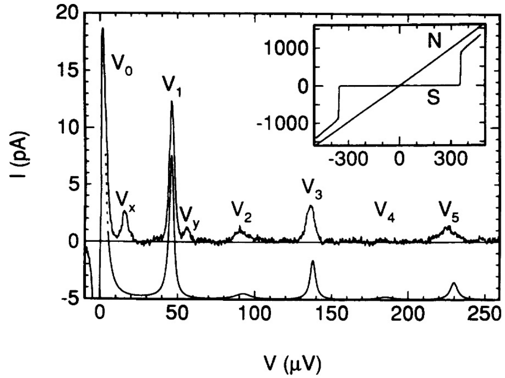

Figure 30. Dynamical Coulomb Blockade of a Josephson junction.

I(V) characteristics of a JJ placed in series with a microwave resonator. Current is allowed when the energy acquired by a Cooper pair tunneling matches one excitation quantum of the resonator. The top curve represents experimental data and the lower one, DCB based theoretical predictions, shifted downwards for clarity. The inset on the upper right corner shows quasi-particle current for biases eV $> 2\Delta$. Reproduced from ref. [43]

Using the toolbox provided by dynamical Coulomb blockade theory [46], Holst and coworkers described quantitatively the current peaks height as being due to the process by which a Cooper pair tunnels by emitting a photon, "the basic process of the theory of the effect of the electromagnetic environment on tunneling".

In their experiment, the coupling of the junction to the modes was indeed so weak that the current peak amplitude was well described by the first order expression of $P(E)$. This is not the case of our samples and the consequences of strong coupling regime are addressed in the following section.

3.4 Strong coupling regime : beyond $P(E)$ theory

The strong coupling regime of a Josephson junction to a single mode environment, $r \sim 1$ is an unchartered regime of quantum optics. In particular, it enhances multi-photon processes and yields to a non-classical behavior of the emitted radiation as shown in section 5.

According to equation 9, the coupling factor r is proportionnal to zero point fluctuations (ZPF) of the phase $\langle \delta\varphi^2 \rangle$. Reaching the strong coupling corresponds to a transition from a well defined phase across the junction to a regime where the tunneling charge is well defined.

This regime may question the validity of the hypothesis made by the $P(E)$ theory :

- The $P(E)$ theory is a perturbative treatment in E_J that assumes either low emission rates or low coupling [46] so that

  $$E_J P(E) \ll 1.$$

  This implies that the dc current through the junction is much smaller than its critical current $I_{\mathrm{DC}} \ll I_C$. As a consequence, multi Cooper-pair processes, where several Cooper pairs tunnel simultaneously to emit one or several photons can be neglected. When the impedance of the environment increases, the value of $P(E)$ increases as well, as shown by equation 47 and the perturbative approach at the lowest order is only valid for very low values of E_J.

- In addition, this treatment assumes that the environment stays at thermal equilibrium, meaning that the resonator has time to relax between subsequent tunneling events. The back-action of the excitations produced by the dynamical Coulomb blockade on the conductor itself is thus neglected, suppressing the memory of the previous tunneling events.

  This assumption can be invalidated, leading to correlations between subsequent tunneling events [50]. As an example, in the two photon emission regime ($2e\ V = 2h\ f_0$), stimulated emission yields to a parametric resonance of the resonator above a certain threshold energy

  $$E_{JT} = \hbar\Gamma \frac{Z_C}{R_Q}.$$

- Moreover the $P(E)$ theory derivation assumes that the admittance $Y(\omega)$ of the junction itself is negligible and does not affect the environment

  $$Y(\omega) \ll [Z_{\mathrm{env}}(\omega)]^{-1}.$$

> When this condition is no longer fulfilled, the perturbative approach is not valid and the problem must be solved self-consistently [50].

Even if the $P(E)$ theory and its extensions provide a meaningful framework for describing the strong coupling regime investigated in this thesis, a quantitative treatment beyond its scope may be required.

4 Relation between tunneling and emitted radiations

The experiment of Holst *et al.* [43] presented in section 3 demonstrated the presence of sub-gap current peaks for dc biased Josephson junction coupled to a single mode resonator, in good agreement with $P(E)$ theory.

Investigations on the emitted radiation, showing *"the bright side of dynamical Coulomb blockade"* was later addressed by Hofheinz *et al.* [41]. They measured both the Cooper pair current and the photon emission rate. They also extented the $P(E)$ theory to the photon emission.

In this last experiment, the sample consisted in a dc biased Josephson junction connected to a microwave resonator, with $\omega_0 / 2\pi = 6$ GHz resonant frequency.

The Cooper pair transfer rate was obtained from the average current measurement

$$\Gamma^{\mathrm{Cp}} = \frac{I}{2e}, \tag{50}$$

and the photon rate from the microwave power P, leaking from the sample around the resonance into the measurement chain

$$\Gamma^{\mathrm{ph}} = \frac{P}{\hbar\omega_0} \tag{51}$$

where $\hbar\omega_0$ is the energy of a photon at resonance. These two rates should be directly linked according to

$$\Gamma^{\mathrm{ph}} = k\,\Gamma^{\mathrm{Cp}} \tag{52}$$

where k is the number of photons emitted by each tunneling Cooper pair.

Both quantities were simultaneously measured while sweeping the dc bias voltage across the Josephson junction. The extracted rates Γ_{Cp} and Γ_{ph} are presented in Fig. 31. On the one photon peak, both rates are equal within the 5% measurement error bar.

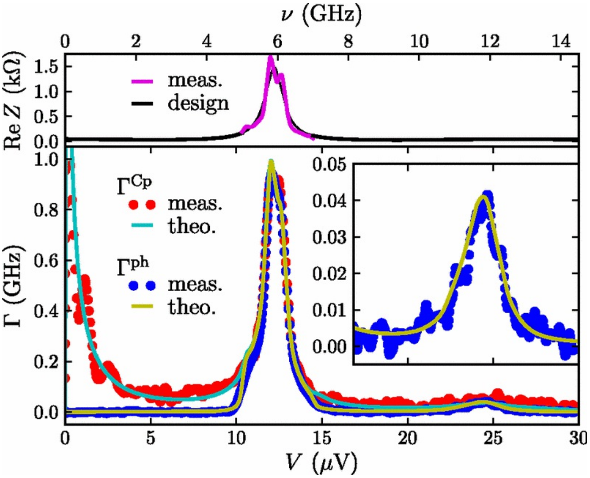

Figure 31. Photon and Cooper pair rates (taken from Hofheinz *et al.* [41]). Top : real part of the impedance seen by the junction, calculated from the resonator geometry (black line) and reconstructed (magenta) from a quasiparticle shot noise measurement.

Bottom : Measured Cooper pair Γ^{Cp}(red) and Photon Γ^{ph} (blue) rates extracted from current and microwave power measurements. The first resonance is hit when one CP emits one photon while tunneling : $V = \hbar\omega_0/2e \simeq 12\,\mu V$. The inset is a zoom on the photon rate at voltage 2eV = $2\hbar\omega_0$, corresponding to the two photon emission process. Solid lines are $P(E)$ theory fits.

In addition, all results of this work were in good agreement with the $P(E)$ theory and its extension. According to equations 46 and 50, the Cooper pair-rate is

$$\Gamma^{\mathrm{Cp}} = \frac{\pi}{2\hbar} E_J^2 P(2eV) \tag{53}$$

At, $T = 0$, one can compute $P(E)$ and obtains

$$\Gamma^{\mathrm{Cp}} \simeq \frac{E_J^*}{2\hbar^2}\left(\frac{r(\omega_J)}{\omega_J} + \int_0^{\omega_J} d\omega \frac{r(\omega)}{\omega}\frac{r(\omega-\omega_J)}{\omega-\omega_J}\right) \tag{54}$$

where $\omega_J = 2e\,V\,/\,\hbar$ is Josephson pulsation corresponding to a bias V, $r(\omega) = \pi \mathrm{Re}[Z_{\mathrm{env}}(\omega)]\,/\,R_Q$ is the coupling factor and E_J^* is the renormalized Josephson energy due to the environment phase fluctuations [36]

$$E_J^* = E_J\left(1 - \int_0^{\omega_J} d\omega \frac{r(\omega)}{\omega}\right). \tag{55}$$

The first term in the parenthesis of equation 54, represents the contribution of single photon processes, while the second term accounts for two photon processes, emitted at ω and $\omega_J - \omega$. In this experiment, the coupling was low ($r = 0.08$) and two-photon processes had much lower rates than the single photon processes as predicted by equation 47.

In conclusion, this experiment [41] validated the understanding of Dynamical Coulomb Blockade based on photon emission into the electromagnetic environment.

Other related works have confirmed this approach

- on a normal tunnel junction [2];
- in the case of two photon emission [65].

All these experiments have open the way to new schemes for the emerging field of quantum optics with microwave photons, dubbed quantum microwaves.

Some other groups have also focused on radiations emitted by a tunnel junction and used their properties to produce non-classical states of light [27][30].

5 Quantum circuit's dynamics

Although the extension of the $P(E)$ theory yields the spectral density of the emitted radiation, we present now two approaches [51][54] which allow us to go further and predict the full quantum properties of the emitted radiation.

5.1 Quantum description of the field

The microwave resonators used in this thesis consist of sections of TEM transmission lines. In order to get a full quantum description of the field in these resonators, we follow the approach of Yurke and Denker [75], who proposed a quantum description of the TEM modes of a one dimensional transmission line.

A transmission line is a conductor whose dimensions are not all negligible compared to the wavelength of the signals which are carried [67]. Its electrical variables are $Q(x,\, t)$, the total charge at the right from the point x at the time t and $I(x,t)$ the current [24]. They are defined for an infinite, lossless and unidimensionnal line by

$$Q(x,t)\,;I(x,t)=\frac{\partial Q(x,t)}{\partial t}\,;V(x,t)=-C_T\frac{\partial Q(x,t)}{\partial x} \tag{56}$$

where C_T is the linear capacitance of the transmission line and $V(x,t)$ the voltage.

The formalism of classical electromagnetism yields the Lagrangian [76]

$$\mathcal{L}=\frac{1}{2}\left[L_T\left(\frac{\partial Q}{\partial t}\right)^2-\frac{1}{C_T}\left(\frac{\partial Q}{\partial x}\right)^2\right]$$

The natural conjugate of the charge is then the flux

$$\Phi(x,t)=\frac{\partial\mathcal{L}}{\partial(\partial Q/\partial t)}=L_T\frac{\partial Q}{\partial t}=L_TI(x,t),$$

which simply corresponds to the magnetic flux per unit length threading the transmission line at t and x. In the case of a superconducting transmission line, the flux $\Phi(x,t)$ is related to the superconducting phase introduced in section 3.1:

$$\varphi(x,t)=\frac{\Phi(x,t)}{\varphi_0}.$$

The wave velocity is $v=(L_T C_T)^{-1/2}$.

According to the usual procedure of canonical quantization, $\hat{Q}$ and $\hat{\Phi}$ are operators and get

$$[\hat{Q}(x,t),\hat{Q}(x',t)]=[\hat{\Phi}(x,t),\hat{\Phi}(x',t)]=0$$

$$[\hat{Q}(x,t),\hat{\Phi}(x',t)]=i\hbar\delta(x-x')$$

We split the quantum fields in two counterpropagating waves

$$\hat{Q}(x,t)=\hat{Q}_{\leftarrow}(x+v\,t)+\hat{Q}_{\rightarrow}(x-v\,t).$$

One can then link these equations with quantum optics by describing charge dynamics in terms of creation/anihilation operators of free propagating waves [76].

$$\hat{Q}_{\leftarrow}(x+v\,t)=\sqrt{\frac{\hbar}{4\pi Z_C}}\int_0^{\infty}\frac{d\omega}{\sqrt{\omega}}(\hat{a}_{\leftarrow}(\omega)e^{-i\omega(t+{}^{x}\!/_{v})}+\hat{a}^{\dagger}_{\leftarrow}(\omega)e^{-i\omega(t+{}^{x}\!/_{v})})$$

$$\hat{Q}_{\rightarrow}(x-v\,t)=\sqrt{\frac{\hbar}{4\pi Z_C}}\int_0^{\infty}\frac{d\omega}{\sqrt{\omega}}(\hat{a}_{\rightarrow}(\omega)e^{-i\omega(t-{}^{x}\!/_{v})}+\hat{a}^{\dagger}_{\rightarrow}(\omega)e^{-i\omega(t-{}^{x}\!/_{v})})$$

where Z_C is the characteristic impedance of the line. The value $d\omega/\sqrt{\omega}$ is defined in agreeement with quantum optics concepts[75]. In fact, $\hbar/(4\pi Z_C)$ corresponds to the spectral power of charge fluctuations in the vacuum state $|0\rangle$ and the operator $a^{\dagger}_{\mu}(\omega)a_{\mu}(\omega)$ correponds to the flow of photons, having a pulsation ω and travelling in the direction μ.

These operators also obey the canonical commutation relations

$$[\hat{a}_\mu(\omega), \hat{a}_\nu(\omega')] = 0$$

$$[\hat{a}_\mu(\omega), \hat{a}^\dagger_\nu(\omega')] = \delta(\omega - \omega')\delta_{\mu\nu}$$

where μ and ν corresponds to travelling directions → or ←.

It is also possible to define the current and voltage operators $\hat{I}(x,\omega)$ and $\hat{V}(x,\omega)$. One can then link these quantities to the measured power at the output of the transmission line, considering $\Delta\omega$, the measurement bandwidth.

Finally, we can introduce the temporal equivalents of creation/anihilation operators

$$\hat{a}(t) = \int_{\Delta\omega} \frac{d\omega}{2\pi}\, \hat{a}(\omega) e^{-i\omega t} \quad ; \hat{a}^\dagger(t) = \int_{\Delta\omega} \frac{d\omega}{2\pi}\, \hat{a}^\dagger(\omega) e^{i\omega t},$$

which also obey the commutation relations

$$[\hat{a}(t), \hat{a}(t')] = 0$$

$$[\hat{a}(t), \hat{a}^\dagger(t')] = \delta(t - t').$$

The rate of photon detection in the measurement line is then obtained from $\langle \hat{a}^\dagger(t)\hat{a}(t) \rangle$. It also allows us to calculate field correlation functions using photon power measurements.

One thus sees that the concepts of Quantum Optics can be readily applied to microwave circuits and transmission lines with one important difference: the modes we have discussed here are surface plasmons associated to the TEM modes of our waveguides. As a consequence, they have only one polarization, so that iconic quantum information experiments as the one performed by Alain Aspect and co-workers to demonstrate the violation of Bell's inequality [5] cannot be envisionned in the systems we describe in this thesis.

We now give an input-output description of the environment and show why it is, in addition, a nice probe to observe the quantum properties of the field.

5.2 Input-output description of junction radiation

The decomposition of a transmission line modes into two counter-propagating fields allows to naturally introduce input-output theory formalism when we are interested in the boundary conditions of the line. Let's first consider a half-infinite transmission line, going from $x=0$ to $x=+\infty$ connected to a certain system at $x=0$ [75]. Fields propagating from the line to the system are described by the operators $a_{\text{in}}(\omega)$ and those going from the system to the transmission line are described by $a_{\text{out}}(\omega)$.

As the incident fields *in* are coming from the infinite, they are not affected by the presence or the absence of the system. They are just propagating modes of the line. However, fields outgoing of the system into the transmission line result from the interaction between the incident fields and the system, and impose boundary conditions to the line. By knowing this interaction mechanism, one can then link the state of the system to the outgoing modes which corresponds to measurement observables in an experiment.

Radiation of a Josephson junction coupled to an infinite transmission line

Juha Leppäkangas and Göran Johansson [55][53] have developed such a description in the case of a voltage biased Josephson junction connected to a semi-infinite transmission line. According to their description, the phase $\hat{\Phi}$ is defined as

$$\hat{\Phi}(x,t)= \sqrt{\frac{\hbar Z_0}{4\pi}}\int_0^{\infty}\frac{d\omega}{\sqrt{\omega}}\{\hat{a}_{\text{in}}(\omega)e^{-j(\omega t+x/v)}+\hat{a}_{\text{out}}(\omega)e^{-j(\omega t-x/v)}+h.c.\}\ .$$

This description of $\hat{\Phi}$ is true everywhere in the line, including in $x=0$, where it is related to the voltage across the junction through Josephson relations.

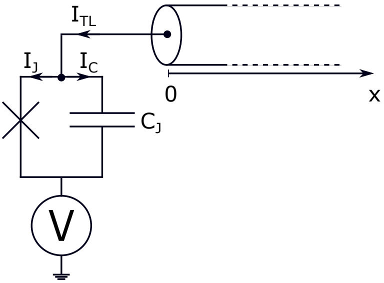

Figure 32. Model introduced in [75] to describe the radiation emitted by a Josephson junction into a semi infinite transmission line.

As shown in Fig. 32 and described in section 1, the junction is modeled as a pure tunnel element in parallel with a capacitance C_J.

The Josephson junction is biased with a perfect dc bias V at the input of the transmission line. The current in the transmission line is defined as

$$I_{\mathrm{TL}} = I_C + I_J$$

$$I_{\mathrm{TL}} = -\frac{1}{L_{\mathrm{TL}}}\frac{\partial\hat{\Phi}}{\partial x}(0,t)$$

$$I_C = \frac{\partial\hat{Q}}{\partial t}(0,t) = C_J\frac{\partial^2\hat{\Phi}}{\partial t^2}(0,t)$$

$$I_J = I_0\sin\varphi_J = I_0\sin\left(\frac{2e}{\hbar}(\hat{\Phi}(0,t) - Vt)\right)$$

where I_{TL}, I_J and I_C are the current of the transmission line, of the tunnel element and geometric capacitance of the junction, respectively.The boundary condition for the transmission line is then

$$C_J\frac{\partial^2\hat{\Phi}}{\partial t^2}(0,t) + \frac{1}{L_{\mathrm{TL}}}\frac{\partial\,\hat{\Phi}}{\partial\,x}(0,t) = -I_0\sin\left(\frac{2e}{\hbar}(\hat{\Phi}(0,t) - Vt)\right)$$

There is no general solution to this equation. However, in the so called "charge regime" where zero point charge fluctuations are small (which is the case for strong coupling constant), one can look for a perturbative solution in I_0 and decompose the outgoing mode of the transmission line as

$$\hat{a}_{\text{out}}(\omega) = \sum_{n=0}^{\infty} \xi^n \hat{a}_n(\omega).$$

where ξ is the perturbation of I_0. The zero order term, which corresponds to the case of pure capacitor without tunneling element is then

$$\hat{a}_0(\omega) = \frac{1 - j\, Z_0\, C_J\, \omega}{1 + j\, Z_0 C_J\, \omega}\, \hat{a}_{\text{in}}(\omega)$$

which corresponds indeed to the reflexion coefficient of an incident wave from a transmission line with the impedance Z_0 on a pure capacitance C_J. The following term contains the dynamical Coulomb blockade term due to phase fluctuations

$$\hat{a}_1(\omega) = -\frac{j\, I_0}{1 + j\, Z_0\, C_J\, \omega} \sqrt{\frac{Z_0}{\hbar \omega \pi}} \int_{-\infty}^{\infty} \mathrm{dt}\, e^{j\omega t} \sin\!\left(\frac{2e}{\hbar} \big(\hat{\Phi}_0(t) - \mathrm{Vt} \big) \right)$$

where $\hat{\Phi}_0(t)$ is the expansion at the first order in I_0 of $\hat{\Phi}(0, t)$, which corresponds to vacuum phase fluctuations at the level of the junction. This development can be extended to higher order to compute $\hat{a}_{\text{out}}(\omega)$ to any precision. All the information about the junctions radiations can then be extracted by calculation. Its spectral density $f(\omega)$ is given by

$$f(\omega) = \int_0^{\infty} \frac{d\omega'}{2\pi} \langle \hat{a}_{\text{out}}^{\dagger}(\omega) \hat{a}_{\text{out}}(\omega') \rangle.$$

Here, the $\hat{a}_{\text{out}}(\omega)$ are no longer field modes, and thus $f(\omega)$ calculations show other frequencies contributions. This expansion pushed to the second order in I_0 shows a contribution of thermal photons $f_{\text{th}}(\omega)$,

$$f_{\text{th}}(\omega) = \frac{1}{2\pi} \frac{1}{e^{\beta \hbar \omega} - 1}$$

which is negligible as soon as $k_B T \ll \hbar \omega$.

Radiation of a Josephson junction coupled to a resonator

We now treat the case of a Josephson junction coupled to a single mode resonator, leaking in the measurement line. We model the resonator as a section of transmission line with finite length, inserted between the junction and a semi-infinite line with a different characteristic impedance.

The position-dependent magnetic-flux is now defined for each section according to Fig. 33

- in the resonator $0 < x < d$

$$\hat{\Phi}(x,t) = \sqrt{\frac{\hbar Z_r}{4\pi}} \int_0^\infty \frac{d\omega}{\sqrt{\omega}} \{\hat{a}^r_{\text{in}}(\omega) e^{-j(\omega t + x/v_r)} + \hat{a}^r_{\text{out}}(\omega) e^{-j(\omega t - x/v_r)} + h.c.\}$$

- in the measurement line $x > d$

$$\hat{\Phi}(x,t) = \sqrt{\frac{\hbar Z_m}{4\pi}} \int_0^\infty \frac{d\omega}{\sqrt{\omega}} \{\hat{a}^m_{\text{in}}(\omega) e^{-j(\omega t + x/v_m)} + \hat{a}^m_{\text{out}}(\omega) e^{-j(\omega t - x/v_m)} + h.c.\}$$

where r, m refer to the resonator and measurement transmission line. In our experiment, we measure the outgoing field $\hat{a}^m_{\text{out}}(\omega)$.

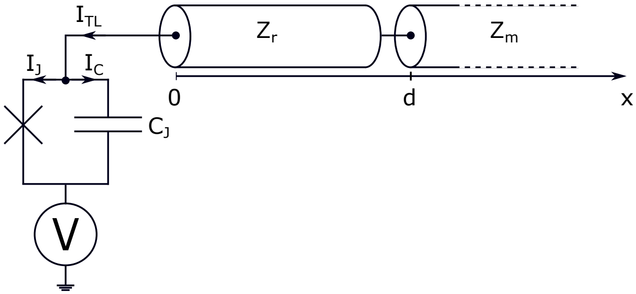

Figure 33. Model introduced in [53] to describe the radiation leaking from a single mode resonator coupled to a Josephson junction.

The authors of [53] calculate correlation functions of the outgoing field. They find for the photon flux leaking in the measurement chain

$$\langle \hat{a}^{m\dagger}_{\text{out}}(\omega)\hat{a}^{m}_{\text{out}}(\omega)\rangle = 2\pi\, f(\omega)$$

where $f(\omega)$ is identified as the photon flux.

Radiation due to inelastic Cooper-pair tunneling is, at the leading order in I_C

$$f(\omega) = \frac{E_J^2}{\varphi_0^2}\frac{\text{Re}(Z_{\text{env}}(\omega))}{2\omega}(P'(2eV - \hbar\omega) + P'(-2eV - \hbar\omega)).$$

This result relates the outgoing photon flux to the Cooper pair transfer rate across the Josephson junction, according to the $P(E)$ theory (equation 46.

The input-output theory developped in [53] shows how one can directly access the properties of a quantum conductor, here a Josephson junction, by measuring the power spectral density of the emitted radiation.

5.3 Photon statistics

We now give an introduction to the tools we use to characterize the emitted radiation and the statistics of the emitted photons.

In a two terminal conductor, in the low transparency limit where all conducting channel have a transmission $T_n \ll 1$, the Shot Noise spectral density was first described by Schottky [70] as

$$S_P = \frac{e^3|V|}{\pi\hbar}\sum_n T_n = 2e\langle I\rangle. \tag{57}$$

Stochastic (incoherent) processes are defined by their Poisson distribution [11] and this value is often reffered to as the Poisson Value of Shot Noise.

However, non-stochastic processes can follow different statistics and either be

- bunched : in that case, the statistics is super-Poissonian, meaning that the events have the tendency to occur simultaneously. This bosonic behavior is observed at the output of a photon beam splitter.

- anti-bunched : anti-correlated events corresponding to a sub-Poissonian statistics. For example, photons produced by relaxation of a single atom are emitted sequentially.

In mesoscopic physics, the Fano factor, introduced below, is commonly used to characterize this behavior [33][68], especially in the case of partitionning noise in QPC.

Fano Factor

In the classical case, Shot Noise spectral density, resulting from the tunneling of independent particles obey equation 57. Deviations from this value are the signature of electronic interactions, which can be quantified by the so-called Fano factor $\mathcal{F}$

$$S_{II}^{\text{Class}}(V) = 2e\mathcal{F}I.$$

In fact, $\mathcal{F}$ corresponds to the deviation from classical Poisson statistics

- $=1$ Poissonian noise
- >1 super Poissonian : bunching
- <1 sub Poissonian : anti-bunching
- $=0$ noiseless current perfectly correlated electrons

In quantum optics, one characterize the statistics of the emitted radiation using correlation functions [56][7][45].

First order correlator : $g^{(1)}$

Considering photon creation/anihilation operators $\hat{a}^\dagger/\hat{a}$, one defines the first order correlation function [56]

$$g_{\text{aa}}^{(1)}(\tau) = \frac{\langle \hat{a}^\dagger(t)\,\hat{a}(t+\tau)\rangle}{\langle \hat{a}^\dagger \hat{a}\rangle} \tag{58}$$

This quantity is directly proportionnal to the output intensity of a Mach-Zender interferometer with delay τ . This function $g^{(1)}$ describes correlations in terms of complex field amplitude, meaning it is sensitive to the phase coherence of the field.

Integrated over the frequency domain, this first order correlator becomes [53][56]

$$g^{(1)}(\tau)=\frac{\int_0^{+\infty}d\omega\,\omega\,\langle\hat{a}^\dagger(\omega)\,\hat{a}(\omega)\rangle e^{-j\omega\tau}}{\int_0^{+\infty}d\omega\,\omega f(\omega)},$$

where $f(\omega)$ the photon flux density [53] is

$$\langle\hat{a}^\dagger(\omega)\hat{a}(\omega')\rangle=f(\omega)\delta(\omega-\omega').$$

Second order correlator : $g^{(2)}$

This intensity-intensity correlator was created in the context of radioastronomy by Hanbury-Brown and Twiss who showed that it provides a much more precise measurement of star diameters [39]. Radioastronomy essentially focuses on thermal radiation sources, but in quantum optics, where a much wider range of sources are characterized, intensity-intensity correlation is a tool that can probe the non-classical nature of light. In fact, an important quantity describing photon emission is the relation between the first and second order moments. This intensity-intensity correlator $g^{(2)}$ is defined as

$$g^{(2)}(\tau)=\frac{<\hat{a}^\dagger(t)\hat{a}^\dagger(t+\tau)\hat{a}(t+\tau)\hat{a}(t)>}{<\hat{a}^\dagger\hat{a}>^2} \tag{59}$$

and quantifies correlations between a photon emission at a time t and the emission of a second one a a time $t+\tau$. As the system is experiencing a constant voltage bias, $g^{(2)}$ does not depends on t. This correlator $g^{(2)}$ can be measured using a single beam splitter and two power detectors [65], as we will decribe it in detail in chapter 6.

In the regime when each tunneling Cooper pair emits a single photon, the second order correlator of the emitted radiation is related to the current correlator

$$g^{(2)}(\tau)=\frac{\langle\hat{I}(t)\,\hat{I}(t+\tau)\rangle}{\langle\hat{I}(t)\rangle^2}.$$

At $\tau = 0$, $g^{(2)}(0)$, which measures the probability to emit two photons simultaneously, characterizes the type of radiation statistics :

- if $g^{(2)}(0) < 1$, the field is anti-bunched
- if $g^{(2)}(0) > 1$, the field is bunched
- for a Poissonian process $g^{(2)}(0) = 1$
- for thermal radiations $g^{(2)}(0) = 2$

Although arbitrarily large bunching is allowed for classical fields, anti-bunching is a direct proof of nonclassicality [73]. A perfect single photon source is characterized by its vanishing $g^{(2)}(0)$.

The link between the Fano factor and the second order correlator is given by the Mandel formula [57][60]

$$\mathcal{F} = 1 + \Gamma \int_0^{\infty} d\tau (g^{(2)}(\tau) - 1) \tag{60}$$

where Γ is the photon emission rate.

This equation illustrates the difference between these two values. In fact, $\mathcal{F}$ compares long time scale correlations and will always reach one for extremely low rates, whereas $g^{(2)}(\tau)$ characterises correlations at all times.

Classical fields

According to the proposal by Glauber [34], any classical field can be decomposed in a statistical mixture of coherent fields $|\alpha\rangle$ with the probability $P(\alpha)$. Its density matrix writes

$$\rho = \int d\alpha P(\alpha) |\alpha\rangle \langle \alpha|,$$

which yields the following result for the second order correlator

$$g^{(2)}(\tau) = \frac{\int d\alpha P(\alpha) |\alpha|^4}{(\int d\alpha P(\alpha) |\alpha|^2)^2} \geqslant 1.$$

In addition, in a field resulting from random processes, $a(t)$ and $a(t+\tau)$ are not correlated, yielding

$$\langle\hat{I}(t)\rangle^2 = \langle\hat{I}(t)\,\hat{I}(t+\tau)\rangle \to g^{(2)}(\tau) = 1$$

Furthermore, as correlations have finite time scales, this limit is reached at long time τ for both quantum and classical fields.

Beyond $P(E)$ theory

Photons in the cavity have a life time τ_{res} inversely proportionnal to the bandwidth of the resonator. The main assumption of $P(E)$ theory is that the environment goes back to equilibrium before each tunneling event. This assumption is valid as long as the life time of a photon in the resonator τ_{res} , is much shorter than the mean time between two subsequent tunneling events, Γ^{-1}, i.e. $\Gamma\tau_{\mathrm{res}} \ll 1$. In this fast relaxation regime, the electromagnetic field produced by an event cannot affect the subsequent one.

For high rates or strong couplings, the environment has not enough time to relax and influences subsequent processes, giving rise to non-classical radiation.

By tuning the Josephson energy, we can vary the emission rate $\Gamma(E_J)$ and thus, the average number of photons in the resonator $\langle n\rangle$.

As one aim of this thesis is to produce anti-bunched photons, we now present two theoritical proposals to reach this regime [54][37][51].

5.4 Anti-bunched photons using an additionnal resistor

In 2015 Leppakangas *et al.* [54] demonstrated that one could produce anti-bunched photons by voltage biasing a Josephson junction through a resistive environment, as shown in Fig. 34.

They show that the low frequency dynamics of the junction, characterized by a finite charging time RC, prevents simultaneous tunneling events to occur yielding to anti-bunching. This phenomenon is reminiscent from the proposal of Likharev and coworkers [6] to obtain anti-bunched electron sources.

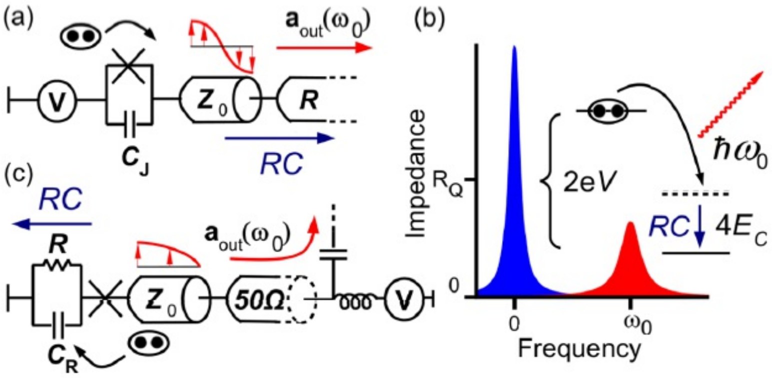

Figure 34. The single-photon source proposed by Leppäkangas *et al.* (figure reproduced from ref. [54]).

(a) a Josephson junction (JJ) with capacitance C_J is connected in series with a semi-infinite transmission line (TL) with an impedance step, $Z_0 <$ R, and voltage biased. The TL section provides a $\lambda/2$-resonator between the impedance step and the junction. The total effective impedance is described in (b)–(c).

(b) The impedance as seen by the JJ, presents a peak at zero frequency described by a zero frequency resistance $R > R_Q$ and a capacitance C defining its bandwidth, as well as a peak at finite frequency ω_0 opening a window for photon emission. When $2\text{eV} = \hbar\omega_0 + (2e)^2/2C$, a photon at ω_0 can be emitted by Cooper-pair (CP) tunneling together with many other ones in the low frequency environment. Further CP tunneling events are momentarily blocked. After a time RC the capacitor discharges and the next photon-assisted CP tunneling can occur.

(c) An experimentally feasible realization allowing for large zero-frequency impedance $R \gg R_Q$, while maintaining compatiblity with standard 50 Ω TLs.

A semiclassical picture indeed yields for the voltage across the junction after a tunnel event

$$v(t) = V - \left(\frac{2e}{C}\right) e^{-t/\mathrm{RC}}.$$

The system takes a recharging time RC to recover after the voltage drop $2e/C$ that occurs at a tunnel event. The associated correlation function is

$$g^{(2)}(\tau)=\frac{\int_{\mathrm{BW}}\mathrm{Re}[Z_{\mathrm{env}}(\omega)]P(2e\,v(\tau)-\hbar\omega)d\omega}{\int_{\mathrm{BW}}\mathrm{Re}[Z_{\mathrm{env}}(\omega)]P(2e\,V-\hbar\omega)d\omega} \tag{61}$$

where BW is the measurement bandwidth centered around the LC resonant frequency (see dashed lines in Fig. 35).

The computed $P(E)$ has a peak for $E=4E_C$, corresponding to the charging energy of the junction's capacitance, but it also show a second peak for $E=(2e)^2/2C+\hbar\omega_0$, corresponding to an additionnal excitation of the cavity mode according to Fig. 34. This last condition corresponds to a bias voltage $2e\,V=(2e)^2/2C+\hbar\omega_0$.

For charging times of the junction above the time resolution of the measurement chain, they calculated temperature effects on $g^{(2)}(\tau)$. They find that the resistor brings in thermal fluctuations that limit anti-bunching effects as shown by their more complete theory based on a fourth order expansion in E_J (see full lines in Fig. 35).

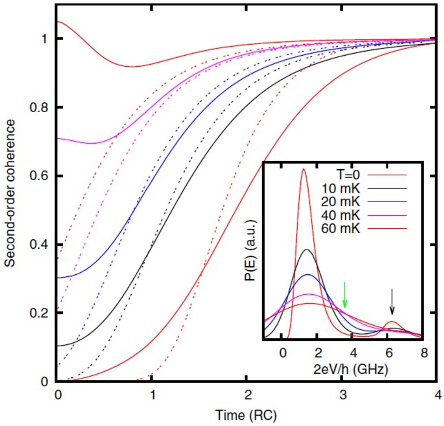

Figure 35. Second order coherence function $g^{(2)}(\tau)$ calculated by Leppäkangas *et al.* (figure reproduced from ref. [54]). Second-order coherence function based on semianalytical approximation Eq. 61 (dashed lines) and on the full theory (solid lines), at different temperatures. When biased optimally (black arrow in the inset), the anti-bunching observed within the RC timescale is strongly reduced by temperature. The semi-analytical formula 61 well accounts for the long-time behavior.

An experimental set-up implementing this theoretical proposal is presently developped by Hofheinz and coworkers.

5.5 Anti-bunching with high impedance resonators

A second way to produce anti-bunched photons, based on enhanced coupling with the resonator, was proposed in parallel by Ankerhold and coworkers [37][51].

We have implemented this proposal in this thesis work. It consists in coupling a dc voltage biased Josephson junction to a high impedance single mode resonator. This theoretical proposal focuses on the regime where E_J is low enough so that Cooper pair tunneling occurs sequentially.

According to $P(E)$ theory [46], the probability of a tunnel event is directly proportionnal to the probability to emit a photon in the resonator

$$P_{N\to N+1} \propto \left| <N+1 \middle| e^{-2i\sqrt{r}(\hat{a}^\dagger+\hat{a})} \middle| N> \right|^2 \delta(2eV - h\,f_0) \tag{62}$$

where $|N\rangle$ and $|N+1\rangle$, correspond to the number of photons in the resonator before and after tunneling, and f_0 is the mode frequency.

At low temperatures $h\,f_0 \ll k_B T$, the resonator is empty at thermal equilibrium. For low tunneling rates and when the junction is biased so that $2eV = h\,f_0$, where each tunneling Cooper pair emits one photon, one can consider, as a first approximation, only transitions from $|0\rangle$ to $|1\rangle$ and from $|1\rangle$ to $|2\rangle$. A calculation of the matrix elements in Eq. 62 yields

$$P_{0\to 1} \propto r^2\, e^{-r}$$

$$P_{1\to 2} \propto \frac{1}{4} r^2\, e^{-r} (2-r)^2$$

In the strong coupling regime, $P_{0\to 1}$ has a finite value but $P_{1\to 2}$ is strongly reduced and vanishes at $r = 2$, the case described by fig. 36.

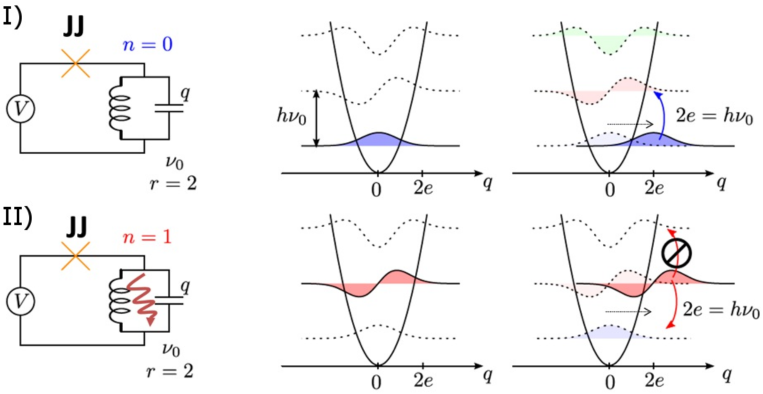

Figure 36. Anti-bunched photon source proposed by Gramich *et al.* [37]. Figure reproduced from ref. [65].

I: assuming the resonator is initally empty, the first tunneling Cooper pair emits one photon and the resonator goes from $|0\rangle$ to $|1\rangle$. The probability of this event is directly related to the overlap between the shifted $|0\rangle$ state wave function and the $|1\rangle$ state wavefunction.

II: The probability for a second Cooper pair to tunnel is then related to the overlap between the shifted by $2e$ $|1\rangle$ state wave function and the $|2\rangle$ state wavefunction. For $r = 2$, this overlap $|\langle 1|e^{-2i\varphi}|2\rangle| = 0$. As a consequence, when a Cooper pair tunnels and emits one photon in the resonator, it prevents further photon emission until the first one leaks into the measurement chain. This mechanism generates anti-bunched photons.

As a result, the emission of a first photon in the resonator blocks the tunneling of a second Cooper pair that would imply the emission of a second photon. Due to the finite lifetime in the resonator, the second tunneling event is blocked until the first photon escapes the resonator and leaks in the measurement chain. This ideal case corresponds to perfect anti-bunching/ single photon source.

For slightly lower coupling constant r, the transition $P_{1\rightarrow 2}$ is not forbidden but has a small probability, causing anti-bunching. To estimate the "effectiveness" of this blocking effect, Gramich *et al.* [37] calculate analytically the second order correlator $g^{(2)}(0)$ at zero time delay, see Fig. 37.

For low photon occupancy of the resonator it is simply given by

$$g^{(2)}(0) = (1 - {}^{r}\!/_{2})^2 \tag{63}$$

with $r = \pi Z_C / R_Q$ the superconducting coupling constant.

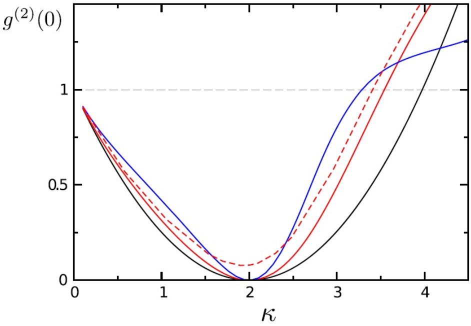

Figure 37. Second order correlation function $g^{(2)}(0)$ as a function of the coupling κ (which corresponds to r in this manuscript) and for different average population of the resonator $\langle n \rangle_0$ ($\propto$ photon emission rate): DCB-result for $\langle n \rangle_0 = 0.01$ (black) ; numerical data (RWA) for $\langle n \rangle_0 = 0.05$ (red), $\langle n \rangle_0 = 2$(blue) ; full data (non-RWA) including also the impact of 2-photon processes for $\langle n \rangle_0 = 0.5$, Q = 10 (red-dashed). Figure taken from ref. [51].

As expected and shown in fig.37, for a coupling constant $\kappa = r = 2$, photons are perfectly anti-bunched. However, even for lower coupling constants, significantly anti-bunched photons are emitted.

Effect of the photon emission rate on $g^{(2)}$

The average population of the resonator is directly related to the driving strength

$$\langle n \rangle_0 \propto \left(\frac{E_J^*}{\gamma} \right)^2$$

where $\langle n \rangle_0$ is the average population of the resonator, E_J^* is the normalized Josephson energy and γ is the damping rate of the cavity defined as

$$\gamma = \frac{\omega_0}{Q}.$$

As expected, anti-bunching is enhanced for low occupation number of the resonator where it is correct to consider only transitions from $|0\rangle$ to $|1\rangle$ and from $|1\rangle$ to $|2\rangle$. For higher occupation numbers, i.e. higher emission/tunneling rates, the resonator is in a statistical mixture of states. Transitions from $|2\rangle$ to $|3\rangle$ and to higher photon number states that are not blocked identically, must be considered. This explains why $g^{(2)}(0)$ approaches 1 when $\langle n\rangle_0$ increases.

On the other hand, for very low population of the resonator, the photon has time to escape in the measurement line long before the next tunneling event, destroying any correlation between subsequent tunnelings. Furthermore, the out of resonance simultaneous emission of two photons by a single tunneling Cooper pairs, provides a second source of coherence. For low Q resonators, this process induces a rise of $g^{(2)}(0)$, as shown in Fig. 38 and in agreeement with Olivier Palavecchio's results [65].

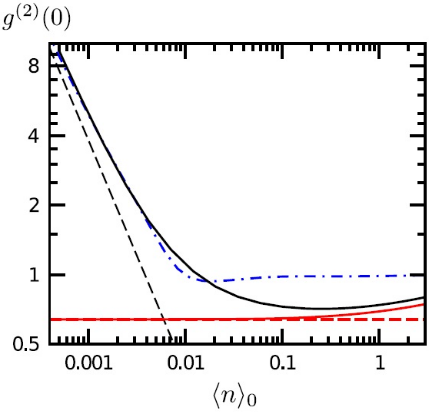

Figure 38. Photon correlation function $g^{(2)}(0)$ at the one-photon resonance versus the Josephson coupling as a function of $\langle n\rangle_0$: the one-photon contribution together with the result at the two-photon resonance for $r = 0.4$ (blue, dashed–dotted) ; the one-photon contribution (red, solid) reduces to the CB-result (red, dashed) for low driving ; the full g(2) (0) (non-RWA) at the single-photon resonance $\omega_0 = \omega_J$ (black, solid for Q = 5) diverges for weak driving due to the dominating impact of off-resonant two-photon processes in accordance with perturbative results (black dashed). Figure taken from ref. [51].

Dynamics of correlations : time resolved $g^{(2)}$

As previously described, Cooper pair tunneling is blocked as long as the first emitted photon stays in the resonator. As a consequence, considering the resonant case, we expect that $g^{(2)}(\tau) \to 1$ with a characteristic timescale given by the lifetime of photons in the cavity as descibed in [20]:

$$g^{(2)}(\tau) = \left(1 - \frac{r^2}{2} e^{-\gamma\tau/2}\right)^2 \tag{64}$$

with r the coupling constant and $\gamma = 2\pi\,\mathrm{FWHM}$ the photon leakage of the resonator.

This is shown to be true for the rather modest coupling strength achieved in our set-up. For higer coupling strength $r \sim 3$, the coherent evolution of the field in the cavity furthermore induces a suppression of $g^{(2)}(\tau \neq 0)$ as described in [20] and illustrated inf Fig. 39.

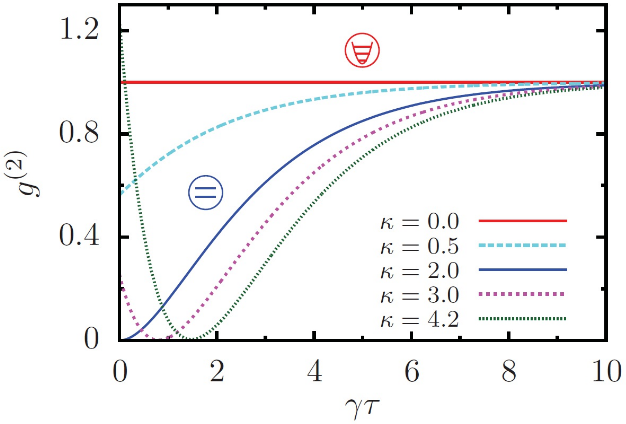

Figure 39. The second-order correlation function $g^{(2)}(\tau)$ in the number few-photon limit $\langle n\rangle_0 = (\sqrt{\kappa} E_J^* / \hbar\gamma)^2 \to 0$, for various values of the coupling constant κ (which corresponds to r in this manuscript). $\kappa = 0$ corresponds to the uncoupled harmonic oscillator and $\kappa = 2$ to a two-level system whith perfect anti-bunching. The nonlinearity for finite κ becomes apparent in suppressed (enhanced) transitions to the second-excited state. Figure taken from ref. [20].

The main goal of this thesis is to use this mechanism of cavity back-action to produce non-classical light. We have built high impedance resonators to imprint the anti-bunched behavior of Cooper pairs on emitted photons.

3 Designing the electromagnetic environment

In order to validate theoretical predictions from the group of J. Ankerhold [51], as described in 5.3, we want to apply a dc bias to a Josephson junction coupled to a high impedance single mode resonator and collect radiations leaking from the resonator.

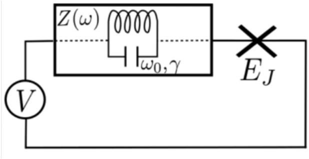

Figure 40. Theoretical circuit scheme. Picture extracted from ref. [37]

In an experimental point of view, this can be implemented by the following circuit:

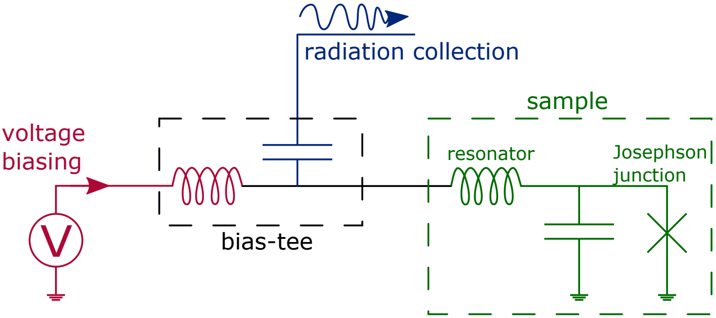

Figure 41. Measurement scheme. The bias-tee splits the applied dc voltage from the microwave signal.

The high impedance microwave mode we will use is represented by the green box in Fig. 41. Its resonant pulsation ω_0 and characteristic impedance Z_C are given by [67]

$$Z_C = \sqrt{\frac{L}{C}} \quad ; \quad \omega_0 = \frac{1}{\sqrt{\mathrm{LC}}}.$$

Aiming at acoupling strength $r \simeq 1$ at a frequency around 5 GHz, one gets, $Z_C \sim 2k\Omega$, $L \sim 60\,\mathrm{nH}$ and $C \sim 15\,\mathrm{fF}$, which corresponds to a very low capacitance.

In order to reduce the capacitance we decided to have the resonator on the same chip than the junction and to use quartz wafers, which have a small effective permittivity $\varepsilon_r = 4.2$ (in comparison with 11.8 for silicon).

To measure the radiation emitted by the junction, we will connect it to a dissipation-less resonator on a $3 \times 10\mathrm{mm}^2$ quartz chip, as shown in Fig. 57. This device is then bonded to a printed circuit board (PCB) with a single input/output port. The PCB will be placed in a metallic box and cooled down to 15 mK in a dilution refrigerator. Using an additional microwave component, called bias-tee we can apply a dc bias to the sample while collecting the emitted radiations in a 50Ω detection line.

Huge technical progress in the microwave technologies over the last twenty years provide us performing measurement apparatuses for frequencies around 5 GHz. We have first performed electromagnetic simulations to design a circuit presenting a single resonance between 4 and 8 GHz associated with a large impedance as seen from the junction and thus, optimize the coupling to the Josephson junction as described in section 1.

There are two different ways to build electromagnetic resonators : distributed circuits for which capacitance and inductance are distributed along a transmission coplanar waveguide (CPW), or lumped element circuits where discrete elements are drawn on the chip.

On a typical substrate, our target frequency range corresponds to wavelength of the order of $\lambda \sim 1\mathrm{cm}$. Having lines of the same length-scale, one can then use phase rotation along these lines in addition with their inductance and capacitance to the ground plane to build distributed element resonators.

However, the capacitance of a CPW line is already of the order of 100pF/m and a length of 150µm is too short to reach our targeted inductance. As a consequence, our resonator has to be based on lumped element geometries.

Using abacus, one can precisely estimate the length and shape required to obtain discrete element based inductances [67]. As the resulting line is longer than λ/10, phase rotation along the line will also influence the resonator behavior, forcing us to perform detailed electromagnetic simulations. In order to reduce its capacitance to ground, this line can be packed as a meander or wounded as a coil, which will be quantitatively compared in section 1.3.

Finally, a third parameter of the resonator that must be tuned is its quality factor Q. We consider a simple parallel LC oscillator with

$$Q = \frac{f_0}{\Delta f} = \frac{Z_C}{Z_S},$$

where Z_S is the impedance of the source as seen from the resonator and Δf the resonance bandwidth at -3dB. To tune Q, we can insert an impedance transformer between the 50Ω measurement line and the resonator and thus increase the effective input impedance.

1 Electromagnetic simulations

1.1 Sonnet simulations

In order to simulate our resonators, we use a high frequency electromagnetic software tool for planar circuits analysis : Sonnet. The system simulated by this software consists in several metallic layers separated by dielectrics as shown in Fig. 42.

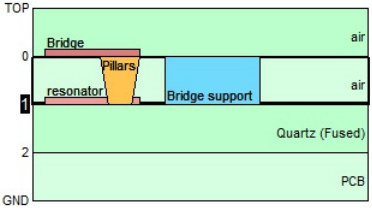

Figure 42. Sonnet schematic of the dielectric stack.

Each metallic sheet layer contains a metallic pattern for the circuit, with strip-lines or resonators and can be connected to the other layers through vias. Dielectric layers properties and thickness can also be chosen.

This stack is enclosed in a box with perfect metallic walls. The simulated device sees the outer world through ports that sit at the surface of the box, or are added inside the box, as probes shown in Fig. 43. Sonnet also provides additional tools making possible to insert lumped electric component in the circuit, between two points of the pattern.

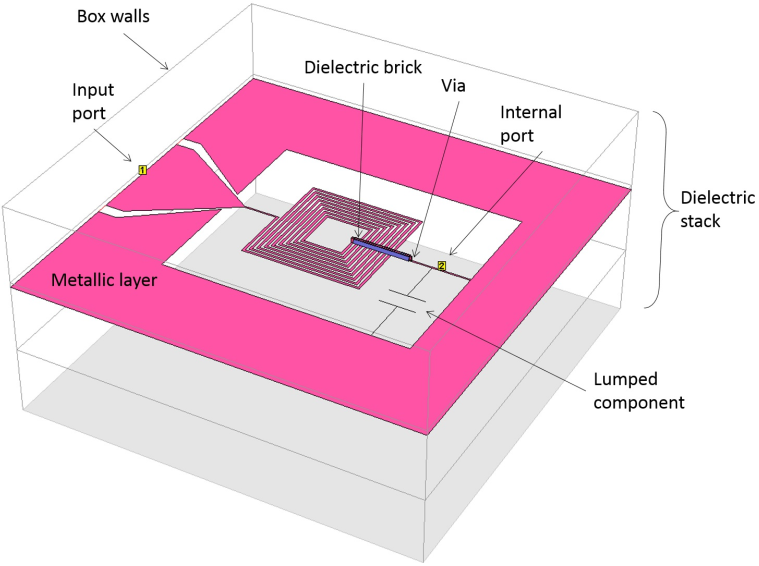

Figure 43. Sonnet simulated elements.

Using finite element based method, this software calculates scattering and impedance matrices at each port over a specified frequency band. It can also compute current/charge densities as well as far fields and build a π-model file of the circuit. It is also possible to build a network of previously simulated blocks and compile the overall system.

Port impedance definition

Ports are defined as presented below :

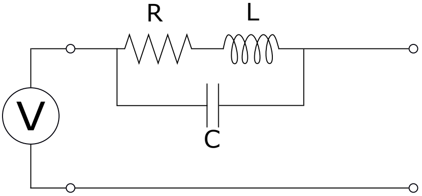

Figure 44. : Sonnet port configuration. They correspond to the parameters of the input line and can be tuned after the simulation.

When a port is used as an intput, a voltage source is connected to it and excite the system. Most of common apparatus as well as microwave devices have 50 Ohm output impedances, so we will assume in the following that input ports are defined with $R = 50\Omega$ and $C = L = 0$, unless it is precised.

As we are interested in the behavior of the environment seen by the junction, we will replace it by a port, which will act like a probe. As we will voltage bias the Josephson junction below the superconducting gap, there will be almost no current crossing the barrier ; we can thus model the junction as an open port. Furthermore, in order to take into account the junction's geometric capacitance, we add a discrete capacitor in parallel to ground as presented in Fig. 44.

1.2 Extraction of the characteristics of the resonator

In general, microwave systems are described by their scattering S-matrices, which gives access to the amplitude of in/outgoing electromagnetic waves. Impedance Z-parameters can also be used to describe a linear electromagnetic device and are more relevant in our case, as we will focus on the impedance seen by the Josephson junction. The *em* simulator Sonnet calculates S, Z and $Y = Z^{-1}$ matrices defined as :

$$S = \left\{ S_{i,j} = \frac{V_i^-}{V_j^+} \right\}_{V_{i \neq j}^+ = 0},$$

with V_i^+ and V_i^- amplitudes of incident and reflected voltage waves on port i, and

$$Z = \left\{ Z_{i,j} = \frac{V_j}{I_i} \right\}_{I_{k \neq i} = 0},$$

where the voltage V is the sum, while I is the difference of ingoing and outgoing waves. This matrix is calculated with “open ports”,i.e. with no current flowing through the other ports.

Using simulation results, we predict the resonant frequency f_0, the impedance seen by the junction Z_{out2}, the quality factor Q and the environment characteristic impedance Z_C. In order to mimic the actual set-up, our circuit is defined as

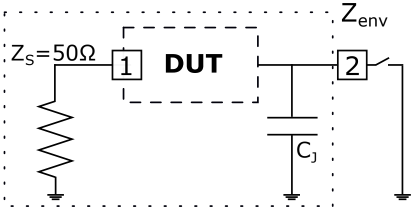

,

Figure 45. Schematic of our simulation block.

where the box represent the device under test (DUT), Z_S is the 50Ω input impedance of port “1”, C_J is the geometric capacitance of the junction and Z_{env}, the impedance seen by the junction.

Resonant frequency f_0

The resonant frequency, in the case of a lossless system, is usually found on S-parameters, by the point where the phase has turned by −180°. It also corresponds to the point where $\text{Im}[Y(\omega_0)] = 0$, meaning that the impedance Z reaches a maximum.

Impedance seen by the junction

As previously mentioned, the Z-matrix is calculated with all ports open. We will consider a resonant circuit connected to a 50Ω measurement line, according to Fig. 45, and we are thus interested in the impedance seen on port 2 when the port 1 is connected to 50Ω. This impedance Z_{env} can be extracted from the impedance matrix by

$$Z_{\text{env}}(\omega) = Z_{22} - \frac{Z_{12}\,Z_{21}}{Z_{11} + Z_S}$$

where $Z_S = 50\,\Omega$ is the impedance of the measurement line.

As discussed in section 1, we want to measure the power emitted by the junction, which is proportional to the real part of Z_{env}. For this reason, our simulations will mainly focus on the shape of $\text{Re}[Z_{\text{env}}(\omega)]$.

Quality factor

The width of the resonance gives access to the quality factor of the resonator. On typical S-measurement, it corresponds to the spectral width around resonance over which the phase rotates from -45° to -135° or when the transmitted power is divided by 2. This value can also be extracted from $\mathrm{Re}(Z_{\mathrm{env}})$ and corresponds to the full wifth at half-maximum (FWHM) of the real part of the impedance.

Characteristic impedance

The characteristic impedance of a single LC resonator can be extracted using the derivative of the admittance Y-matrix according to

$$Z_C = \sqrt{\frac{L}{C}} = \frac{2}{\omega_0 \, \mathrm{Im}[Y_{\mathrm{env}}(\omega_0)']},$$

where ω_0 is the resonant pulsation.

According to formula 11 from chapter 1, the characteristic impedance of an LC resonator connected to a $50\,\Omega$ measurement line can also be extracted from

$$Z_C = \int d\omega \frac{\mathrm{Re}[Z_{\mathrm{env}}(\omega)]}{\omega}.$$

As a consequence, our simulations aim at maximizing the integral of $\mathrm{Re}[Z_{\mathrm{env}}(\omega)]$.

More simply, one can also estimate the characteristic impedance from $\mathrm{Re}[Z_{\mathrm{env}}(\omega)]$ with a good precision by making the following assumption :

$$Z_C \approx \frac{\mathrm{Re}[Z_{\mathrm{env}}(\omega_0)]}{Q}$$

1.3 Large inductance simulations

To built lumped planar inductances, different shapes can be used : coils [59][58] or meanders [29][67]. Here, we first compare the inductance of a meander and a coil with similar sizes as it would be seen by the junction (according to the circuit of Fig. 45) and extract the corresponding inductances using the formula :

$$L = \frac{Z_C}{\omega_0}$$

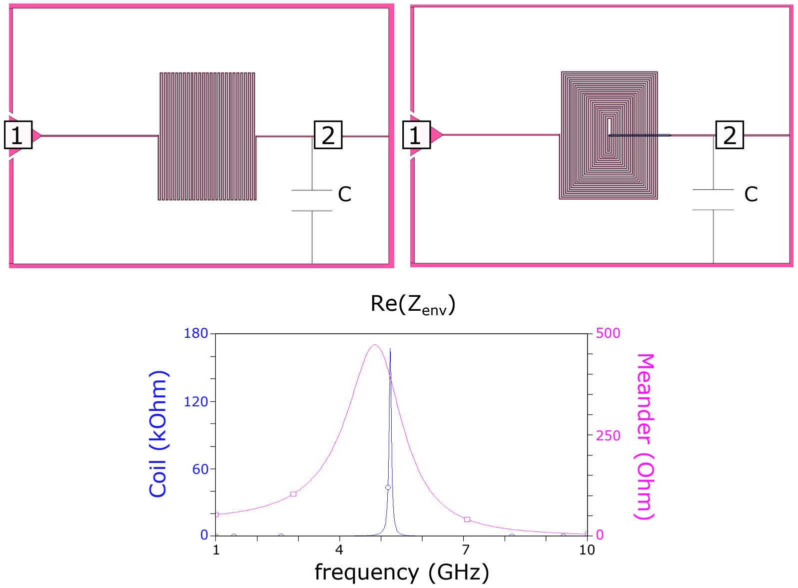

Figure 46. : a) & b) Sonnet drawings of the coil and meanderinductances forming a resonator with a lumped capacitor. Input port 1 is connected to a 50Ω load. c) Real part of the impedance $\mathrm{Re}[Z_{\mathrm{env}}(\omega)]$ as seen from internal port 2 (note the three orders of magnitude between left and rigth Y-scales for the two resonators).

The capacitance in parallel C_J, was tuned so that the resonant frequencies match the experimental frequency window in both cases and so that we can estimate whether a discrete capacitance must be added to the circuit. The resulting parameters and corresponding inductances are compared in the table below.

resonator	f_0(GHz)	Δf(MHz)	Q	$\boldsymbol{Z_C(\Omega)}$	L(nH))
Meander	4,85	1 720	2,8	**167**	5,4
Coil	5,22	65	80	**2k**	63,6

Table 1. Characteristics of the resonator extracted from simulations.

With no surprise, the inductance of the flat coil is more than ten times bigger than the inductance of the meander because of a mutual inductance generated by the turns. For the same resonant frequency, we can thus achieve ten time bigger characteristic impedances, making their utilization essential to our project.

In addition, these inductances already have a non negligible parasitic capacitance which cause the coil to get a self resonance (SRF), as already mentioned. We will use this parasitic capacitance, as well as the capacitance to the ground plane to build the resonator.

Planar coils have however one main disadvantage : their center has to be connected, using either bonding wires or bridges. We will first focus on the shape of the coil itself, and simulation results showing influence of the bridge will be presented in the following section 1.4.

Coil simulations

Coils can have different shapes as shown in Fig. 47. By using circular shapes, we avoid the charge accumulation in the corners and the associated parasitic capacitance. We are thus able to optimize the characteristic impedance as well as the quality factor.

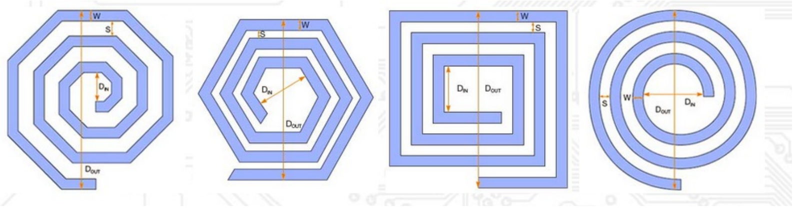

Figure 47. Common flat coil shapes.

As the size of a coil is of the order of hundreds μm in diameter and the line are of the order of a μm, it is not really compatible with electron beam lithography (EBL) which would be very long. Our design must then be compatible with optical lithography techniques, meaning at least 1μm wide lines.

By playing with the space between the lines, the number of turns, the inner diameter and the distance to the ground plane, we were able to tune the resonant frequency and the impedance of the mode.

1.4 Bridge

To connect the center of a coil, several options are possible. Some groups have chosen air bridges, some other place dielectric spacers below the bridge. It is also possible to connect the center of the inductance with a bonding wire (Christian Schönenberger, private communication).but it requires to have a big pad in the middle of the coil, at the cost of a higher parasitic capacitance.

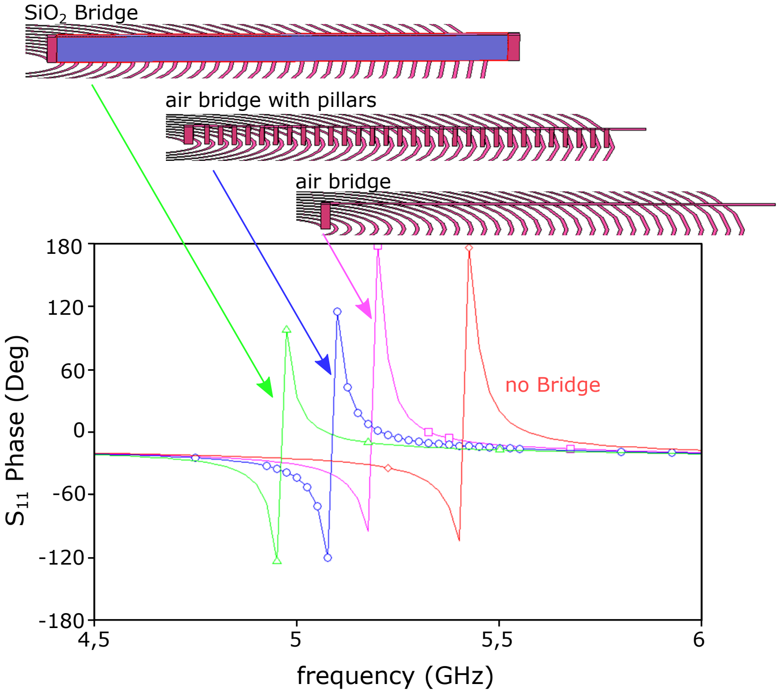

Figure 48. Reflected phase response of the resonator with different bridge configurations. The height of the bridge was 500 nm in all simulations (vertical scale was multiplied by 10 on drawings).

All these solutions have a non negligible influence on the resonance, as shown in Fig. 48 . In fact, the bridge forms a capacitor with every turn of the coil.

As the radius of the coil is of the order of $\sim 100 \mu m$, the solution of an air bridge is not compatible with fabrication constraints. One must either add pillars between the turns of the coil, or place a piece of dielectric on top of which sits the line. After several unsuccessful trial with air bridges, we have decided to use bisbenzocyclobutene (BCB) based bridges. Its description is given in table 2 and compared with other common insulators.

dielectric	PMMA	BCB	SiN$_X$
relative permittivity ε_r	2.8	2.65	3.9
losses factor (tanδ)	10^{-2}	8.10^{-4}	$1{,}510^{-2}$

Table 2. Properties of common dielectrics.

The BCB is a low loss dielectric which has been developed for such applications by the microwave industries which also has a relatively low permittivity. Using it, we were also able to increase the insulator thickness from 500nm to $>1 \mu m$ and reduce the capacitance to the coil.

1.5 Final design

After several simulations, we decided to use the following parameters :

Coil	nb of turns	line width	line space	bridge
	23.5	1 μm	2 μm	BCB / 1.2 μm
Results ($C_J = 2$fF)	f_0	Δf	Z_C	Re$(Z_{\text{env}})_{\text{MAX}}$
	5,1 GHz	60 MHz	2,05 kΩ	188 kΩ

Table 3. Geometric parameters of the resonator and associated characteristics.

The corresponding schematic and result of simulations are shown in Fig. 49. Now, the lumped capacitor C_J represents the capacitance of the Josephson junction alone, the rest of the capacitiance being implemented by the surrounding ground.

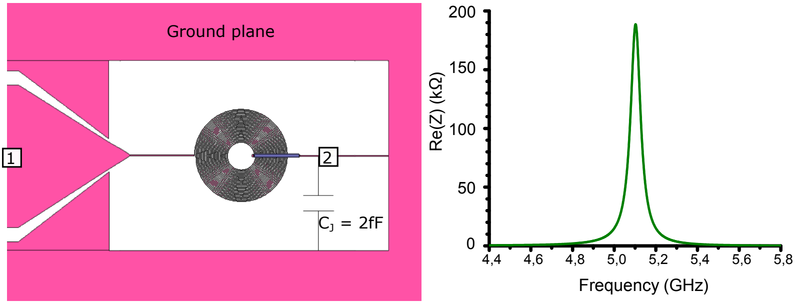

Figure 49. Final design drawing (left) and associated simulation result(right).

Computing current densities

In order to understand the full resonator behavior, we have simulated current and charge densities at resonance, as shown in Fig. 50.

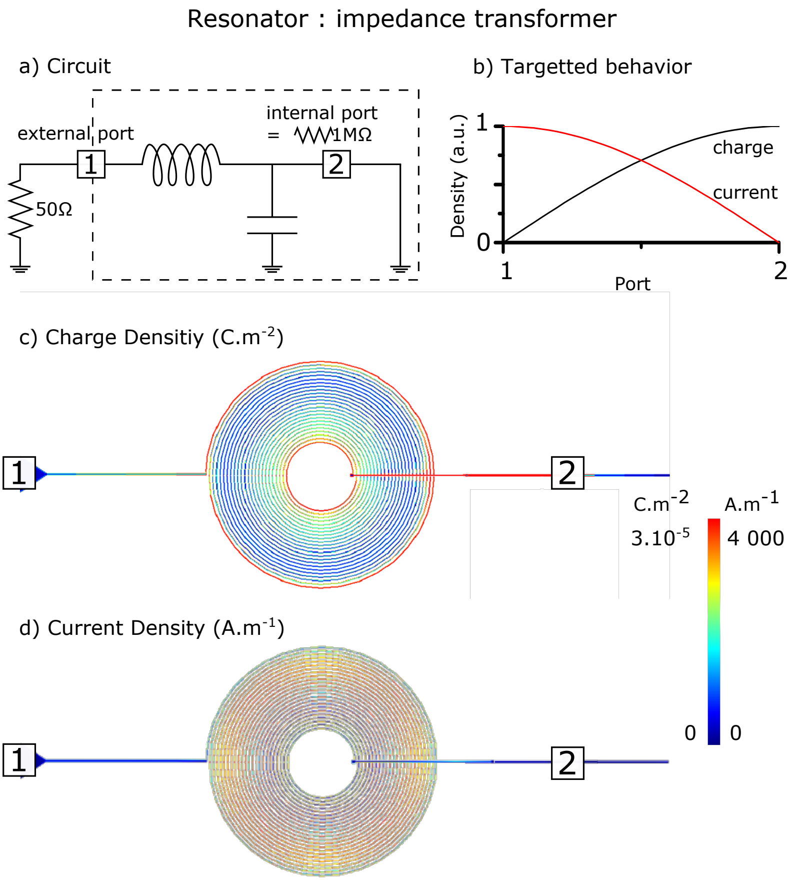

Figure 50. a) Our circuit has two ports. One external port "1" to be connected to the measurement chain can be modeled as a 50Ω load. The second port "2" is internal to the circuit and parametrized to mimic the Josephson junction open between the resonator and the ground plane probes the impedance seen by the future junction. These boundary conditions make us expect the resonator to behave like a $\lambda/4$ resonator.

b) In a typical $\lambda/4$, the low impedance port 1 corresponds to a node in charge and an anti-node in current, while on the "open" side port 2, there is an accumulation of charges and no current.

c) As expected, there is a charge accumulation on the high impedance side of the resonator. As the coil is used as an inductance but is also the capacitance of the circuit, there is an accumulation of charge at the periphery, i.e. in the first turn of the coil.

d) There is indeed no current flowing through the high impedance side and we see an increase toward the low impedance port.

in c) and d) the ground plane shown in fig. 49 is not represented here as it does not present peculiar current/charge density.

1.6 Junction's capacitance influence

The Josephson junction's geometric capacitance C_J is of the order of few fF ($70\,\mathrm{fF}.\mu m^{-2}$) [42] and is also part of the environment seen by the pure Josephson element according to

$$Z_{\mathrm{env}}(\omega) = \frac{Z_{\mathrm{circuit}}(\omega)}{1 + jC_J\omega Z_{\mathrm{circuit}}(\omega)},$$

where $Z_{\mathrm{circuit}}(\omega)$ is the impedance of the resonant circuit connected to the measurement line without junction.

By adding a discrete capacitor to ground $C = C_J$ (cf. fig. 45) at the junction's position in simulations and tuning its value, one can then observe in Fig. 51 that it is not negligible and must be taken into account.

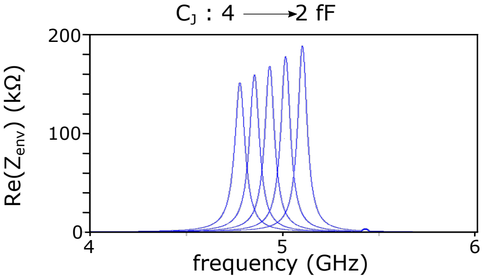

Figure 51. Real impedance seen by the junction $\mathrm{Re}[Z_{\mathrm{env}}(\omega)]$ for different junction capacitances

As we aim at building a resonator with a capacitance around 15 fF, C_J will account for 10 to 20% of the total capacitance of the circuit. As a consequence, both characteristic impedance and resonant frequency will be decreased by 5 to 10%.

1.7 Tuning the bandwidth using quarter wavelength

resonator

According to table 3 and Fig. 49, our resonator has a bandwidth of $\Delta f \sim 60\text{MHz}$. For experimental reasons which will be presented in the next chapter, it is useful to broaden this resonance while preserving the characteristic impedance and resonant frequency.

In fact, keeping the same resonator geometry, one can enlarge its bandwidth by inserting a second resonator between it and the source to play the role of an impedance transformer (quarter wavelength). Doing so, we can increase the input impedance seen by the coil and broaden the resonance as shown in Fig. 52.

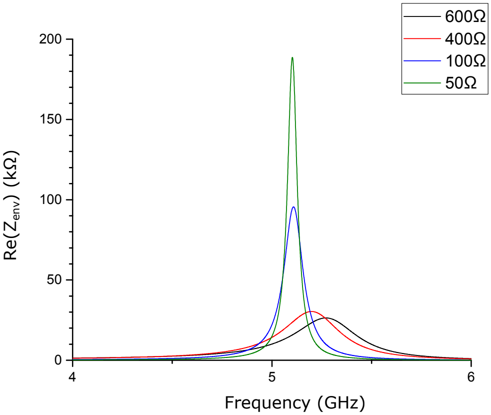

Figure 52. By increasing the input impedance of port 1, one observes a small increase of the resonant frequency and a broadening of Z_{env}, while the characteristic impedance is preserved.

We have built this second stage of impedance transformer “on chip” between the measurement line (modeled by Z_0) and the coil, using a lossless coplanar waveguide (CPW) of length $l = \lambda/4$ according to :

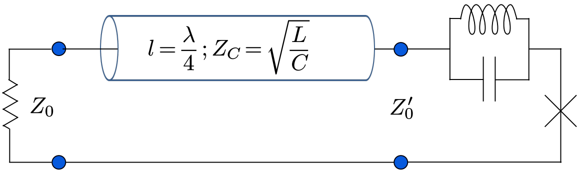

Figure 53. Circuit with an addinitionnal impedance transformer.

This transformer is characterized by

$$Z_0'=\frac{Z_C^2}{Z_0},$$

where Z_C is the characteristic impedance of the line, Z_0' the “new” load impedance of the resonator and Z_0 the 50Ω input impedance of the input line.

One can then choose the impedance seen by the coil (the impedance Z_0' of the transformer) by tuning the characteristic impedance Z_C. To do so, textbook calculations allow to choose the good ratio between the width of the central conductor and the distance to ground plane on a particular substrate [74]. The bandwidth of the resonator, corresponding to an input impedance of 50Ω, is 60MHz. By adding quarter wavelength transformers, we increase Δf as listed in table 4 :

Δf (MHz)	Z_0'	$Z_c, \lambda/4$	width(μm)	Gap (μm)
60	50	-	-	-
100	100	70	25	10
300	400	140	10	50
500	600	173	5	67

Table 4. Influence of an additionnal impedance transformer on the resonator bandwidth.

The length of the line must be tuned to a quarter of the resonant frequency wavelength, which on a quartz wafer, is around ∼1cm. In order to fit on the $3\times 10\text{mm}^2$ chip, this line will be packed as a meander, taking into account that the ground plane between two lines must be, at least five times larger than the gap. Sonnet simulations give the following results for the resonance of the different transformers :

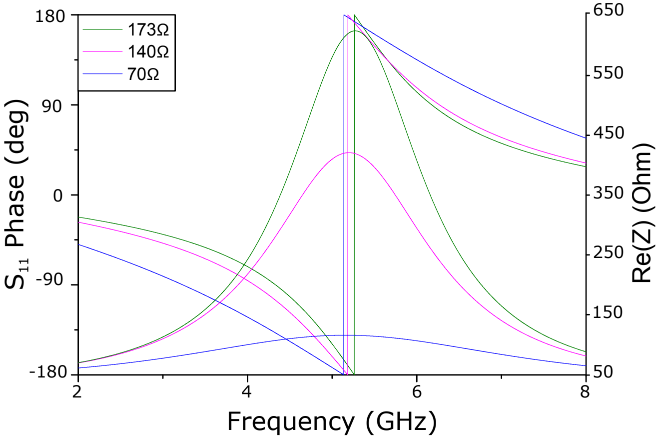

Figure 54. S_{11} phase and $\mathrm{Re}(Z_0')$ for $\lambda/4$ transformers of table 4

Using these simulations as a first block and the previous coil results as a second one, the full circuit was simulated, using the Sonnet “netlist” feature. Such a combination of previous simulations assumes no geometric “crosstalk” between the two resonators, which makes sense given that they are shielded from each other by ground planes. We obtained the results of Fig. 55.

1.8 Further improvement perspective : flat coil on SiO2 membranes

Simulation results above, exhibit characteristic impedances of 2.2 kΩ, leading to coupling factor $r \sim 1$ (see chapter 1). In order to increase further the coupling and reach the ideal value of $r = 2$, the resonator should have a characteristic impedance of ~4.1 kΩ.

One way to obtain such a value, would be to reduce further the capacitance of the resonator, by fabricating the inductance on silicon nitride

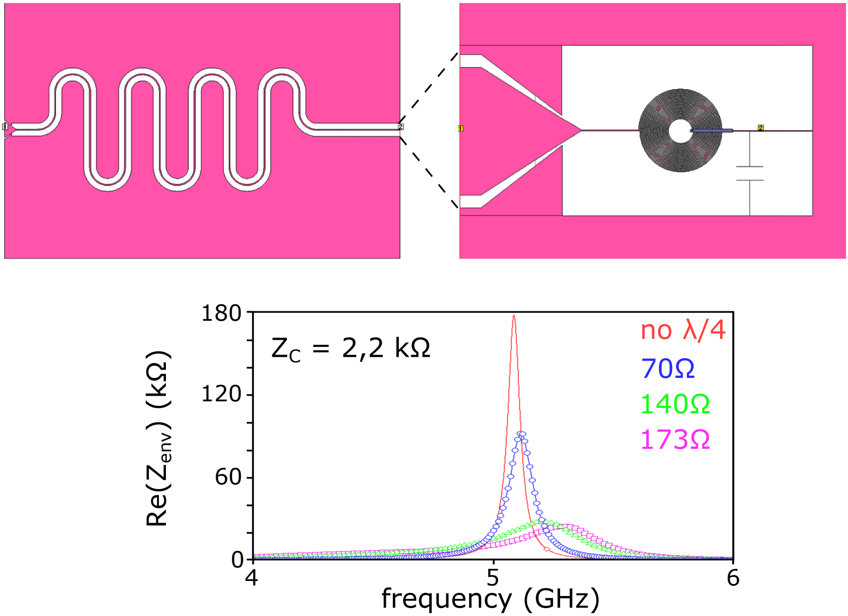

Figure 55. : initial simulation result and Netlist simulation results for the 3 $\lambda/4$ transformers of table 4

We were then able to check that the $\lambda/4$ resonator has no influence on the characteristic impedance by extracting it for each design. In order to have different bandwidth, these four configurations were fabricated.

membranes.

Running simulations with the previously designed 25 turns resonator, we were able to increase the characteristic impedances by 50%. As the resonant frequency increases as well, one could also increase the inductance by building larger coils. This design was not implemented however during my PhD.

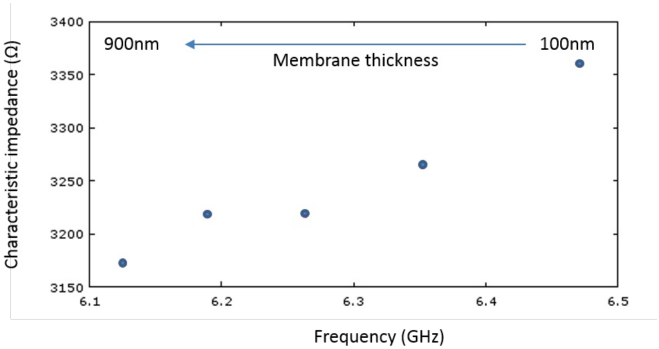

Figure 56. Influence of the membrane thickness on the characteristic impedance and resonant frequencies.

2 Fabrication

As mentioned in the previous section, we want to build the circuit of Fig. 57 on a $3 \times 10\text{mm}^2$ low permittivity quartz chip with a single input/output port adapted to a $50\,\Omega$ measurement line.

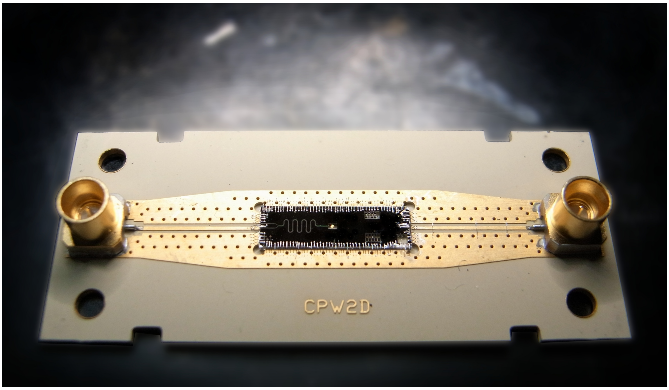

Figure 57. Picture of the chip.

Our fabrication process consists in 3 mains steps. First, we fabricate Niobium based coil and quarterwave impedance transfromers. Then, we connect the center of the coil to its periphery with a bridge and finally, as it is the most fragile element, we fabricate the Josephson junctions.

2.1 Resonator: coil and $\lambda/4$

In order to be able to test the samples at 4K, we chose to built niobium based resonator. As Niobium is of a much better quality when sputtered than evaporated, we used a top down approach for this step.

A 100 nm a layer of Niobium was first deposited on a $430\,\mu m$ thick Quartz wafer at 2 nm/s using a dc-magnetron sputtering machine and then patterned by optical lithography and reactive ion etching (RIE).

In order to pattern the resonators, we used an optical lithography process. The classical optical lithography process used a resist thick enough so that all the niobium between the lines can be removed before all the resist is etched: the S1813.

It was spinned according to the following recipe:

1. 110°C prebake of the substrate on hot plate
2. Resist spinning : S1813, 4000 rpm 45" / 8000 rpm 15"
3. 2 min rebake on hot plate

Using these parameters, and performing interferometric measurements, we measured a resist layer of 1450 nm. The sample was then exposed with a Karl-Süss MJB4 optical aligner, with a dose of 150 mJ/cm^{-2} (15 secs). Finally it was developed using microposit MF319 during 90 seconds and rinsed in deionized water for at least 1 min.

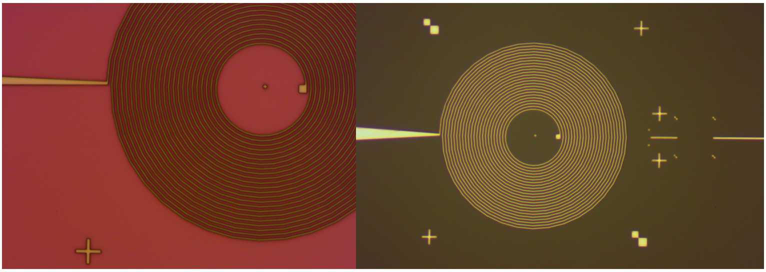

Figure 58. Fabrication of the coil. Left : optical image after optical lithography. Right : optical image after niobium etching.

The next step of the process is the reactive ion etching of the niobium film : we used a mixture of CF_4 and Ar (20/10 cc) at a pressure of 50 μbar (plasma off) and a power of 50 W (209V) for 4 minutes 45 seconds (150 nm). After this process, the sample was cleaned in 40°C acetone for 10 minutes to remove any resist residues and rinsed in IPA.

The quarter wave resonator was fabricated at the same time as the coil by Niobium etching.

Figure 59. 70 Ω quarter wavelength resonator and coil. The whole chip is $3 \times 10\text{mm}^2$.

2.2 Bridge

As we decided to use a dielectric spacer to support the bridge, we added two additional steps to the fabrication process. One for the dielectric spacer, the second one for the brdige itself. One of the main difficulties of these steps is that, as the pads to connect the bridge is small, they require very precise alignment.

Dielectric support

We chose to work with polymers derived from B-staged bisbenzocyclobutene, sold as Cyclotene 4000 by Dow Chemicals and choose the lower viscosity, in order to obtain a spacer between 0.8 and 1.8μm thick: XU35133. The process was performed according to the following recipe:

1. 2 minutes prebake at 110°C

2. Primer AP 3000 rpm 30 secs

3. BCB XU : 3000rpm, 45secs/ 8000 rpm 15 secs

4. 3 minutes rebake @80°C

Using this technique, we obtained 1650 nm thick layers. The sample was then exposed with the MJB4 optical aligner, with during 3 seconds. The development of this resist is quite difficult as it is not dissolved by acetone:

1. 30 secs on hot plate (70 °C) : to avoid that the bridge flows
2. DS 3000 rinsing for 1 minute
3. TS 1100 rinsing for 30 seconds
4. 1 min rinsing in deionized water
5. the sample was then dried while spinning

In order to obtain a flat surface and remove all resist residues, an RIE SF_6/O_2 etching was performed for 30 seconds (20/2 cc, 10 μbar, 50 W) as shown in Fig 60. Finally, the sample was rebaked during 30 minutes at 190°C to stabilize the resist.

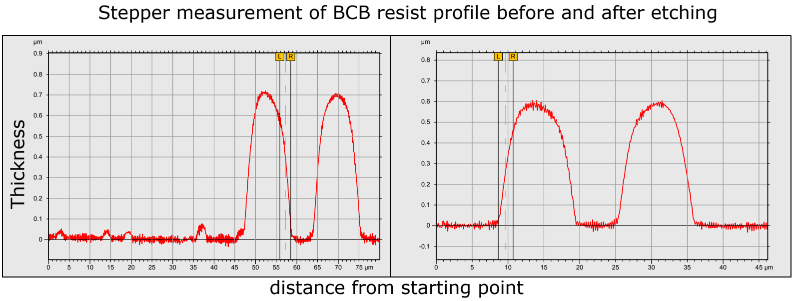

Figure 60. The flatness of the sample was measured with a stepper. After 30 seconds of SF_6/O_2 etching, resist residues have disappeared

Bridge's line

As the spacer is quite thick, this step requires a thicker resist. We used AZ5214 and obtained a 1.5μm layer of resist according to the recipe:

1. 72°C prebake on hot plate
2. microposit primer : 6000rpm for 30 seconds
3. AZ5214 : 4000 rpm during 60s, 8000rpm during 10s
4. 2min rebake at 100°C with a bescher on top of the sample

The sample was then aligned and exposed during 7s using the MJB4. As the AZ5214 is a negative resist which can be reversed, we rebaked the sample for 3min at 120°C and performed a flood exposure for 25 seconds. The development was then performed using diluted AZ 400K with deionized water (1:4) for 1 min. Finally, the BCB was covered with a 200 nm layer of aluminum after 12 seconds Argon etching to ensure good contacts with the coil.

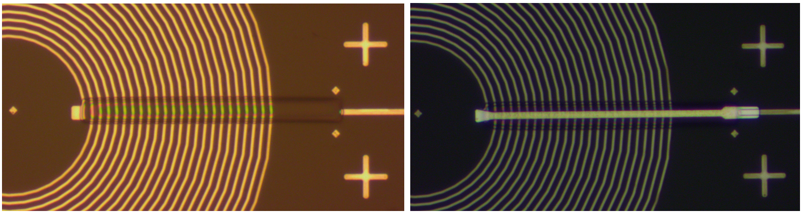

Figure 61. Left: in a first step, a BCB brick is deposited with optical lithography. Right: in a second step the core of the coil is connected with an aluminum bridge.

2.3 Josephson junction

As explained in chapter 2, for $r \simeq 1$, strong anti-bunching effects are expected when the resonator is, in average, almost empty. The maximum photon emission rate is given by

$$\dot{n} = \frac{\mathrm{Re}[Z(\omega_0)] I_0^2}{2\hbar\omega_0},$$

from which the mean occupation number n can be deduced by:

$$\dot{n} = \frac{n}{\Gamma},$$

with $\Gamma = 2\pi\,\mathrm{HMBW}$, the leaking rate of the resonator. In order to estimate the targeted resistance of the junction, one uses the Ambegaokar-Baratoff formula and Josephson relations (taking into account that DCB will renormalizes E_J by a factor of $\exp(-\pi Z_c / 2\, R_Q)$):

$$I_0 = \frac{\pi\Delta}{2\mathrm{eR}_N}, \qquad E_J = \frac{\varphi_0 I_C}{2\pi}.$$

In order to be able to tune E_J with a magnetic field, a SQUID geometry is used for the josephson junction: two junctions are placed in parallel to form a loop, which behaves as a single effective junction tunable with the external magnetic flux applied to the loop.

As a small capacitance is required for the resonator, junctions must be as small as possible, but big enough to be reproducible and lead to a good symmetry between the two branches of the SQUID. Assuming a symmetry of 90%, E_J can then be reduced by a factor of 10 tuning the flux with a little coil on top of the sample.

Assuming a bandwidth $\Delta\omega \sim 100$MHz, a characteristic impedance $Z_C \sim 2k\Omega$, a critical current I_0 of 1nA and a symmetry of 90%, one can estimate the minimal amount of photon in resonator :

$$n = 1/100.\frac{\dot{n}}{\Gamma} = \frac{Z_C I_0^2}{2h(\Delta\omega)^2.100} e^{-\pi Z_c / R_Q} \sim 0.5$$

with $\Delta\omega$ the half maximum bandwidth of the resonator (FWHM). These parameters require a normal state resistance for the SQUID of

$R_N \sim 300k\Omega$.

Fabrication principle

Samples are made of aluminum based tunnel junctions, fabricated by double angle evaporation through a suspended shadow mask, according to a technique developed 40 years ago [25]. By adjusting the angles of evaporation, two adjacent openings in the mask can be projected onto the same spot, creating an overlay of metallic films as shown in fig. 62. The first film is oxidized before the second evaporation to form the tunnel barrier.

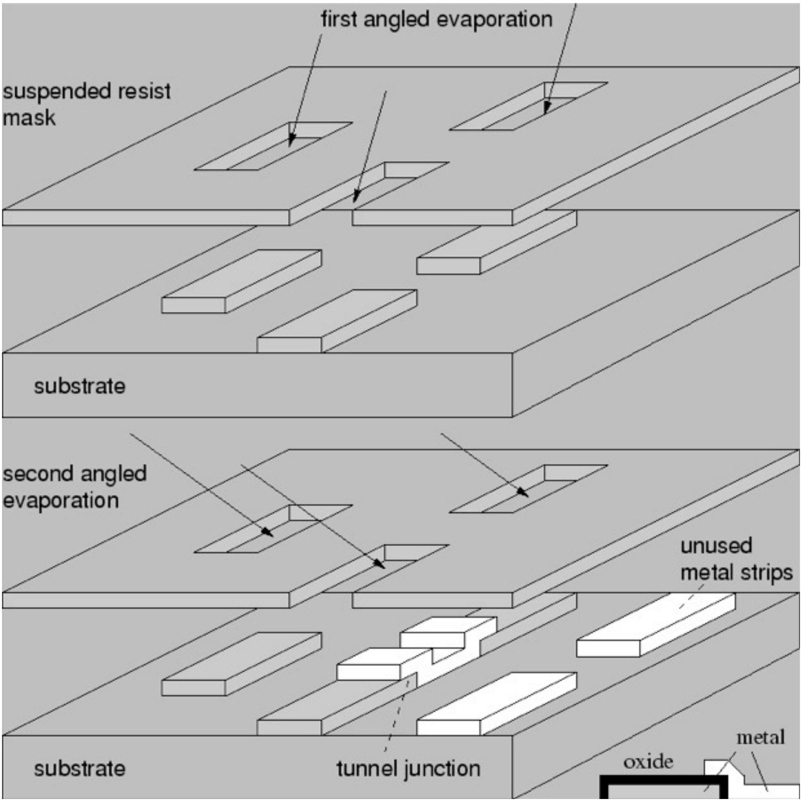

Figure 62. Double angle evaporation principle: two metallic layers are evaporated onto the same spot, creating an overlay of metallic films. As the first layer was oxydidized, the two electrodes are separated by an insulator and form a Josephson SIS junction.

In order to have reproducible as well as small junctions, we used a cross shape as shown in Fig. 63.

SQUID fabrication

PMMA/PMGI resist bilayer spining :

1. 2 min rebake at 110°C
2. Ti prime 6000 rpm 30 secs
3. PMGI SF8 : 3000rpm, 45secs/ 6000 rpm 15 secs ($\approx 613 \pm 15$nm)
4. 5min rebake @170°C with bescher
5. PMMA A6 : 6000rpm, 60secs ($\approx 253 \pm 21$nm)
6. 15 min rebake @ 170°C (with bescher)

As the quartz is very sensitive to charging effects, we placed an additional 7nm layer of aluminum of top of the resist to evacuate charges during EBL. The full wafer was then covered by a thick layer of UVIII resist which can be removed in IPA and sent to IEF for dicing. Actually, as the Quartz substate has an hexagonal symmetry, it cannot be cleaved.

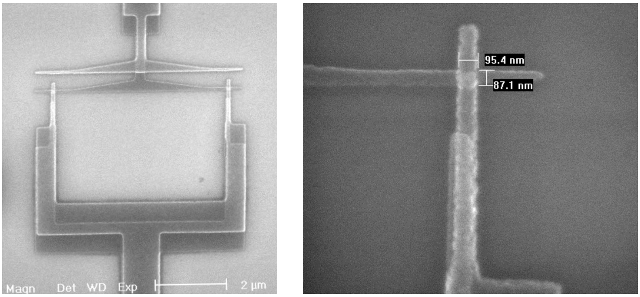

Figure 63. Left: SEM image of the SQUID. Right: zoom on one of the Josephson junction with size $95 \times 87\,\mathrm{nm}^2$

We then performed EBL on single chips using an FEI XL30 SEM with a dose of 300 μC.cm^{-2} at 30 kV. The focus was tuned a three point on the sample using 20 nm gold colloids.

The development process then consisted in :

1. 35 secs MIF 726, 15 secs ODI to remove the aluminum layer
2. 60 secs MIBK + IPA (1:3), 30 secs IPA, 15 secs ODI to open the Josephson junction patterns
3. 25 secs MIF 726, 1min ODI, 15 secs ethanol to have a nice undercut

Double oxidation junctions

Finally, we deposited and oxidized aluminum to form highly resistive Josephson junctions using double angle evaporation technique. In order to fabricate very resistive Josephson junctions, the group of J.P. Pekola [42] raised the idea of oxidizing not one layer of aluminum but to do it twice. By evaporating an additional subnanometer thick layer of Al immediately after oxidizing the first layer, and oxidizing this fresh very thin layer, one thus obtain thicker barriers.

The key parameter of this recipe is the thickness of the intermediate thin Al layer. As it will be completely oxidized we can achieve resistances up to $1M\Omega$ with 0,4nm. Using this process, the surfacic capacitance of the junction is estimated to 70 fF / μm^2 i.e. $\sim$2fF for the SQUID.

1. Argon ion milling 2x10 secs / 3 mA
2. -24° : 20 nm Al @ 1 nm.s-1
3. O2/Ar (15/85 %) oxidation 300 mbar during 20 min
4. 0.25 nm Al @ 0.1 nm.s-1
5. O2/Ar (15/85 %) oxidation 667 mbar during 10 min
6. 24° : 80 nm Al @ 1 nm.s-1

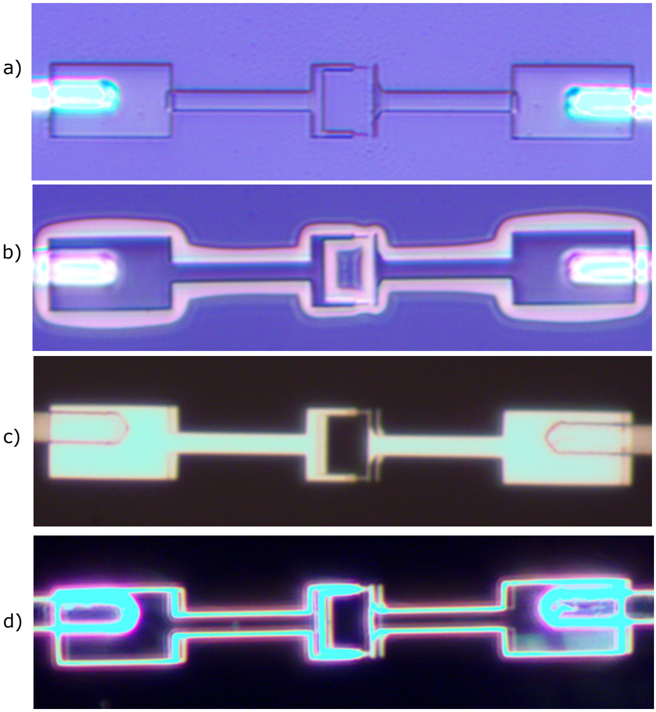

Figure 64. Josephson junction fabrication steps :

a) Josephson junction shape : PMMA development

b) Undercut : PMGI development

c) & d) optical microscope view of the junctions after lift-off

The lift-off of the resist was done by putting the sample in 60°C remover-PG during 40 minutes. In order to get uniform resistance values and limit Josephson junctions aging, they were rebaked on a hot plate at 110°C during one minute.

The chip was then stuck on the PCB with UVIII resist and bonded to the single input/ output port using aluminum wires as shown in Fig. 57.

The chip was then placed in a brass box, connected to the measurement chain and cooled down to 15mK.

4 Measurement techniques and set-up calibrations

As presented in details in chapter 1, we want to apply a dc voltage bias to a Josephson junction coupled to a high impedance microwave resonator and collect the emitted radiation leaking from the resonator into a 50Ω detection line. In chapter 3, we have presented simulations results of our microwave resonators with resonance frequency in the 4-5 GHz range, i.e. inside the 4-8 GHz detection bandwidth we are equipped for.

The first measurement step consists in characterizing the resonators (section 1); we then couple them to a Josephson junction nanofabricated on chip. The sample was then cooled at 15 mK and connected to a measurement set-up (Sec. 2), comprising a dc line (Sec. 2.1) and a microwave measurement line (Sec. 2.2).

1 4K characterization of the resonators

Our resonators are made of niobium whose critical temperature $Tc \sim 9K$, higher than liquid helium temperature. In order to first test the resonators and probe our designs, the junction is not made, thus leaving this side of the resonator open. We dip the chip in liquid Helium and perform reflection measurements with a vectorial network analyzer (VNA).

Reflection measurement set-up

Our sample has only one port, and can thus be characterized through reflection measurements only. In order to differentiate reflections from the sample from the parasitic reflection of the measurement line, we use an hybrid coupler and perform S_{21} measurements with a VNA as shown in Fig. 65. This is indeed equivalent to an S_{11} measurement.

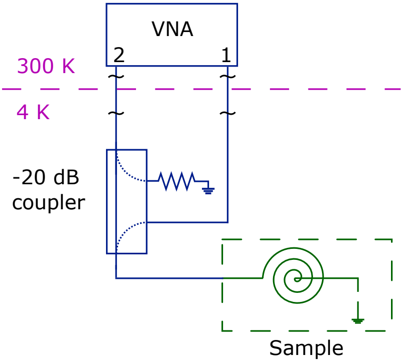

Figure 65. 4K S_{11} measurement set-up : the signal is sent to the sample from port 1 of the VNA and measured in port 2. In order to avoid parasitic reflections, both line are attenuated. The hybrid coupler provides an additional 20 dB attenuation of the input signal.

To perform this measurement, we place attenuators between cables to avoid standing waves. In addition, we use the internal attenuators of the VNA to reduce the power of the output signal. In fact above a certain input power, the sample turns normal and the resonance disappears.

We measure the S_{21} signal on the VNA which corresponds to the signal reflected by the sample. We performed magnitude and phase measurements. As we measure a dissipation-less resonator, the amplitude of S_{11} is always $\sim 0\,\mathrm{dB}$. After removing the slope in the phase due to the cable length, this measurement gives access to the resonant frequency and the quality factor Q from

$$\mathrm{Arg}(S_{11}) = -2\,\mathrm{Arctan}\left(2\,Q\,\frac{f-f_0}{f_0}\right). \tag{65}$$

Coil & bridge

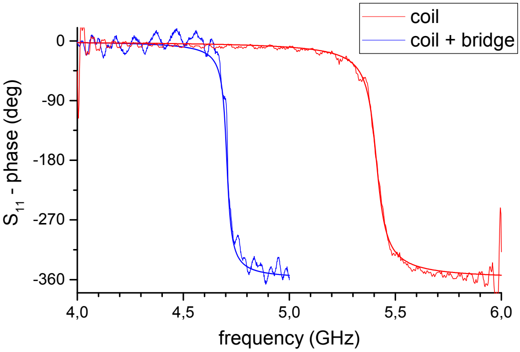

Figure 66. 4K reflection measurements of the resonator without (red) and with the BCB bridge (blue). The fits yield the resonator parameters given in table 5.

The results extracted from these measurements are given in table 5.

experiment (sonnet)	Coil	+ bridge		+ JJ
f_0 (GHz)	**5.41** (5.97)	**4.7** (5.19)		**4.47**(5.1)
Q	**80** (85)	**93** (104)		**65**(74)

Table 5. Resonator parameters extracted from measurements (bold) and simulations (in parentheses).

The third column corresponds to a different measurement of the resonator connected to the Josephson junction. Instead of performing reflection measurements, we have used the Josephson junction voltage biased above the gap as a white noise source and measure the emitted radiations to characterize the microwave environment. This last measurement was performed at 15mK.

The initial resonance frequency is lower than the simulation results (see chapter 3) by 10%, which is quite significant but still compatible with our measurement set-up (allowing detection in the 4-8 GHz frequency range). We have performed simulations to check whether this could be due to the width of the coil lines, to the height of the simulation box or to the wafer thickness. In the simulations, these parameters do not affect the resonance. We attribute this shift to an additional capacitance of unknown origin.

This is somewhat not surprising, as we observed that the resonant frequency depends of the precise way our sample box is closed. We thus attribute this discrepancy to a capacitive coupling of our resonator to the sample box not correctly taken into account in our simulations.

The bridge, in good agreement with simulations, decreases the resonant frequency by 15%. This is qualitatively easily understood as the bridge capacitively couples the high impedance end of our resonator to the low impedance input, so that one can think of the bridge as an additional capacitance.

Even though the full resonant circuit can be modeled as a parallel LC resonator, one sees in table 5 that the contribution of the bridge cannot be modeled as a simple capacitive contribution (which would lower the quality factor). In fact, the capacitance between the turns as well as the mutual inductance are affected in a non trivial way by the addition of any element. The bridge thus modifies the current distribution in the entire inductor, thus making electromagnetic simulations essential.

In our simulations, assuming a size of $2 \times 100 \times 100$ nm^2 for the junctions [42], we took a Josephson junction capacitance $C_J = 2$ fF. Our experimental results indicate that the capacitance added by this element is more important (around 5 fF). In fact, our estimate was not taking into account the capacitance related to the lines connecting the SQUID to rest of the circuit which might be responsible for a capacitance of 1.5 fF (assuming $C_L = 40$ pF.m^{-1}). In addition, the SQUID branches may also bring some parasitic capacitance and can further increase the shunting capacitance.

Both the bridge and the junction's capacitance lower the resonant frequency of our inductor but did not strongly affect the characteristic impedance. Our complete resonator is still compatible with our measurement chain, allowing us to access the strong coupling regime.

2 Voltage bias of a Josephson junction and collection of emitted photon

We then build an experiment analogous to the experiment of Hofheinz *et al.* [41], without current measurement in order to reduce the voltage noise on the dc line. The corresponding experimental set-up is presented in Fig. 67 : the capacitive port of the bias tee guides the photons emitted by the junction to a microwave amplifying chain, whereas its inductive port is connected to a low frequency circuit making possible to apply a dc voltage bias V to the junction.

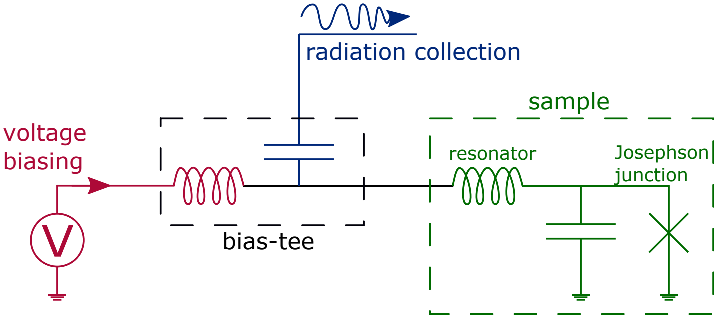

Figure 67. Measurement scheme. The bias-tee splits the applied dc voltage from the microwave signal.

One important feature of our measurement set-up is to apply dc bias voltage to the sample while measuring the emitted microwave radiations. In this aim, the resonator is galvanically coupled to the biasing line through a single port.

2.1 Low noise voltage biasing

As previously mentioned in section 3, in order to emit radiations into the environment, the sample must be biased according to

$$2e\,V = k\,h\,f_0,$$

where f_0 is the resonance frequency of the mode. This condition requires the voltage noise amplitude on the biasing line to be much smaller than the equivalent width of the resonator

$$\delta V \ll \frac{h\,\Delta f}{2e},$$

where $\Delta f = 130\,\text{MHz}$ is the full width at half maximum (FWHM). This is fairly difficult as it corresponds to a $\delta V = 300\,\text{nV}$.

Voltage divider

In order to reduce the noise shined on the sample from the room temperature DC bias source (Yokogawa), we voltage bias the sample through a huge voltage divider of $200\,\Omega$ / $6.5\,\text{M}\Omega$ according to Fig. 68.

Thanks to this divider, we can voltage bias the junction with a precision of a fraction of μV and thus neglect the noise coming from the voltage source as it will be divided by $R_1 / R_2 \sim 3.2\,10^4$.

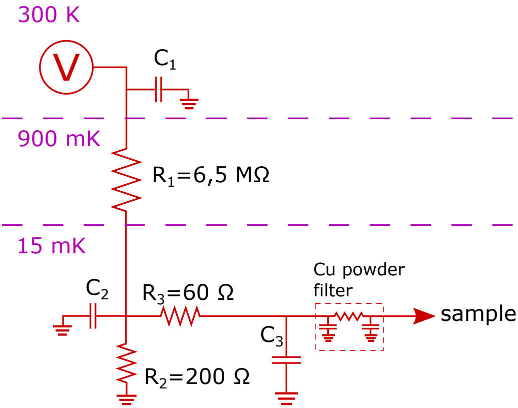

Figure 68. Bias line filtering scheme.

The first biasing resistor $R_1 = 6.5\,M\Omega$ is placed at 1K to reduce thermal fluctuations. The second resistor of the voltage divider is a distributed resistance $R_2 = 200\,\Omega$ associated with an important capacitance to ground $C_2 \sim 100\,\text{nF}$, thus providing a first RC filtering stage.

The sample is finally biased through a $60\,\Omega$ resistor (remain of the previous current measurement set-up) in parallel with a Presidio capacitor $C_3 = 100$ nF at room temperature, and supposed to increase at low temperature. This forms a second stage of RC filtering.

The Copper powder filter does not contribute to the low frequency filtering but protects the sample for very high frequency noise that may have been transmitted across the two first filters through parasitic capacitive couplings.

Thermal noise on the biasing line

Here, we estimate the total noise power that reaches the sample. In fact, each resistor of the line can be modeled as a pure resistance in parallel with a current noise source as shown in Fig. 69., which shines thermal fluctuations to the rest of the circuit.

As they are almost suppressed by the voltage division, we do not consider intrinsic voltage fluctuations of the source and 1K fluctuations of the resistor $R_1 = 6.5\,M\Omega$. In addition, we neglect the contribution of the Copper powder filter as its resistance is negligible ($0.3\,\Omega$).

As a consequence we consider here two stages of RC filtering : R_2C_2 and R_3C_3. The amplitude of the voltage noise of each RC circuit can be calculated independently according to

$$\delta V_{\mathrm{RMS}}^2 = 4\,k_B T_N\,R\,\Delta f$$

Where Δf is the bandwidth of the circuit, given by the considered RC filter cut-off frequency $1/2\pi R\,C$. The voltage noise then takes a very simple form

$$\delta V_{\mathrm{RMS}}^2 = \frac{1}{2\pi}\int_0^{+\infty} \frac{d\omega}{1 + R^2C^2\omega^2}\,4k_B T R = \frac{k_B T}{C}. \tag{66}$$

where T is the temperature of the resistance. As a first approximation, we can sum up the noise that is brought by the stages independently, which is not irrelevant if the cut-off frequencies of the second filtering stages does not filter most of the noise of the first stage.

In order to validate our filtering strategy and estimate the amplitude of voltage noise at the sample level, we perform lock-in power measurement to extract the cut-off frequency of the biasing line.

As described in Fig. 69, we first apply a constant bias V_0 to the sample, in order to hit the side of the single photon processes resonance. In this regime, we expect the emitted power to be proportional to the impedance of the resonator at the Josephson's frequency $2e\,V\,/\,h$. We then add a second contribution $V_{\mathrm{AC}}\cos(2\pi \mathrm{f} t)$ and chose $V_{\mathrm{AC}} = 4$ mV that corresponds to a bandwidth $V_{\mathrm{AC}}\,/\,(h\,/\,2e) = 58$ MHz over which we can consider that the impedance seen by the junction is a linear function of the Josephson frequency (black arrow).

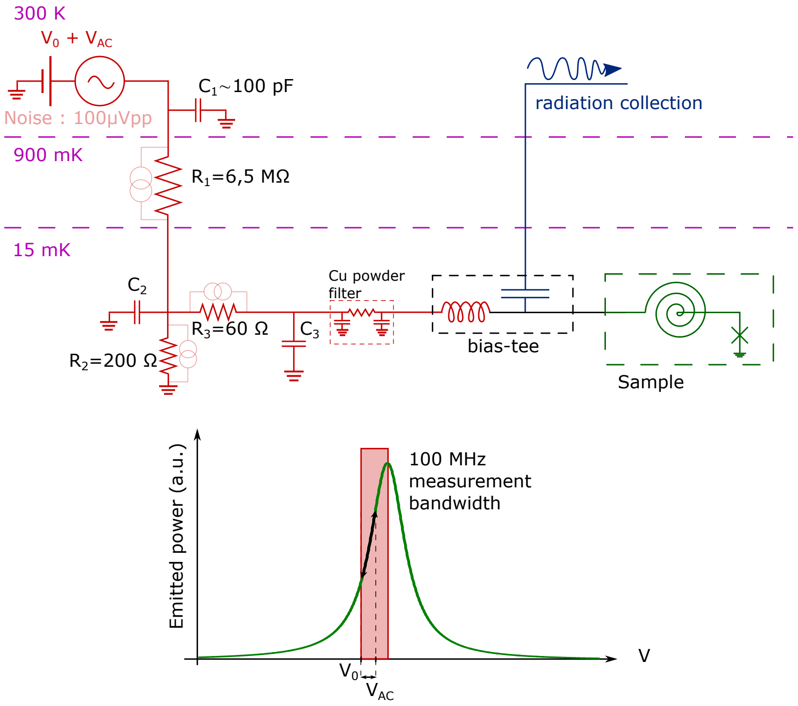

Figure 69. Measurement of the DC line frequency cut-off.

As shown in Fig. 70, we measure the excess power as a function of the modulation frequency. In this regime, the emitted power is proportional to the impedance of the environment $Z_{\mathrm{env}}(2e\,V\,/\,h)$ and thus increase linearly with the effective voltage applied to the sample.

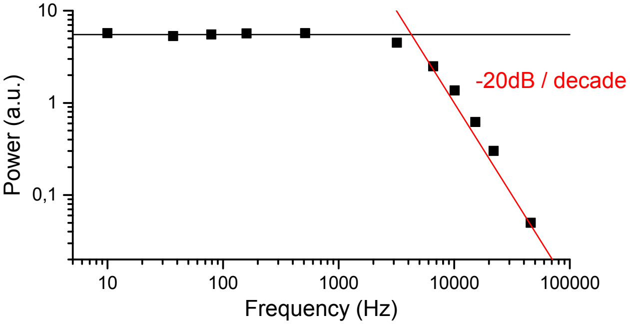

Figure 70. Excess power emitted by the sample as a function of the frequency modulation on the bias.

From this measurement, we extract the cut-off frequency $f_c \simeq 5$ KHz and the filtering slope. The slope of -20 dB/decade on the power measurement corresponds to a slope of -20 dB/decade on the amplitude of the applied voltage and thus to a second order filter. This means that both the second and third stages have a frequency cut-off around f_c.

We know that $C_3 = 100\,\mathrm{nF}$ at 300 K and increases as low temperatures up to $\sim 1\,\mu$F. Considering a 5 kHz cut-off frequency, we estimate $C_3 = 500\,\mathrm{nF}$ at 15 mK. From this measurement, we also deduce approximatively the value of C_2, as given in table 6.

Stage	R	C	frequency cut-off
2	$200\,\Omega$	$\sim$150 nF	5 kHz
3	$60\,\Omega$	$\sim$500 nF	5 kHz

Table 6.

A straightforward calculation of the noise contribution from this 2-stage filter gives

$$\delta V_{\mathrm{RMS}}^2 = \frac{2k_BT}{\pi}\int_0^{+\infty}\frac{R_2 + R_3\left(1 + R_2^2C_2^2\omega^2\right)}{(1 - R_2C_2R_3C_3\omega^2)^2 + (R_2C_\Sigma + R_3C_3)^2\omega^2}\,d\omega$$

where $C_\Sigma = C_2 + C_3$. This corresponds to a voltage noise $\delta V_{\mathrm{RMS}} = 0.7\,\mathrm{nV}$.

In our experiment, the amplitude of this voltage noise δV_{RMS} will result in a frequency noise σ_f in the emitted radiation. Assuming Gaussian fluctuations $\propto e^{(f-f_0)/2\sigma_f}$, this will correspond to a frequency FWHM $\delta f_{\mathrm{RC}} = 2\sqrt{2\ln 2}\sigma_f \simeq 2.35\frac{\delta V_{\mathrm{RMS}}}{\Phi_0} = 800\,\mathrm{kHz}$.

Given the measurement uncertainties, this results is consistent with our measurement of $\delta f_{\mathrm{meas}} = 3\mathrm{MHz}$ presented in chapter 5.

One should note that we have neglected so far the influence of the Yokogawa voltage source noise. However, its contribution might be significant as the data-sheet gives a noise amplitude of 100 $\mu\mathrm{V}_{\mathrm{pp}}$ for a 10kHz bandwidth. This would correspond to an additional $\delta V_{\mathrm{RMS}} = 0.75\,\mathrm{nV}$ contribution on the noise, resulting in a total width of 1.2 MHz, which is in reasonable agreement with our measurements..

2.2 Radiation measurements

2.2.1 Low temperature amplification

Now that our sample has a clean sample biasing line, we characterize the radiation of the Josephson junction with power measurements. One photon at a frequency 4.4 GHz corresponds to a temperature of ~ 200 mK. As the signals that we want to measure are initially very small, we first need to amplify them.

We use HEMT low temperature amplifiers from LNF. They provide a

40 dB gain over the 4 to 8 GHz bandwidth. Its input/output signals can be described in terms of annihilation/ creation operators : a and $a^\dagger$ for the input line, f and $f^\dagger$ for the idler port associated to the intrinsic noise of the phase preserving amplifier, and A and $A^\dagger$ for the output signal of the amplifier.

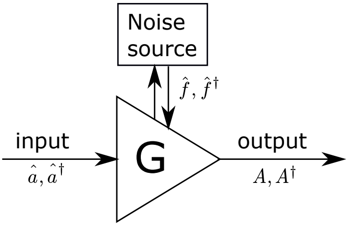

Figure 71. Amplifiers noise contribution on the output signal.

The output of the amplifier is then defined by its operators [17][40]

$$\begin{aligned} A &= \sqrt{G}a + \sqrt{G-1}f^\dagger, \\ A^\dagger &= \sqrt{G}a^\dagger + \sqrt{G-1}f \end{aligned} \tag{67}$$

where G is the gain of the amplifier.

The output voltage is then

$$V = A + A^\dagger = \sqrt{G}(a + a^\dagger) + \sqrt{G-1}(f + f^\dagger),$$

and as a and f commute, the associated power is

$$P_{T,A} = \langle A^\dagger A \rangle = G\langle a^\dagger a \rangle + (G-1)^2 \langle f^\dagger f \rangle. \tag{68}$$

One should note that the output of the amplifier is now made of a huge number of photons so that ${}^{N+1}/_N \sim 1$ and can thus be considered as a macroscopic signal.

By performing correlation measurements at the output of the amplifier and removing all terms which do not preserve photon number, one obtains for the power fluctuations $\langle \delta P_A^2 \rangle$

$$\langle \delta P_A^2 \rangle \propto \langle A^\dagger A^\dagger A A \rangle - \langle A^\dagger A \rangle^2,$$

with

$$\langle A^\dagger A^\dagger A A \rangle = G^2 \langle a^\dagger a^\dagger a a \rangle + (G-1)^2 \langle f^\dagger f^\dagger f f \rangle + 2G(G-1) \langle a^\dagger a \rangle \langle f^\dagger f \rangle.$$

This is obviously different from $\langle a^\dagger a^\dagger a a \rangle$ that we want to access. As these amplifiers have a noise temperature of ∼2 K (see Sec. 2.3.2), $|f| \gg |a|$.

The $\langle f^\dagger f^\dagger f f \rangle$ contribution from the amplifier noise can be easily removed by performing on-off measurements.

As the signal is a small (∼1%) contribution P_S on top of the amplifier noise P_N, the calculated correlator is mainly accounted for by the first moment contribution $\langle a^\dagger a \rangle$. We will present in details in section 1.1, a way to circumvent this effect by using a beam splitter and performing Hanbury-Brown and Twiss like experiment.

In addition, this noise is also present at the input of the amplifier. In order to prevent the amplifier to shine thermal radiation on the sample, we use 4 circulators as isolators, which provides more than 60dB isolation.

2.2.2 Cold Stage set-up

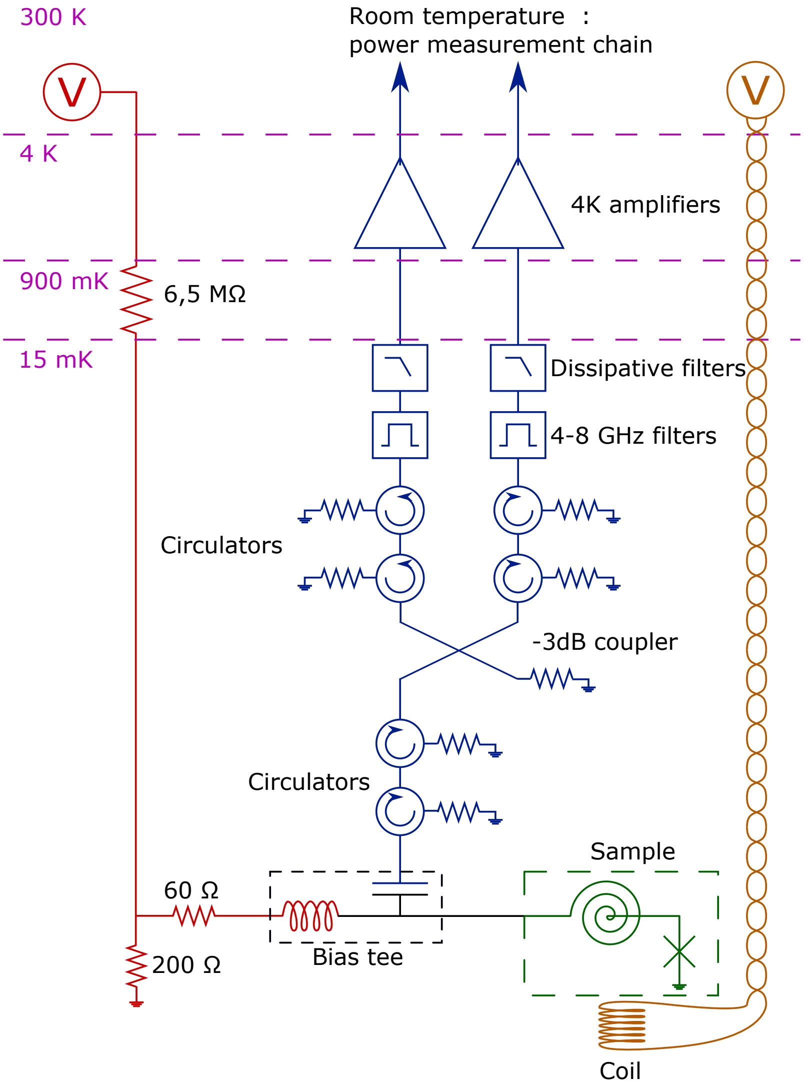

Figure 72. Wiring of the cold part of the experiment : The sample (green) is biased through a voltage divider (red). The outgoing microwave signal, emitted by the sample, is filtered and amplified (blue). The flux through the SQUID loop is tuned with a small coil on top of the sample (orange). Unlabeled resistors are 50Ω loads connected to ground.

The reference of the elements are listed in table 7. In addition with all the previously mentioned devices, the circuit has:

- a twisted pair of cables to feed a coil on top of the sample box holder. This allows to modulate E_J by changing the magnetic field.
- $4-8$ GHz and dissipative filters to remove any out of band contribution at the input of the amplifiers.
- Copper powder filters on the dc line

element	reference
Bias tee	SHF BT 45B 40873 20kHz-40GHz /16V, 0,4A
-3dB coupler	Pulsar QS2-05-463/2
double circulator : - before splitter - after splitter	Quinstar : QCY060400C020 QCY060400CM20
dissipative filters	Marki FX0109
4-8 GHz filters	Microtronics BPC 50403
amplifiers	LNF LNC4_8A
Cu powder filter	0.3Ω / 350pF

Table 7.

With this cold stage set-up, we voltage bias the sample with extremely low noise and measure its microwave emission on top of the amplifiers noise at the output of the fridge.

2.2.3 Spectral power measurement

In a first step, we measure the power emitted by the sample without performing correlation measurements, as done by Hofheinz and coworkers [41], but without current measurement. We use the set-up shown in Fig. 73.

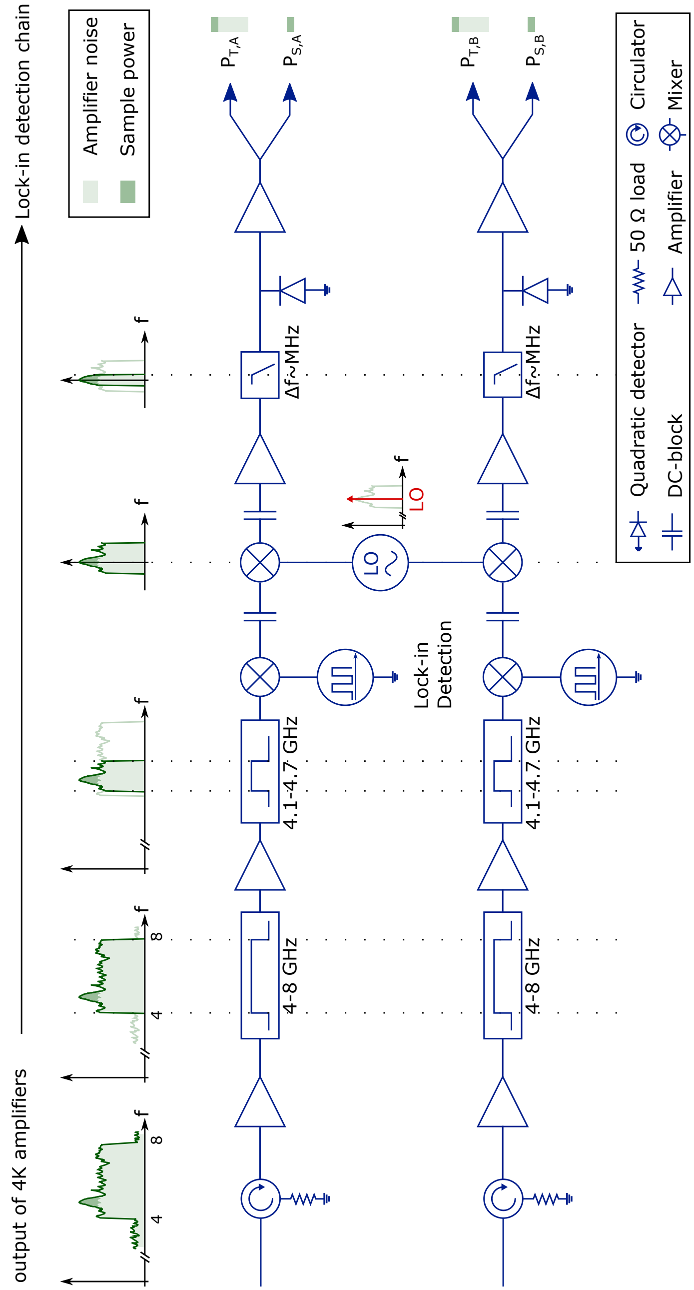

Figure 73. Room temperature microwave set-up for power measurements.

The references of the elements used in the room temperature microwave set-up are listed in table 8 :

- First, at the output of the fridge the signal goes through an isolator to avoid shining noise from 300K amplifiers back to the fridge.
- The signal is once more filtered and amplified in the $4-8\,\mathrm{GHz}$ band. As our resonator frequency is $4.4\,\mathrm{GHz}$, we add a second step of filtering to get rid of amplifiers noise.
- Then we use a first mixer as a chopper to perform homodyne detection with lock-ins. To do so, we use Marki mixers and connect the low frequency port to a MHz square source. The input/output signals are connected to the LO and RF port of the mixer.
- In order to be able to tune measurement frequency and bandwidth, we down-convert the signal with a second stage of mixers (Miteq). We use an RF source from Rhode and Schwartz as a local oscillator and filter the output of the mixer with a low-pass filter Δf.
- Finally, we perform power measurement using quadratic detectors, amplify the output voltage and send it to quadratic detectors to perform homodyne detection.

element	reference
$4-8\,\mathrm{GHz}$ filters	Microtronics BPC 142 44
$4.1-4.7\,\mathrm{GHz}$ filters	Microtronics BPC 188 98
$4.25-4.7\,\mathrm{GHz}$ filters	WI WTBCJV6 41254825 250 1100 50SS
Mixers (chopping)	Marki M80420LS-0409
Mixers (heterodyning)	MiteQ DB0218LW2
RF source	R&S SMR20
MHz sources (LI detection)	HP 3310B
	SRS DS 345
Quadratic detectors	Herotek DTM 180AA
Lock-in	SRS SR830 DSP

Table 8.

Quadratic detectors

Quadratic detectors consist of a resistor connected to a capacitance through a diode. To obtain the RMS value of the signal, the input voltage must stay well below the threshold voltage of the diode.

This kind of detector has two main drawbacks :

- due to the finite charging time the capacitance, they do not follow power fluctuations above a certain frequency

– a voltage over which they become nonlinear.

The maximum input voltage to achieve 1% precision is typically $0.2\,v_0$, with $v_0 \sim 26\,\mathrm{mV}$.

When a voltage $V = V_{\mathrm{in}} \cos(\omega_0 t)$ is applied to the diode, the output of the detector, charged by a resistance R_L is then

$$V_{\mathrm{out}} = R_L\, I_{\mathrm{sat}} \frac{V_{\mathrm{in}}^2}{v_0^2}$$

where I_{sat} is the saturation current of the diode. This value is in fact proportional to S_{II}. We use two types of quadratic detectors :

- Slow Quadratic detector : low cut-off frequency : 1 MHz

  they are used to measure the average power on each line.

- Fast Quadratic detectors : rising time of 0.6ns (1 ns, according to their specifications). They are used to perform cross correlation measurements and their output power is given by Fig. 74.

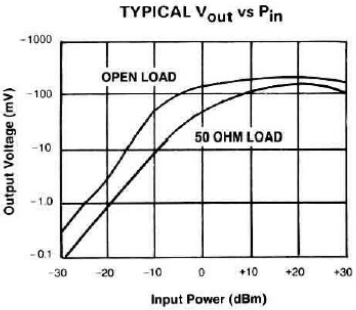

Figure 74. Quadratic detector linear behavior range.

(reproduced from Herotek data-sheet)

Homodyne detection

The output voltage of the quadratic detector is proportional to the emitted power and is amplified with a 20 dB gain amplifier. Each line is then split and measured with two lock-in detectors as shown in Fig. 73.

- The first one is synchronized with the first mixer of the warm chain to perform standard homodyne detection and gives access to the total power : $P_{T,A/B} = P_{N,A/B} + P_{S,A/B}$.
- The second one is synchronized with a TTL signal chopping the biasing line, which allows to measure the excess noise coming from the sample when the bias is applied : $P_{S,A/B}$.

The typical frequencies that we used were ~120 Hz for the TTL and several MHz for the mixers.

The main contribution to the total power $P_{T,A/B}$ is the power associated with the noise contribution of the cold stage amplifiers $P_{N,A/B}$. We assume that the temperature associated to this value stays constant over time and that the fluctuations of the total power are due to fluctuations of the gain. As a consequence, the ratio $P_{S,A/B}/P_{N,A/B}$ is thus directly related to the power emitted by the sample.

In the Shot Noise regime, where the power emitted by the sample is well defined, the ratio between these two powers allow us to calibrate the whole measurement chain (see Sec. 2.3.2)

2.3 Calibrations

Before performing the power fluctuation measurements to access $g^{(2)}(\tau)$, we calibrate the gain of our detection chain and characterize the electromagnetic environment of the junction.

The main parameters of the sample that we have measured are

Name	f_0	FWHM	Q
Lores_Quartz2_C5	4.41 GHz	130 MHz	34
	Z_C	R_N (300K)	$Z_{C\lambda/4}$
	2.05 $k\Omega$	230 $k\Omega$	70 Ω

Table 9. Main characteristics of the measured sample.

By performing on-off measurement, chopping the bias of the junction, we measure the excess noise P_S coming from the sample when a voltage bias is applied.

2.3.1 Shot Noise calibration

We first voltage bias the Josephson junction above the gap $\mathrm{eV} > 2\Delta$, so that it acts as a white noise source, as shown in section 5. The power spectral density emitted by the sample is then

$$S_{\mathrm{II}}(\omega) = 2\mathrm{eV}\Gamma(\omega), \tag{69}$$

where $\Gamma(\omega)$ is the coupling coefficient between the junction and the resonator.

Coupling coefficient

Shot noise measurement thus give access to the coupling coefficient between the Josephson junction and its single mode environment [67] which is related to its impedance

$$\Gamma(\omega) = \frac{4\mathrm{Re}(Z_{\mathrm{env}}(\omega))R_T}{|Z_{\mathrm{env}}(\omega) + R_T|^2} \tag{70}$$

where $Z_{\mathrm{env}}(\omega)$ is the impedance of the environment and R_T, the normal tunnel resistance of the Josephson junction. As this resistance was measured at room temperature, we consider that it increases by 17% at low temperature, according to previous experiments [35][65].

Using Eq. 69, the associated power measured by the quadratic detectors is

$$P_S = 2\mathrm{eV}\Gamma(\omega)\delta f \tag{71}$$

where δf is the bandwidth of the power measurement chain.

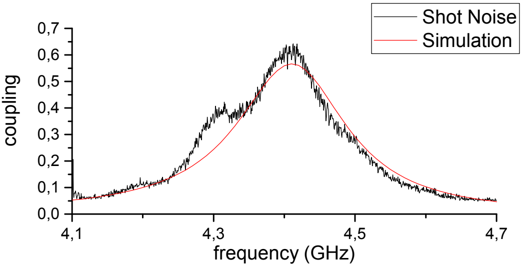

Figure 75. Coupling $\Gamma(\omega)$ for $V = 990\mu V > 2\Delta$: Shot Noise measurement (black line) compared with simulation results (red line)

In order to measure the emission spectrum, we sweep the frequency of the heterodyning source and filter the signal with a narrow bandpass filter (Fig. 73) or directly measure the emission spectrum with a spectrum analyzer.

From this measurement presented in fig. 75 (black line), we extract the resonant frequency $f_0 = 4.41$ GHz. The coupling $\Gamma(\omega)$ extracted from simulations using equation 70 is compared to the experimental results in Fig.75.

To extract the effective coupling from the data, we fit the emitted power with a Lorentzian and assume that its maximum matches the simulation.

2.3.2 Noise temperature of the cryogenic amplifiers

The second goal of this calibration step is to determine the total gain of the chain, i.e. to convert an output quantity : the power measured by the quadratic detectors, into an absolute quantity : photon emission.

The main contribution to the power is the intrinsic noise of the cryogenic amplifier as described in section 2.2.1. This noise power can be associated with a noise temperature T_N so that $P_{N,A/B} = 4k_B T_{NA/B}$.

In order to calibrate the equivalent temperature of the two cold amplifiers, we measure both the total power $P_{T,A/B}$ and the excess power $P_{S,A/B}$ emitted in the whole resonator, assuming a constant noise temperature over its bandwidth.

Sweeping the voltage bias across the junction above the gap

$$2\mathrm{eV} > 2\Delta \sim 360\,\mu V\,,$$

we measure the excess noise power coming from the sample as shown in Fig. 76.

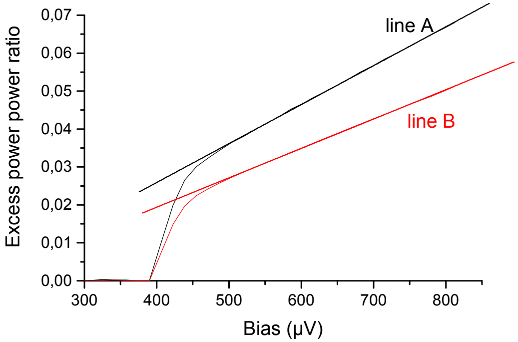

Figure 76. Excess power emitted by the Josephson junction in the two measurement lines as a function of bias voltage.

As this excess power is well defined by equation 71, it is used as a calibration to extract the noise temperature of the two amplifiers $T_{NA/B}$

$$T_{NA/B} = \frac{2\mathrm{eV}\Gamma}{4k_B\,{}^{P_{S,A/B}}/_{P_{N,A/B}}}$$

where $P_{S,A/B}$ is the excess power coming from the sample and $P_{N,A/B}$ is the power measured at zero applied dc voltage, corresponding to intrinsic noise of the amplifiers.

By measuring the slopes, as shown in Fig. 76, we extract the noise temperature of the two amplifiers referred at the output of the sample that are given in table 10.

Noise temperature as seen from the sample	Amplifier reference LNF :
$T_{\mathrm{NA}} = 11.4\mathrm{K}$	LN8CA - SN 067
$T_{\mathrm{NB}} = 15.1\mathrm{K}$	LN8CA - SN 070

Table 10.

These values are consistent with the ∼2 K noise temperature of the amplifiers combined with the attenuation of the various components inserted between the sample and the amplifiers as presented in the cold stage Fig. 72 of section 2.2.2. This includes the insertion losses of the 4 circulators, the small attenuation of the 12 GHz low pass filters, and the 3dB due to the splitter.

Since the amplifiers noise temperature is stable over the duration of the experiments, we use the background noise of the amplifier as a power reference. Using all calibrations, we extract the photon emission rate in the Dynamical Coulomb Blockade regime as

$$\Gamma = \frac{P_S}{P_N}\frac{T_N}{\hbar\omega_0}\delta f.$$

5 Power spectrum measurements

The main goal of this thesis is to characterize the statistics of photons emitted by a Josephson junction strongly coupled to a single mode environment. This requires power fluctuation measurements using a Hanbury Brown and Twiss set-up as discussed in chapter 4.

We first characterize the spectral density of the radiation emitted by the Josephson junction, which is equivalent to measuring $g^{(1)}$, before performing power fluctuation measurements in the single photon peak to obtain $g^{(2)}$.

We also investigate in this chapter new features that appear in the strong coupling regime. We observe in particular processes involving the simultaneous emission of up to 9 photons by a single Cooper pair as well as the renormalization of E_J, which goes beyond the standard

$P(E)$ theory of Dynamical Coulomb Blockade.

1 Single photon peak

The spectrum of the radiation emitted by the junction when the voltage is swept around the single photon resonance is shown in Fig. 77. According to section 3, the Josephson junction emits single photons at the Josephson frequency $f = (2e/h)\,V$. When this frequency matches the resonance, one observes a single photon emission peak, leaking in the measurement line.

This map of Fig. 77. was taken at a low enough value of E_J for which the $P(E)$ theory is expected to account for the emitted radiation as tested further below.

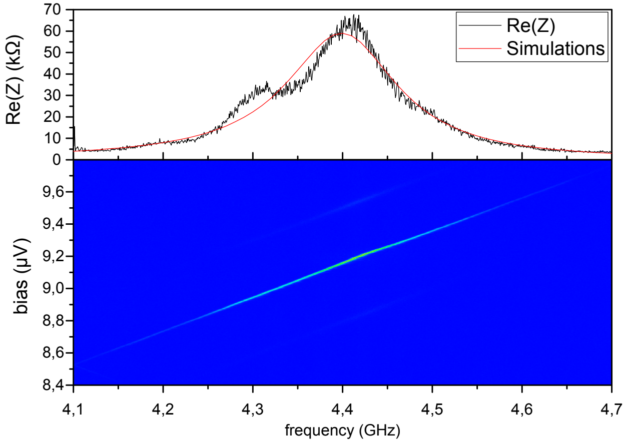

Figure 77. Single photon emission. Bottom : Map of the radiation emitted by the Josephson junction when the voltage is swept around $V = (h/2e)\,f_0$. Top : Black line : the extracted impedance of the environment assuming that the emitted power follows the $P(E)$ theory as described in section 1.3. Red line : Sonnet simulation of the circuit geometry.

1.1 Characterization of dc voltage noise

Given the bias voltage noise directly affects the emission frequency, our experiment requires a careful filtering of the biasing line so that voltage fluctuations δV (coming either from thermal fluctuations or parasitic noise) induce frequency fluctuations δf significantly smaller than the spectral width of the resonator.

In order to estimate the voltage noise on the line, we use two methods :

- we bias the junction with a fixed voltage and measure the emission spectrum. The result for different values of E_J is shown in Fig. 78 (left) and give a bandwidth δf_{meas} of $3-5$ MHz, which corresponds to a $\delta V_{\mathrm{RMS}} \sim 2.5\,\mathrm{nV}$.
- Using heterodyning and filtering the signal in a 10 MHz bandwidth, we select a narrow frequency band and sweep the bias across the junction as shown in fig. 78 (right) and we measure the frequency noise with a quadratic detector. As the quadratic detector has a low frequency cut-off, we cannot reduce the filtering bandwidth down to a few MHz. We obtain $\delta V_{\mathrm{FWHM}} = 0.03\ \mu\mathrm{V}$, which corresponds to $\delta f_{\mathrm{meas}} = 15$ MHz. Given the 10 MHz convolution from the filtering bandwidth, this value agrees with the direct spectral measurement.

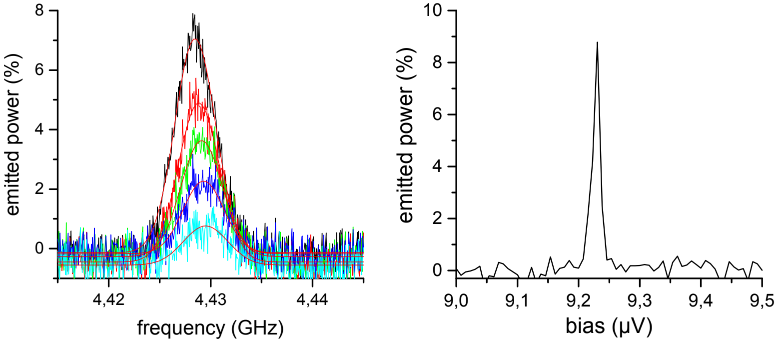

Figure 78. dc voltage noise characterization. Left : direct spectral analysis of the emitted radiation. Right : emitted power at a frequency f in a 10 MHz bandwidth when the bias voltage is swept around $(h/2e)f$.

In previous experiments using a similar set-up, the voltage noise corresponded to a 35 MHz frequency broadening [65]. This is why our sample was designed to have a FWHM frequency width of 130 MHz.

We attribute the reduction of the noise in the present experiment to improved filtering. Our sample with a quarter wave transformer, has a sizeably larger that the achieved technical broadening of 5 MHz. This low value could even allow narrower resonances.

1.2 Spurious environment modes due to the bias tee

Bias tees are made of inductive and capacitive elements, resulting in a RF self resonance which can also exchange photons with the Josephson junction. As these modes are of much lower impedance than the resonator, they are weakly coupled to the junction but result in small additional side-band peaks involving two photon processes, as shown in Fig. 79.

One observes 3 lines, which from bottom to top correspond to :

I. As the energy $2e\,V$ provided by a Cooper pair is $2e\,V < h\,f_0$, it can nevertheless emit a photon in the resonator by absorbing a photon from the bias-tee mode.

II. Dominant process : emission of a single photon in the resonator.

III. Simultaneous emission of one photon in the sample resonator and one photon in the bias-tee mode.

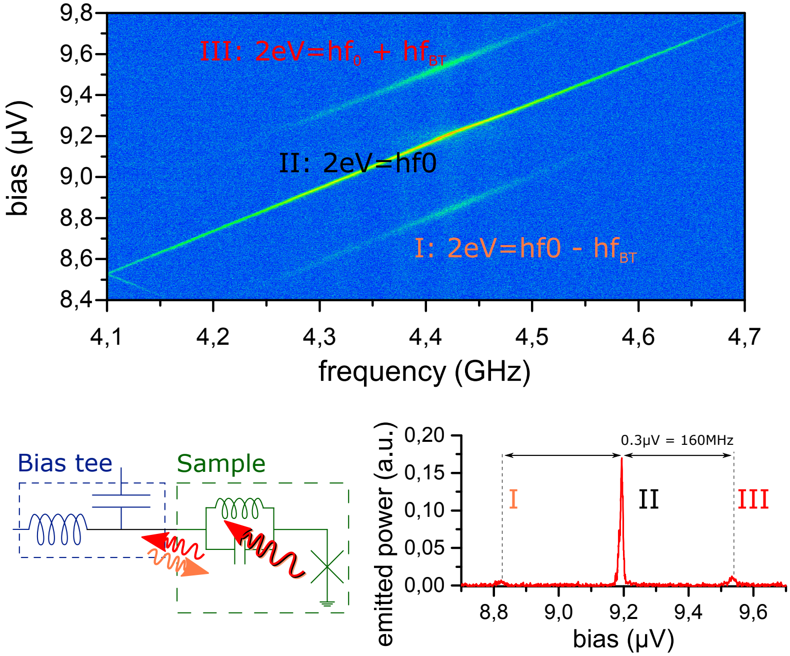

Figure 79. Effect of the spurious bias-tee mode on the emission spectrum. Single photon peak map (logarithmic scale). The two side-band peaks correspond to the simultaneous emission of a photon in the resonator associated with the absorption/emission of a photon from/in the 160 MHz bias-tee mode.

The resonant frequency of the parasitic low frequency mode, extracted from a cut of the map of Fig. 79, corresponds to $f_p = (2e\,/\,h)\delta V =$ 160MHz.

In addition, the mean thermal population n of the parasitic mode can be obtained from the ratio between emission and absorption side-bands $\frac{n+1}{n}$. The measured value 2.07 yields $n = 0.93$, which corresponds to a temperature of 15 mK, in good agreement with the fridge temperature.

1.3 Analysis of the single photon peak with the $P(E)$ theory : extraction of Re(Z_{env})

According to the $P(E)$ theory prediction of Eq. 49, the excess emitted power density is

$$S_{II}(\omega, V) = \frac{2\pi e^2 E_J^2}{\hbar} P_1'(\omega, V),$$

where $P_1'(\omega, V)$ corresponds to the probability to emit single photons in the environment. This probability described in section 3, is proportional to the real part of the impedance of the environment

$$P_1'(2\mathrm{eV} - \hbar\omega) \propto \mathrm{Re}[Z_{\mathrm{env}}(\omega)]\, \delta(2\mathrm{eV} - \hbar\omega).$$

Following the line $2e\,V = h\,f$ on the map of fig. 77, one can precisely reconstruct the profile of the environment.

We make the assumption that the noise temperature of the amplifiers is constant over the resonator bandwidth and correspond to the power P_N. The emitted power ratio $P_S\,/\,P_N$ measured in the map shown in Fig. 77 is then proportional to $\mathrm{Re[Z_{env}(\omega)]}$.

In order to obtain $\mathrm{Re[Z_{env}(\omega)]}$ from the data, we make the assumption that the integral of the emitted power ratio is equal to the integral of the simulation results. This procedure leads to the impedance shown on the top panel of Fig. 77 (black line). The extracted data summarized in table 11, matched simulation results (see Sec. 1).

f_0	Δf	Q	Z_{MAX}	Z_C	r
4.41 GHz	151 MHz	29	$59k\Omega$	$2.05k\Omega$	1.0

Table 11.

Consistency check with the coupling coefficient in Shot Noise measurements

The impedance of the environment was also characterized by the coupling coefficient $\Gamma(\omega)$ in Shot Noise power measurements in the normal state of the junction given by Eq. 70

$$\Gamma(\omega) = \frac{4\,\mathrm{Re}[Z_{\mathrm{env}}(\omega)]\,R_T}{|Z_{\mathrm{env}}(\omega) + R_T|^2}.$$

We extract the coupling coefficient from the measurement of $\mathrm{Re}[Z_{\mathrm{env}}(\omega)]$.

We compare in Fig. 80 the measured coupling coefficient, the coupling coefficient derived from the single photon peak analysis and using Eq. 70, and simulation results. The good agreement achieved is a consistency check of the global analysis framework.

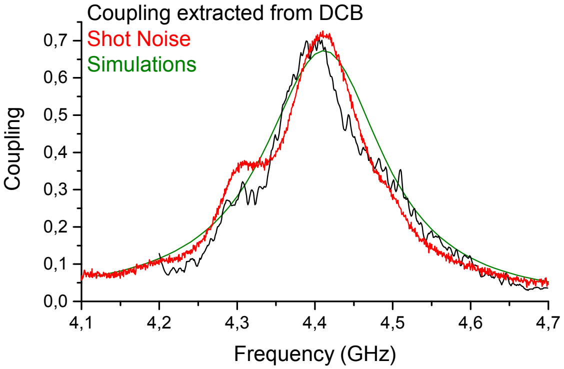

Figure 80. Comparison of the coupling coefficient measured in Shot Noise (red curve), derived from the single photon peak analysis (black curve), and simulation results (green curve).

1.4 Tuning the emission rate Γ with the flux

Previous results in this chapter were obtained at a fixed and small value of E_J. By modulating the flux Φ threading the SQUID [47], one can tune E_J over a large range, and thus the photon emission rate.

According to the $P(E)$ theory (Eq. 33), the emitted power should scale as $E_J^2(\Phi)$ and thus be proportional to

$$E_J^2(\Phi) = E_{J\,\mathrm{max}}^2 \cos^2\left(\pi \frac{\Phi}{\Phi_0}\right) \tag{72}$$

where Φ is the magnetic flux threading the coil and $\Phi_0 = h/2e$, the flux quantum.

In order to observe this modulation, we place the sample at the single photon resonance frequency $2e\ V = h\ f_0$, and collect the radiation emitted in the whole resonator as shown in Fig. 81 (black line). This modulation was compared to theoretical expectations (red line).

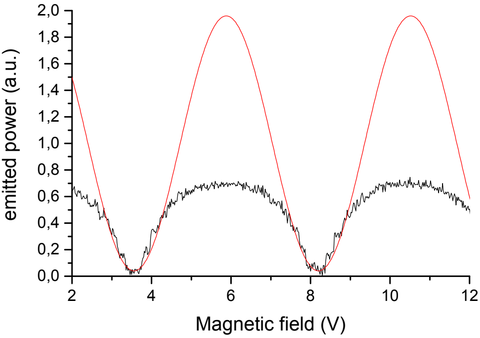

Figure 81. Power emitted by the single photon process as a function of magnetic field (black line) and rescaled theoretical prediction (red line).

The observed variation of the total emitted power with the flux does not scale as predicted by Eq. 72. One observe a saturation of the emitted power at large E_J which we attribute to the strong coupling regime reached in our experiment.

Our very symmetric SQUID allows us to reach low values of E_J, for which the $P(E)$ theory is valid as demonstrated in section 1.3. In addition, it allows us to reach the low mean photon occupation regime required for observing strong anti-bunching as discussed in section 5.5.

1.5 Characterization of $E_J(\Phi)$

The scaling of Eq. 72 should nevertheless be valid when $P(E)$ is small enough to fulfill the inequality (see Sec. 3.4)

$$E_J(\Phi)\, P(E) \ll 1.$$

To calibrate E_J in situ using the standard P(E) formalism, we bias the junction at a bias voltage corresponding to the upper end of the single photon peak region, at frequencies of $2e\,V\,/\,h = 4.512$ and 4.6 GHz, and filter with a narrow 10 MHz bandwidth. We then bias the junction at voltage corresponding to the peak frequency, with a bandwidth covering the whole resonance.

At the frequency f = 4.6 GHz, the real part of the impedance is $\mathrm{Re}[Z_{\mathrm{env}}(2\pi f)] \simeq 6\,\mathrm{k}\Omega$ (and $\mathrm{Re}[Z_{\mathrm{env}}(2\pi\,4.512\,10^9)] \sim 19\,\mathrm{k}\Omega$), which are respectively 3 and 10 times lower than the maximum impedance.

We measure the emitted power at 4.512 GHz and 4.6 GHz at a given bias voltage. However, these data cannot be directly used because the variations of the current with $E_J(\Phi)$ induce a voltage drop across the $60\,\Omega$ resistor of the biasing line, which yields to a small change in the Josephson frequency, but still larger than the narrow filter bandwidth.

Thus, we first measure a map of the emitted radiation as shown in fig. 82 in order to maintain the Josephson frequency in the filter bandwidth.

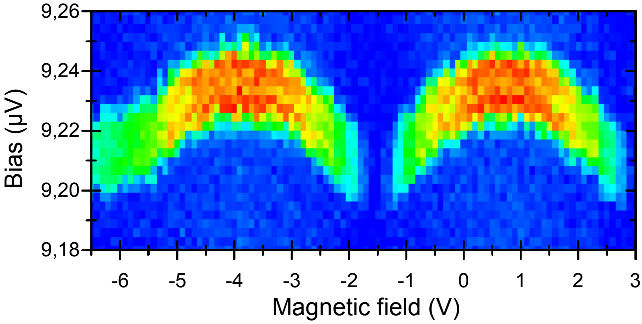

Figure 82. Voltage drop due to the $60\,\Omega$ resistance in series. For a frequency of 4.512 GHz with a filtering bandwidth of 10 MHz.

Note that this map, through the voltage drop, also gives access to the current through the junction.

By taking the maximum of emission for each flux in the map at 4.6 GHz, we obtained the corrected power shown in Fig. 83 (red curve).

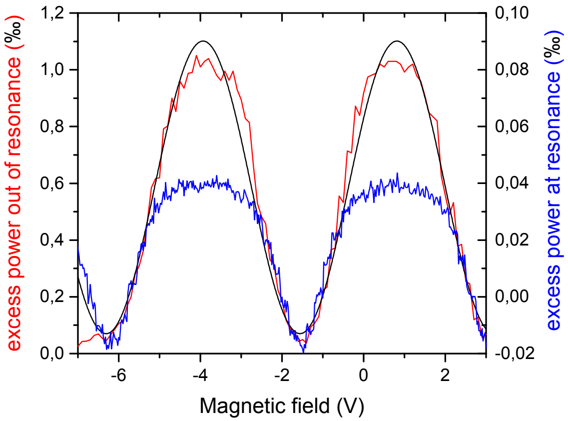

Measurment bandwidth:
side of resonance : 10MHz / center of resonator : 300MHz

Figure 83. E_J modulation by sweeping the flux through the SQUID. the blue curve corresponds to a polarization at the center of the resonator i.e. strong coupling whereas the black curve corresponds to photon emission on the side of the resonance (4.6 GHz). The red curve is the associated sinusoidal fit.

One observes that the emission on the side of the resonator (red curve) follows the $E_J^2(\Phi)$ scaling (black curve), in agreement with the $P(E)$ theory. At resonance, a similar measurement, in a larger bandwidth for the sake of simplicity, shows a strong saturation of the excess power (blue curve) as already shown in Fig. 81.

According to recent theoretical works [50][1], the strong coupling regime leads to a saturation of E_J : when the parallel admittance of the junction becomes appreciable, it shunts the environment. This effect could possibly explain our results, and calculations are presently pushed forward (Philippe Joyez, private communication).

2 Multiple photon emission

We now focus on the regime where a single tunneling Cooper pair emits simultaneously several (k) photons in the environment. The power emitted in the measurement chain is then proportional to the photon emission rate $\Gamma^{\mathrm{Ph}} = k\Gamma^{\mathrm{Cp}}$. Assuming an infinite quality factor mode, the $P(E)$ theory yields

$$P_k = \pi^2 E_J^2 f_0 e^{-r} \frac{r^k}{(k-1)!}, \tag{73}$$

where f_0 is the resonant frequency of the mode, and r, the coupling constant.

2.1 Power spectrum of multiple photon processes

In a previous experiment of the group [41], a coupling factor of $r = 0.08$ was achieved. As a consequence, the second order peak amplitude was $1/12$ of the single photon peak and processes involving the emission of 3 or more photons were not measurable.

With a much larger coupling factor $r \sim 1$, higher order processes are observed as shown on the map in Fig. 84. In this measurement, we measure the spectral power emitted by the junction as a function of frequency while increasing the bias voltage up to $2eV = 4hf_0$, i.e. up to the four photon emission resonance.

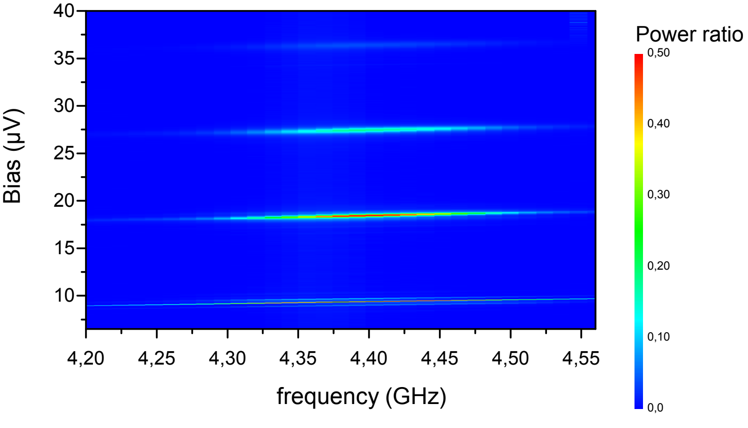

Figure 84. Multiple photon emission map: we measure the power associated to processes where a tunneling Cooper pair emits simultaneously up to 4 photons.

On the map of Fig. 84, the 4 lines correspond to the four processes $k = 1, ..., 4$.

One observes that the multi-photon process lines are broader than the single photon line. This is due to the fact that for higher order processes, the previous condition $\delta(2\mathrm{eV} - h\ f)$ becomes $\delta(2\mathrm{eV} - h\ f_1 - .... - h\ f_k)$. For example, the emitted power at a fixed voltage for the two photon process is proportional to

$$P_2(V) \propto \int_{\mathrm{BW}} \mathrm{Re}(Z(\omega_1))\mathrm{Re}(Z(\omega_2))\,\delta(2\mathrm{eV} - \hbar(\omega_1 + \omega_2)).$$

This implies that the frequency of the emitted photons can be slightly different from $2e\,V / k\,h$, as long as the sum of their energies are equal to $2e\,V$ as shown in fig. 85.

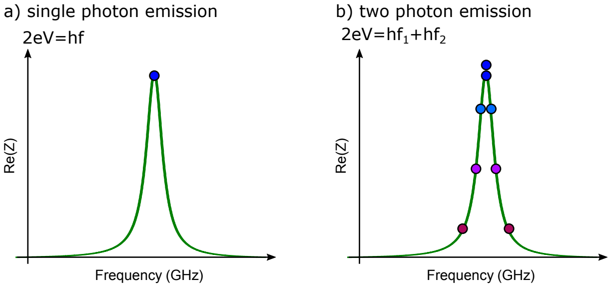

Figure 85. contributions to the emitted power. Left : Single photon emission peak, the spectral width is given by the voltage noise on the biasing line. Right : at a given voltage, 2 photon processes can lead to emission at different frequencies. The cartoon illustrates the case $\omega_J = \omega_0$.

This predicts that the peaks corresponding to two photon are broader that the single photon peak, as observed. The width of the multiphoton peak is given by a (multiple) convolution of the mode impedance shape.

At large values of E_J, the emitted power is large and the signal to noise ratio is optimum. Integrating the power emitted in the whole resonator bandwidth (from 4.1 to 4.7 GHz) and increasing the bias voltage across the junction, we observe up to 9 photon processes as shown in Fig. 86 .

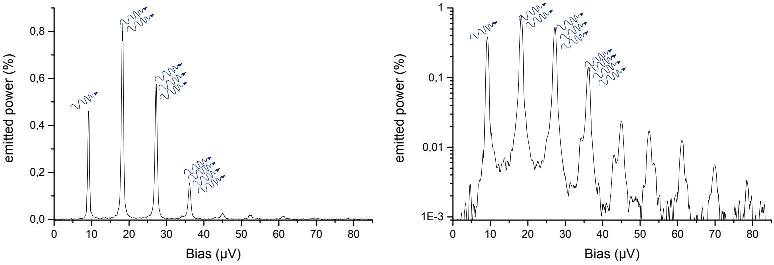

Figure 86. Multiphoton processes. Emitted power integrated over the resonator bandwidth (Linear and logarithmic scales) at the maximum value of E_J.

The integrated power of each peak is given in the table below :

1	2	3	4	5	6	7	8
9.99	22.73	16.90	5.45	1.28	0.88	0.50	0.19

Table 12.

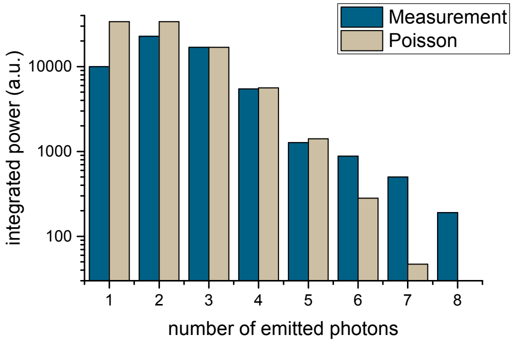

Figure 87. Integrated power of k photon emission (green bars) and fit with the $P(E)$ theory with $r = 1$ and an adjustable scaling factor (grey bars).

2.2 Attempt to extract of the coupling factor from multiphoton peaks

According to the $P(E)$ theory, the amplitude of the integrated peaks P_k shown in Fig. 87 should scale like E_J^2 and obey a poissonian law

$$P_k \propto E_J^2 e^{-r} \frac{r^k}{(k-1)!}. \tag{74}$$

At large values of E_J, the amplitude of the peaks in Fig. 87, cannot be fit by Eq. 74. We nevertheless compare with a fit using the coupling factor r obtained from the measurement of the environment impedance in the single photon regime (sec 1.3).

We observe that few and several photon processes do not accurately follow the predictions of the $P(E)$ theory. In particular, one observes that the high order peaks are significantly larger.

2.3 Effect of strong coupling on multiphoton peaks

We first investigate if the breakdown of the E_J^2 scaling observed on the single photon peak in section 1.5 also occurs on higher order processes. To do so, we measure flux modulation for the 3 and 4-photon peaks as shown by Fig. 88.

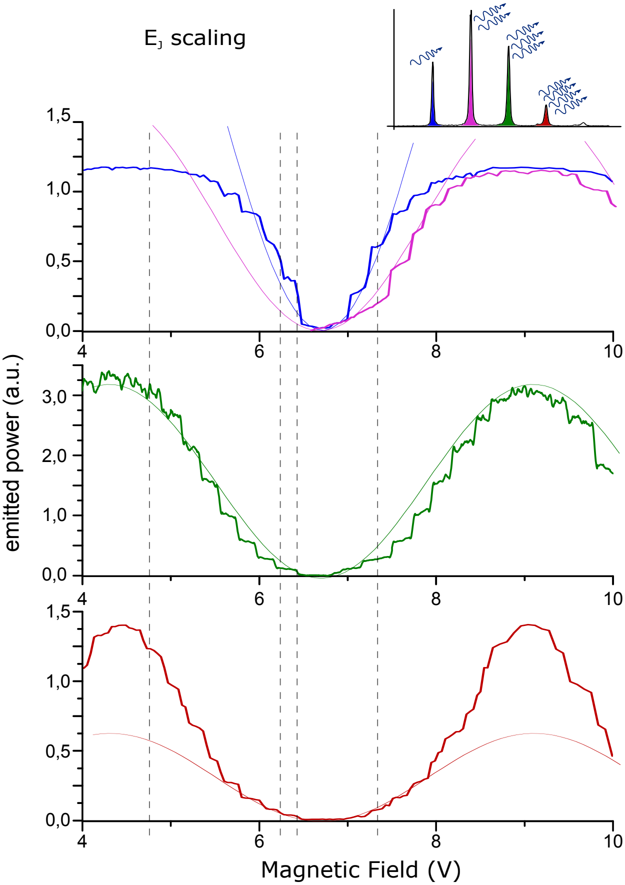

Figure 88. Evolution of the photon emission power with magnetic field for single (blue line), two(pink line), three (green line) and four photon processes (red line). The three photon process is the only one which scales like E_J^2 predictions (black line). The grey dashed lines correspond to the values of E_J used in Fig.89 .

One observes that the single and 2-photon peaks show a saturation at large E_J, that the 3-photon peaks follows the E_J^2 flux modulation predicted by the $P(E)$ theory, and that the 4 photon process is enhanced at large E_J. We now discuss these different phenomena.

2.3.1 Single and two photon processes : emission saturation

We now compare the relative peaks height up to the four photon process at a few different values of E_J as shown in fig. 89. As the amplitude of the peaks significantly increases with E_J, the results are normalized with the 3 photon peak which follows the E_J^2 prediction of the $P(E)$ theory.

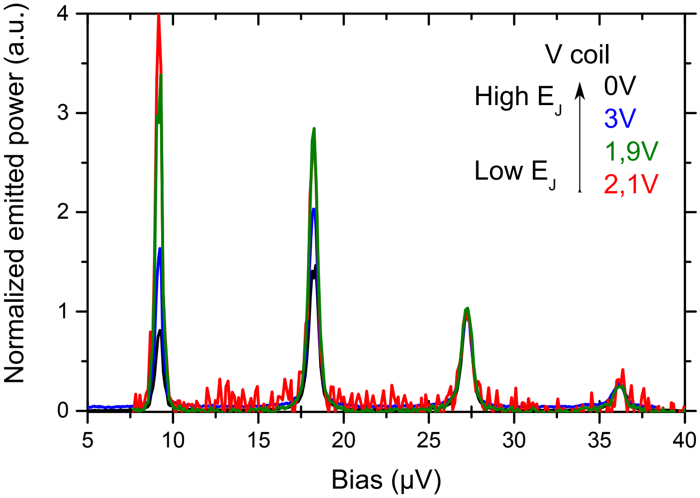

Figure 89. Single to 4-photon peak amplitude at different values of E_J normalized by the 3-photon peak that scales as E_J^2.

One can see in fig. 89 that the 1 and 2 photon peaks are saturated at large couplings.

We attribute this saturation to a shunt of the environment by the Josephson junction. Indeed, the junction adds an effective admittance in parallel with environment whose value increases with E_J. Calculations are currently performed in order to evaluate this effect. (Philippe Joyez, private communication).

2.3.2 High order processes : enhanced emission

In Fig. 87, one has seen that high order processes do not behave as predicted by the $P(E)$ theory. We now focus on this regime and show in Fig. 90 the power emitted by the processes involving the emission of 5 to 9 photons.

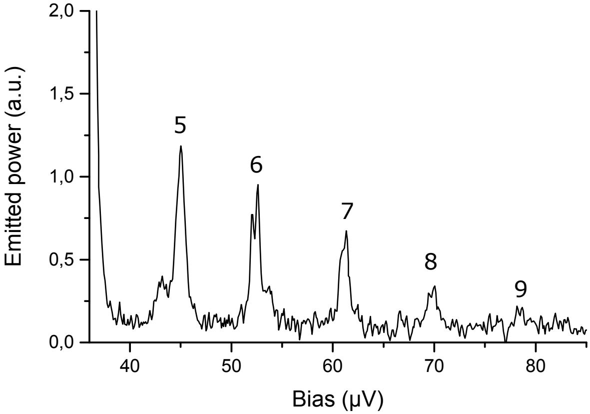

Figure 90. Evolution of the amplitude of photon emission from 5 to 9 photon emission peaks.

These k order processes do not follow the $P(E)$ theory scaling $r^k/(k-1)!$.

The ratio between the single and 8 photon peaks is 50, whereas the scaling of Eq. 74 predicts 5 000 for a coupling constant $r\sim 1$, i.e. a two orders of magnitude discrepancy.

We tentatively attribute this effect to a stimulated emission phenomenon as described by the cartoon of Fig. 91 and presented in [63].

Let us assume that the resonator is initially empty : $n=0$. A first Cooper pair tunnels and emits k photons in the resonator. These photons leak one by one in the measurement line with a characteristic timescale Q/ω_0. At a time $t+\tau$, p photons remain in the resonator and the decay rate in the cavity is thus $\Gamma^{\text{leak}} = p\omega_0/Q$.

The rate Γ^{Cp} associated with the tunneling of a second Cooper pair is given by

$$P_{p\rightarrow p+k} = E_J^2 \frac{p!}{(p+k)!}\left(\frac{r}{2}\right)^k e^{-r}|L_p^k(r)|^2,$$

increasing the number of photons, from $n = p$ to $n = p + k$. These two transition rates are in competition and can lead to an out of equilibrium population state of the resonator. This process might induce stimulated tunneling of Cooper pairs and the associated enhanced photon emission. We attribute this enhanced emission to the appearance of a lasing regime.

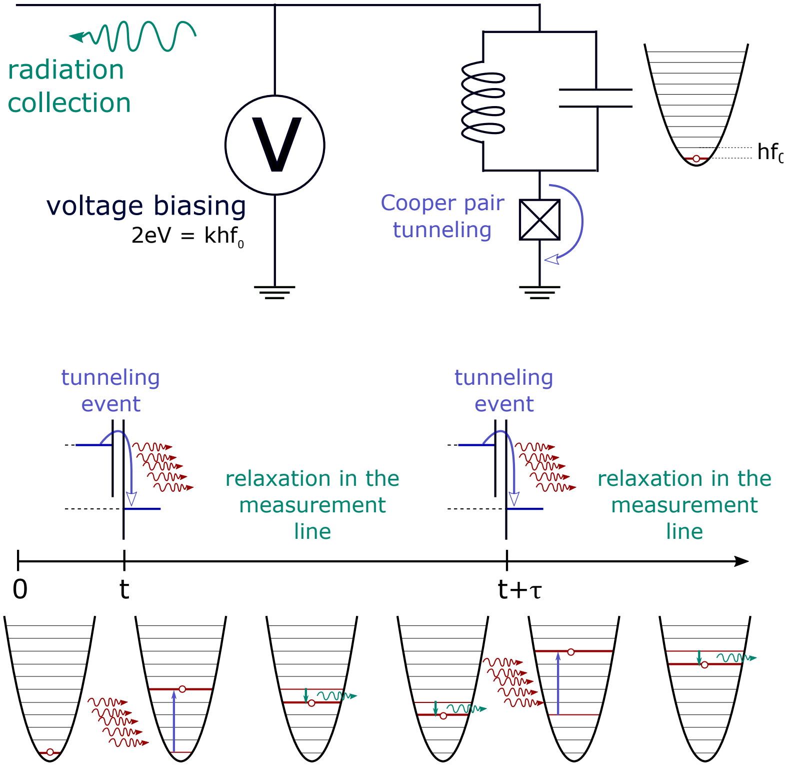

Figure 91. Lasing regime principle. When a Cooper pair tunnels, emitting several photons in the resonator, they leak one by one in the measurement line at a rate given by $\Gamma^{\text{leak}} = p\omega_0/Q$ where p is the number of photon in the resonator. The ratio between Cooper pair tunneling rate Γ^{Cp} and the photon leak rate Γ^{leak} can lead to a divergence of the population in the resonator and thus, to parametric resonance as detailed in [63].

6 Statistics of the emitted radiation

1 Correlation measurement set-up

In order to access the statistics of the emitted radiations, we measure correlators. As discussed in section 2.2.1, the low temperature amplifiers add noise to the signal, that prevents us to directly access the quantum correlators. Our $g^{(2)}$ measurement thus requires interferometric measurements *à la* Hanbury-Brown and Twiss.

1.1 Hanbury-Brown and Twiss set-up for microwaves

To get rid of any measurement chain influence, the sample is connected to a microwave Hanbury-Brow and Twiss (HBT) set-up [39][78] : the radiation leaked by the resonator is split between two path before the first stage of amplification. Correlation measurements are then performed between the output of the two amplifiers.

The beam splitter we use for our HBT set-up is an -3dB hybrid coupler: it consists in a four port microwave device comprising two input and two out ports. Half of the power impinging on each input port is distributed between the two output ports. It can be described by an electromagnetic unitary scattering matrix which can be directly used to express the output field operator as a function of the two input field operators (see Fig. 92.).

$$\hat{c} = \frac{\hat{a} + i\,\hat{b}}{\sqrt{2}} \quad ; \hat{d} = \frac{\hat{a} - i\,\hat{b}}{\sqrt{2}} \tag{75}$$

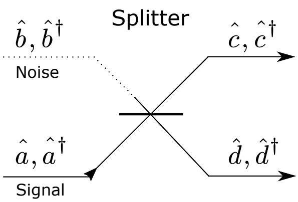

Figure 92. Quantum description of the beam-splitter.

One can easily show that this ensures that $\hat{c}$ and $\hat{d}$ have the same commutation relations that $\hat{a}$ and $\hat{b}$.

$$[\hat{c},\hat{d}] = [\hat{a},\hat{b}] = 0,$$

$$\left[\hat{c},\hat{d}^\dagger\right] = 0,$$

and

$$[\hat{c},\hat{c}^\dagger] = \left[\hat{d},\hat{d}^\dagger\right] = 1.$$

In our experiment, the b port is connected to a 50 Ω load thermally anchored to the fridge dilution chamber, so that we can assume that $\left\langle \hat{b}^\dagger\hat{b}\right\rangle = 0$. Then, we amplify the two split lines, as described in section 2.2.1 (see Eq. 67) and shown by Fig. 93.

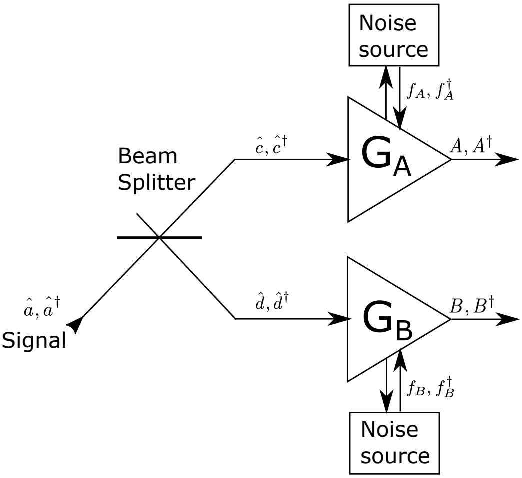

Figure 93. Measurement scheme. Splitting the signal before amplification prevent pollution from the amplifier noise.

Performing a cross-correlation measurement at the output of the two lines, one obtains

$$\langle A^\dagger B^\dagger \mathrm{BA}\rangle - \langle A^\dagger A\rangle\langle B^\dagger B\rangle = G_A G_B\left(\langle c^\dagger d^\dagger d c\rangle - \langle c^\dagger c\rangle\langle d^\dagger d\rangle\right).$$

When we take in account the contribution of the beam splitter and extract this correlator directly as a function of the signal emitted by the sample we obtain

$$\langle A^\dagger B^\dagger B\, A\rangle - \langle A^\dagger A\rangle\langle B^\dagger B\rangle = \frac{G_A G_B}{4}(\langle\hat{a}^\dagger\hat{a}^\dagger\hat{a}\hat{a}\rangle - \langle\hat{a}^\dagger\hat{a}\rangle^2). \qquad (76)$$

In order to extract the second order correlator $g^{(2)}(\tau)$ defined in chapter 2, our signal is split directly after the bias-tee as shown by the cold stage set-up of Fig. 72 and we perform cross-correlation measurements between the output power fluctuations of the two lines with a delay τ

$$\begin{aligned}\langle A^\dagger(t)B^\dagger(t+\tau)B(t+\tau)\, A(t)\rangle - \langle A^\dagger(t)A(t)\rangle\langle B^\dagger(t+\tau)B(t+\tau)\rangle \\ = \frac{G_A G_B}{4}(\langle\hat{a}^\dagger(t)\hat{a}^\dagger(t+\tau)\hat{a}(t+\tau)\hat{a}(t)\rangle - \langle\hat{a}^\dagger(t)\hat{a}(t)\rangle^2).\end{aligned}$$

This measurement removes all $\left\langle f^\dagger_{A/B} f_{B/A}\right\rangle$ contributions as the noise of the two amplifiers are uncorrelated. This directly gives access to $g^{(2)}(\tau)$ according to Eq. 68

$$\begin{aligned} g^{(2)}(\tau) &= \frac{<\hat{a}^\dagger(t)\hat{a}^\dagger(t+\tau)\hat{a}(t+\tau)\hat{a}(t)>}{<a^\dagger a>^2} \\ &= 1 + \frac{<\delta P_A(t).\delta P_B(t+\tau)>}{P_{S,A}.P_{S,B}}, \end{aligned} \qquad (77)$$

where $P_{S,A/B}$ is the excess power emitted by the sample.

To measure $g^{(2)}$, we need both $P_{N,A/B}$ and $P_{S,A/B}$, the average powers from the previous lock-in measurements and the correlator $<\delta P_A(t).\delta P_B(t+\tau)>$. These power correlation measurements are performed using quadratic detectors and a data acquisition board fast enough to catch the dynamics of these fluctuations.

Note that although the amplifier's noise does not contribute to the averaged signal, it still appears in individual measurements and determines our signal to noise ratio. The HBT set-up does not improve our signal to noise ratio, but the accuracy of our measurements. We further comment on this point in Sec. 1.3, where we determine the number of samples required to reach a given SNR.

1.2 Correlation measurement scheme

We perform correlation measurements of the radiation emitted in the whole resonator. To access both $g^{(1)}$ and $g^{(2)}$ at the same time, we perform Hong-Ou-Mandel experiment [44] and split the signal a second time in the warm chain, as described in Fig. 94 :

- The first line is sent to the two lock-in detectors to measure the emitted power. As we are interested in the power emitted in the whole resonator, we no longer implement a narrow filter by down conversion and low pass filtering but rather insert a 600 MHz filter wide enough to cover most of the resonator still reducing influence of the amplifiers noise.

- the second line is sent to a fast quadratic detector that can access the dynamics of the signal. Its output is sent to the acquisition board.

In order to optimize the signal to noise ratio, we use $\Delta f_1 = 600\,\text{MHz}$ and $\Delta f_2 = 350$ MHz bandpass filters around the resonator frequency 4.41 GHz. On the single photon emission peak, the power is emitted in bandwidth of 3 to 5 MHz and we catch all the emitted power with both filters. However, the correlator $g^{(2)}(\tau)$ involves 2 photon correlators associated with 2 CP tunnel events. As a consequence, we expect the fluctuations to scale as $\mathrm{Re}[Z_{\mathrm{env}}(\omega)]^2$. In order to estimate the amount of correlation that we loose die to the filters, we calculate the ratio

$$\frac{\int_{\Delta f} \mathrm{Re}[Z_{\mathrm{env}}(\omega)]d\omega}{\int_0^{+\infty} \mathrm{Re}[Z_{\mathrm{env}}(\omega)]d\omega}.$$

For $\Delta f_1 = 600\,\text{MHz}$, we miss 2.25% of the correlations and for $\Delta f_1 = 350\,\text{MHz}$, 5.9%.

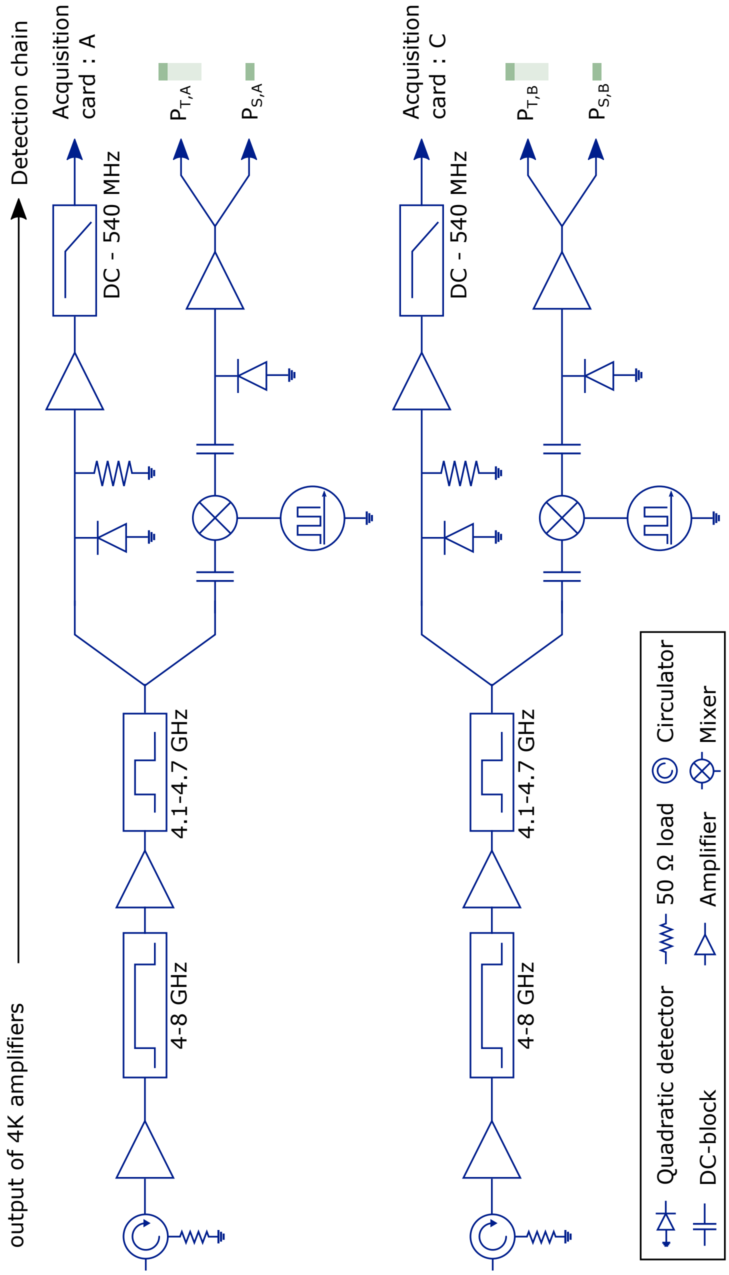

Figure 94. Warm chain scheme for correlation measurements.

1.3 Data acquisition board

In order to perform fast correlation measurement and access $\delta P_{A/B}(t)$, the output of the fast quadratic detectors are connected to the inputs of the *SP-devices* digitizing board whose characteristics are listed in table 13.

Sampling rate	1 / 2 Gsample/sec
channel	4 / 2 channels
range	from 100mV to 2V
dynamics of ADC	12 bits

Table 13. Data acquisition board characteristics.

The data are then transfered to a computer and we perform first and second order correlator calculations. As the bandwidth of the fast quadratic detector is ∼270 MHz, we use a 1 GHz sampling rate.

The amplitude of the measured signal is set by the power limit of the last stage amplifiers, corresponding to 200 mV. We tune the range of the board in order to exploit its full 12-bit dynamics.

Correlator calculation

The acquisition board records N samples on each line that are then transfered to the computer. In order to optimize calculation time, the array is then cut into chunks of 10 000 points. The calculation of the autocorrelations and cross-correlations are performed on each chunk and averaged.

cards output	correlator calculation results
$P_{A0}....P_{\mathrm{Ai}}...P_{\mathrm{AN}}$	$\mathrm{Auto}_A = \sum_{i=0}^{n} P_{\mathrm{Ai}}^2$
$P_{B0}....P_{\mathrm{Bi}}...P_{\mathrm{BN}}$	$\mathrm{Auto}_B = \sum_{i=0}^{n} P_{\mathrm{Bi}}^2$
	$\mathrm{Cross} = \sum_{i=0}^{n} (P_{\mathrm{Ai}} - \bar{P}_A)(P_{\mathrm{Bi}} - \bar{P}_B)$

Table 14. Correlator calculation. The output values of the acquisition card P_i corresponds to the output voltage of the quadratic detectors and are thus proportional to the emitted power.

These calculations are performed with or without bias voltage applied to the sample (corresponding to the upper indices B and 0). The global calculation rate, taking measurement and data transfer time in account was 100 MHz.

Our cross correlation measurements is performed on the total signal $P_{T,A/B}$ yielding

$$\overline{\delta P_A\,\delta P_B} = \overline{(P_{T,A} - \overline{P_{T,A}})(P_{T,B} - \overline{P_{T,B}})}. \tag{78}$$

On each individual measurement the emitted power is

$$P_{T,A/B} = P_{S,A/B} + P_{N,A/B} \tag{79}$$

where S and N stand respectively for contributions of the sample and the amplifiers. By replacing $P_{T,A/B}$ by Eq. 79 in Eq. 78 for a single measurement, one obtains

$$\delta P_A\,\delta P_B = \delta P_{S,A}\,\delta P_{S,B} + \delta P_{N,A}\,\delta P_{S,B} + \delta P_{S,A}\,\delta P_{N,B} + \delta P_{N,A}\,\delta P_{N,B}$$

Only the first of those four contributions will give no zero average value. However, each of them contribute individually. The variance of the measurement is given by the sum of the variances of each of the contributions and will be dominated by the amplifier's contribution $P_{N,A/B}$

$$\begin{aligned} \mathrm{Var}(\delta P_A\,\delta P_B) &= \mathrm{Var}(\delta P_{N,A}\,\delta P_{N,B}) \\ &= \mathrm{Var}(\delta P_{N,A})\mathrm{Var}(\delta P_{N,B}) \\ &= k_B^4\,T_{N,A}^2\,T_{N,B}^2\,\Delta f_A^2\,\Delta f_B^2. \end{aligned} \tag{80}$$

For a $g^{(2)}(\tau) = 0$, one expects

$$\overline{\delta P_A\,\delta P_B} = -P_{S,A} P_{S,B},$$

which corresponds to a signal to noise ratio (SNR) per measurement point

$$\begin{aligned} \mathrm{SNR} = \frac{S}{N} &= \frac{\mathrm{abs}(\overline{\delta P_A\, \delta P_B})}{[\mathrm{Var}(\delta P_A\, \delta P_B)]^{1/2}} \\ &= \frac{P_{S,A} P_{S,B}}{k_B^2 T_{N,A} T_{N,B} \Delta f_A \Delta f_B} \\ &= \frac{P_{S,A} P_{S,B}}{P_{N,A}\, P_{N,B}} \end{aligned} \tag{81}$$

We average the results over N samples. As the global SNR is proportional to $\sqrt{N}$, the total number of samples N that we need is

$$N = \frac{\mathrm{SNR}^2}{\left(\frac{P_{S,A}}{P_{N,A}}\right)^2 \left(\frac{P_{S,B}}{P_{N,B}}\right)^2}. \tag{82}$$

For a photon emission rate $\Gamma = 200$ MHz, the power emitted by the sample is 1% of the noise power of the amplifiers ($\delta P\, /\, P = 0.01$). Reaching a SNR of 10 thus requires to measure $N = 10^{10}$ data points.

As the number of points N scales with the emission rate as $1/\Gamma^4$, we can measure correlators down to 50 MHz emission rates, which already corresponds to a 14 hours measurement.

Second order correlator $g^{(2)}(\tau)$

The second order correlator $g^{(2)}(\tau)$ is defined in terms of power fluctuations by Eq. 77. It can be calculated using the output of the acquisition board and the lock-in measurement chains according to

$$\mathrm{Cross} = <\delta V_A . \delta V_B> = G_A\, G_B < \delta P_A . \delta P_B >$$

$$\mathrm{Auto}_{A,B} = <V_{A,B}^2> = G_{A,B}^2 < \delta P_{A,B}^2 >$$

where $G_{A/B}$ is the total gain of the chain. We then have for power correlations

$$<\delta P_A.\delta P_B> = \frac{\text{Cross}}{K_A\, K_B} = \frac{\text{Cross}}{\sqrt{\text{Auto}_A\, \text{Auto}_B}}\sqrt{<\delta P_A^2><\delta P_B^2>}.$$

As we want to measure correlations from the emitted power in DCB regime, we will take $\text{Cross} = \text{Cross}^B - \text{Cross}^0$ to remove any parasitic contribution of the cross-correlation measurement.

To calibrate the chains total gain G_A and G_B, as we know the associated power fluctuations, we use the autocorrelation without bias on the sample $\text{Auto}^0_{A/B}$ and have

$$<\delta P_{A/B}^2> = 2\, k_B^2\, T_{N,A/B}^2\, \frac{\Delta f_{A/B}^2}{2}$$

with $\Delta f_{A/B}$, the measurement bandwidth of line A/B and $T_{N,A/B}$, the equivalent noise temperature of the low temperature amplifier, previously defined in section 2.3.2. We then obtain for power correlations

$$<\delta P_A.\delta P_B> = \frac{\text{Cross}^B - \text{Cross}^0}{\sqrt{\text{Auto}^0_A\, \text{Auto}^0_B}}\, k_B^2\, T_{N,A}\, T_{N,B}\, \Delta f_A\, \Delta f_B. \tag{83}$$

However, as the quadratic detectors are not infinitely fast compared to the signal fluctuations, we miss some power fluctuations as discussed in section 2.1. We thus add a correction factor K that will be characterize in the chain calibration yielding

$$<\delta P_A.\delta P_B> = \frac{\text{Cross}^B - \text{Cross}^0}{\sqrt{\text{Auto}^0_A\, \text{Auto}^0_B}}\, \boldsymbol{K}\, k_B^2\, T_{N,A}\, T_{N,B}\, \Delta f_A\, \Delta f_B. \tag{84}$$

The excess power coming from the sample in DCB regime $P_{S,A/B}$ is

$$\begin{aligned} P_{S,A/B} &= \frac{V^B_{\text{QD}} - V^0_{\text{QD}}}{V^0_{\text{QD}}}\, k_B\, T_{N,A/B} \Delta f_{A,B} \\ &= \frac{P_{S,A/B}}{P_{N,A/B}}\, k_B\, T_{N,A/B} \Delta f_{A,B}. \end{aligned} \tag{85}$$

where P_N is the contribution of the amplifiers noise and P_S, the excess noise emitted in DCB regime.

The only value affected by the delay τ between the two lines in the crosscorrelation $\mathrm{Cross}^B(\tau)$. Inserting the results of Eq. 84 and Eq. 85 in the definition of $g^{(2)}$ given by Eq. 77, we obtain

$$g^{(2)}(\tau) = 1 + K\,\frac{\mathrm{Cross}^B(\tau) - \mathrm{Cross}^0}{\sqrt{\mathrm{Auto}_A^0\,\mathrm{Auto}_B^0}}\,\frac{1}{{}^{P_{S,A}}\!/_{P_{N,A}}\;{}^{P_{S,B}}\!/_{P_{N,B}}}. \qquad (86)$$

In the following, we first perform measurement in Shot Noise to calibrate the whole measurement chain and then measure the statistic of the emitted photon in the single photon emission peak.

2 Calibration procedures

We first use the noise temperature of the amplifiers to calibrate our measurement set-up. In a second step, we voltage bias the Josephson junction above the gap, to use it as a white noise source of photons which populates the resonator. In this shot noise regime, the statistics of the emitted radiation can be used as a characterization tool as it corresponds to a thermal bath of bunched photons : $g^{(2)}_{\mathrm{SN}}(0) = 2$.

2.1 Fast quadratic detector calibration

The fast quadratic detectors that we use (Herotek DTM 180AA) have a rising time of $\tau_R \sim 0.6\,\mathrm{ns}$, corresponding to a Lorentzian spectral response

$$F_{\mathrm{QD}}(\omega) = \frac{1}{1 + \left(\frac{f}{f_0}\right)^2}$$

where $f_0 = {}^{1}\!/_{2\pi\tau_R} \simeq 270\,\mathrm{MHz}$ is the frequency cut-off of the quadratic detector.

We estimate the influence of the quadratic detector on a flat signal with a 325 MHz bandwidth as we will measure it in our experiment. Due to the finite time response of the quadratic detector, it cannot catch all the dynamics of the signal, and we thus miss some correlations, as shown on Fig. 95.

The power associated to a signal with a $\Delta f = 600\,\mathrm{MHz}$ bandwidth is

$$P_0 = \int_0^{+\infty} d\omega P_N * P_N(\omega) = A_0^2 \int_0^{+\infty} d f \left(1 - \frac{f}{\Delta f}\right), \tag{87}$$

where A_0 is the amplitude of the signal. The power measured at the output of the quadratic detector is

$$P_{\mathrm{QD}} = \int_0^{+\infty} d\omega (P_N * P_N(\omega))\, F_{\mathrm{QD}}(\omega) = A_0^2 \int_0^{+\infty} d f \frac{1 - \frac{f}{\Delta f}}{1 + \left(\frac{f}{f_0}\right)^2} \tag{88}$$

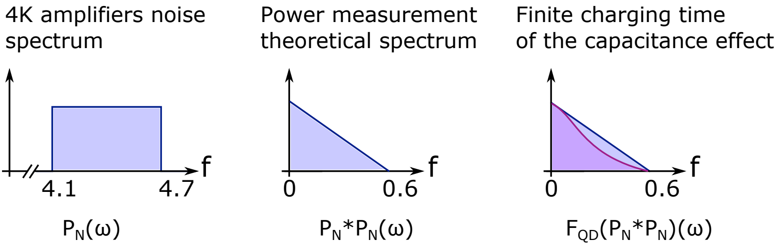

Figure 95. Shape of the initial signal, associated power and QD measurement result.

By taking the ratio between these two expressions, we can estimate the power that is not catched by the quadratic detectors.

To precisely compensate for this effect, we performed power measurement at the output of the quadratic detectors using the intrinsic noise of the amplifiers as shown in Fig.96.

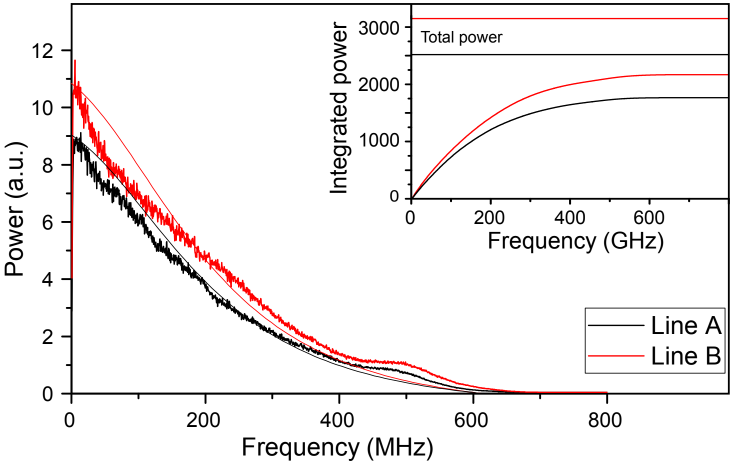

Figure 96. Spectrum at the output of the fast quadratic detector (bold line) and theoretical model (thin lines). Inset : associated power measurement and theoretical limit (horizontal lines)

Taking the ratio between the power at the output of Quadratic detector P_{QD} and the total power P_0, we find for the two lines,

$$K = \frac{P_{\mathrm{QD}}}{P_0} \sim 0.70.$$

As the number of sample required is directly related to $(\delta P / P)^{-4}$ according to Eq. 82, we have also performed correlation measurements with narrower $\Delta f = 325\,\mathrm{MHz}$ filters whose spectrum is shown Fig. 97.

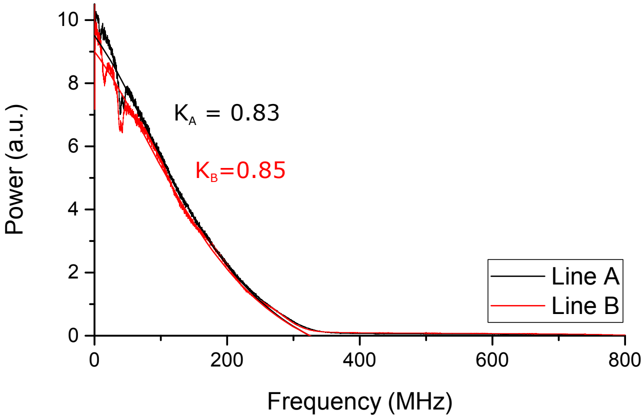

Figure 97. Spectrum at the output of the fast quadratic detector (bold line) and theoretical model (thin lines) for a filtering bandwidth $\Delta f = 325\,\mathrm{MHz}$.

The associated correlation factors yields $K = 0.84$. By reducing the bandwidth, we might loose some correlations but decrease the measurement time by a factor of 12.

2.2 Autocorrelation vs power measurements

According to section 2.2.1, the autocorrelation function of the signal coming out of line A takes the form

$$\langle A^\dagger A^\dagger A A\rangle = \\ G^2\langle c^\dagger c^\dagger c\, c\rangle + (G-1)^2\langle f_A^\dagger f_A^\dagger f_A f_A\rangle + 2G(G-1)\langle c^\dagger c\rangle\langle f_A^\dagger f_A\rangle. \tag{89}$$

As the gain of the amplifier is $G \gg 1$ and $\langle f^\dagger f\rangle \gg \langle c^\dagger c\rangle$, measuring the normalized difference with and without bias voltage applied to the sample yields

$$\frac{\mathrm{Auto}^B - \mathrm{Auto}^0}{\mathrm{Auto}^0} = 2\frac{\langle c^\dagger c\rangle}{\langle f^\dagger f\rangle} = 2\frac{P_S}{P_N}$$

In order to measure this ratio, we voltage bias the junction above the gap. The power emitted by the junction then increases linearly with the applied bias V and we extract the corresponding slopes. Measurements of the power and autocorrelation ratios are displayed in Fig. 98.

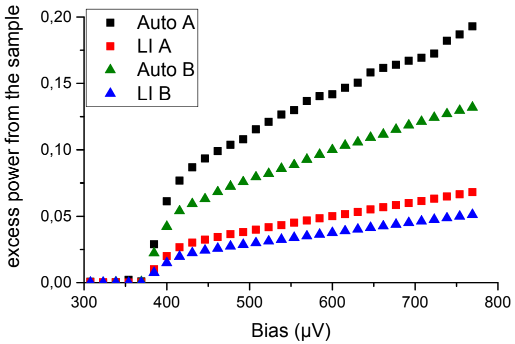

Figure 98. Excess power emitted in ShotNoise regime for the two measurement lines A, B. Comparison of autocorrelations from the acquisition board (red and black squares) and Lock-in measurements (blue and green triangles).

The ratio between autocorrelation and power measurements is slightly smaller than 2, as shown in Fig. 99. This is another consequence of the finite rising time of quadratic detectors which thus miss some autocorrelations.

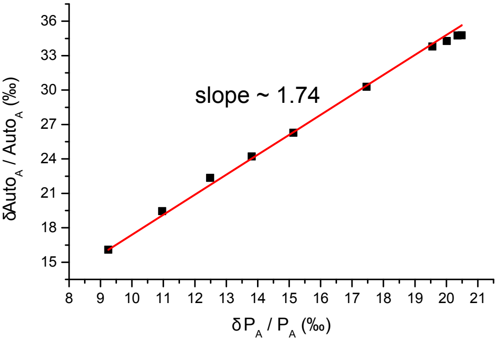

Figure 99. Ratio between autocorrelations ratio and excess power measurement ratio on line A.

By measuring the ratio s between ${}^{\delta\text{auto}}/_{\text{auto}}$ and ${}^{\delta P}/_{P}$ for a filtering bandwidth of 325 MHz, we found $s_A = 1.74$ on line A, as shown in Fig.99, and $s_B = 1.7$ on line B. These values yield to a correction factor of $K = s/2 \sim 0.86$, in agreement with the value estimated in section 2.1.

2.3 Distribution of the measured values

We measure the distribution of the values measured by the acquistion board. A typical histogram is shown in Fig. 100 together with a fit corresponding to rectified Gaussian fluctuations, combined with a small thermal rounding due to the amplifier after the quadratic detector (red curve).

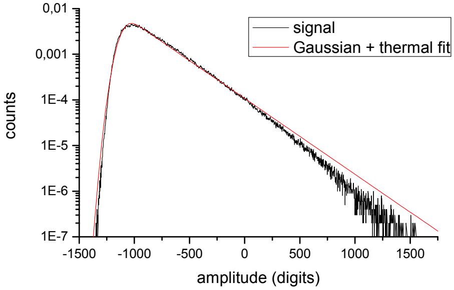

Figure 100. Histogram of the measurement of the acquisition card

We attribute the saturation observed at large values to the non-linearity of the quadratic detector. Note that the saturation of the last amplifier would have a similar effect. The tail of the curve which is slightly saturated accounts for ∼1‰ of the measured values.

These histograms are a quick tool to check that there is no significant saturation and that the dynamics of the board is properly used.

2.4 Correlation measurements in Shot Noise regime

When voltage biased well above the superconducting gap, the junction acts as a white noise source coupled to the resonator.

In this quasiparticle tunneling regime, the coupling factor r for Dynamical Coulomb Blockade effects is reduced by a factor 4. In addition, as the emitted power is high, the mean photon occupation number of the resonator is large and Dynamical Coulomb Blockade effects are negligible.

As a consequence, the properties of the emitted radiation corresponds to a thermal population of photons that are bunched, and with $g^{(2)}(0) = 2$. In addition, $g^{(2)}(\tau)$ tends to 1 after a time given by the inverse of the resonator bandwidth.

2.4.1 Time delay in Shot Noise regime

For experimental reasons, there is a small difference between the length of the two measurement lines, resulting in different propagation times. In order to compensate this shift, the origin of time delays between the two lines is adjusted by placing the origin at the maximum value. As $g^{(2)}$ is directly proportionnal to the cross-correlation function, we measure cross-correlations as function of time delay far above the gap to have the best signal to noise ratio, as shown in Fig. 101.

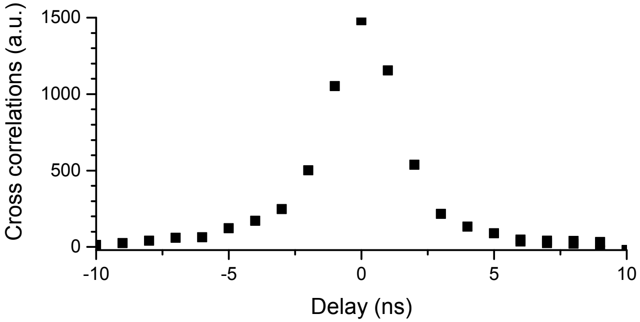

Figure 101. Cross-correlation function in Shot Noise regime as a function of the time delay.

The time delay is tuned by introducing a shift between the arrays of data corresponding to the two measurement lines.

2.4.2 calibration of $g^{(2)}(0)$ in Shot Noise regime

Time resolved measurements of the second order correlator $g^{(2)}(\tau)$ are presented in Fig. 102.

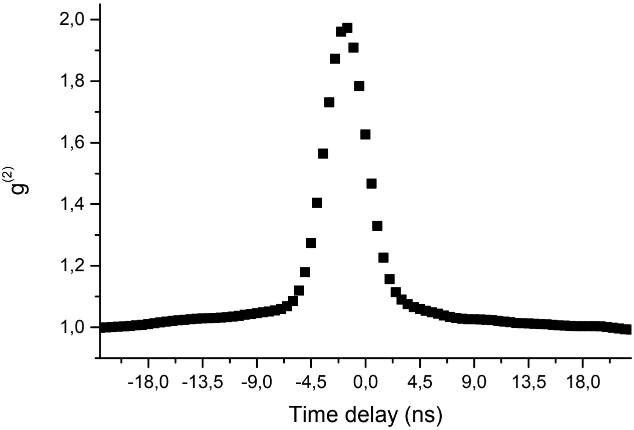

Figure 102. Time resolved second order correlator $g^{(2)}(\tau)$.

In the data processing using Eq. 86, we take $K = 0.72$ for the correction factor, as previously estimated for a wide filter bandwidth $\Delta f = 600\text{MHz}$. We obtained similar results for $g_{\text{SN}}^{(2)}(\tau)$ with the narrower 325 MHz filters. The maximum value of $g_{\text{SN}}^{(2)}(0) = 1.98$ is then in agreement with the theoretical prediction $g_{\text{SN}}^{(2)}(0) = 2$ for a thermal bath of photons.

In addition, as expected the FWHM is 4.5 ns which is comparable with the 7 ns photon lifetime in the resonator.

3 Statistics of emitted photons

We now characterize the statistics of the emitted radiation in the single photon emission peak. As described in chapter 2, Kubala *et al.* [51] made the following prediction for $g^{(2)}(0)$ at low photon occupancy in the resonator as a function of the coupling factor r

$$g^2(0) = \left(1 - \frac{r}{2}\right)^2 \sim 0.25. \tag{90}$$

which yields $g^2(0) = 0.25$ for our high impedance resonator $r \simeq 1$.

By varying the flux threading the SQUID, we can tune the Josephson energy E_J and thus the photon emission rate Γ. This allows us to adjust the average photon population $\langle n \rangle$ in the resonator

$$\langle n(E_J) \rangle = \frac{\Gamma(E_J)}{2\pi \Delta f}$$

where Δf is the FWHM of the resonator.

3.1 Evolution of $g^{(2)}(0)$ with the photon emission rate

We measure the second order correlator at zero time delay $g^{(2)}(0)$ as a function of the emission rate. The obtained results are shown in Fig. 103.

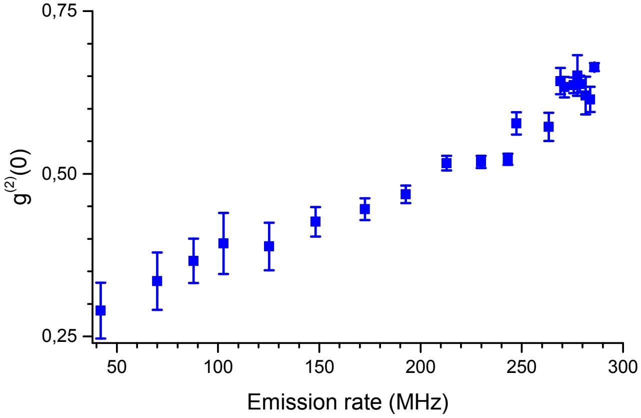

Figure 103. Second order correlator at zero time delay $g^{(2)}(0)$ as a function of the measured emission rate.

One first observes that $g^{(2)}(0) < 1$, meaning that the emitted photons have a non-classical behavior and are anti-bunched. Furthermore, the value obtained at the lowest rate is in good agreement with the predicted 0.25 theoretical limit [51].

Because of the saturation effect on the single photon emission peak presented in chapter 5, we were not able to increase the photon emission rate till correlation effects disappear, and $g^{(2)}(0) = 1$. Theoretical calculations are in progress to fit this curve (J. ankerhold, private communication).

The error bars on the curve of Fig. 103 take in account the statistical uncertainty. In order to reduce parasitic noise, we have first calibrated the chain and then removed the total power measurement associated with the lock-in detection chain. The autocorrelations ratio gave us access to the the emission rate and allowed us to calculate $g^{(2)}$ with an uncertainty within the error bar.

3.2 Time resolved correlator : $g^{(2)}(\tau)$

This measurement gives access to the timescale of correlations, as predicted in [20]

$$g^{(2)}(\tau) = \left(1 - \frac{r}{2} e^{-\gamma\tau/2}\right)^2, \tag{91}$$

where r is the coupling constant and $\gamma = 2\pi$ FWHM is the photon leakage of the resonator.

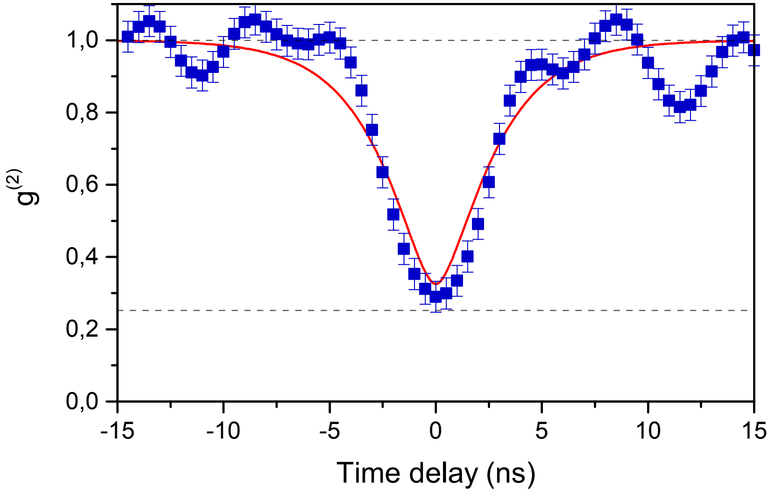

Figure 104. Time resolved evolution of the second order correlation factor $g^{(2)}(\tau)$ (blue) and theoretical fit using Eq. 91 from [20]. The horizontal lines correspond to the theoretical prediction $g^{(2)}(0) = 0.25$ and the long time limit $g^{(2)}(\tau) = 1$. For this measurement, the emission rate was tune to 42 MHz; we average over 2.10^{11}samples with a sampling rate of 2 GHz.

One first observes that the timescale over which $g^{(2)}(\tau)$ reaches one is in consistent with theoretical predictions [20]. The additionnal fluctuations that one can see on Fig. 104 corresponds to noise on the correlated signal.

Due to the finite rising time of quadratic detectors which average the $g^{(2)}(\tau)$ function over their rising time of 0.6 ns, there is an addintionnal rounding effect. We take in account this effect on the red curve which thus does not reach the theoretical limit.

7 Conclusion

In this Ph.D., I have developed high impedance microwave resonators, with characteristic impedances Z_C around 2kΩ. These resonators, based on spiral inductors micro-fabricated on quartz substrate allowed us to reach a strong coupling to a Josephson junction as their impedance becomes scalable with R_Q is the superconducting quantum of resistance. This coupling is characterized by

$$r = \frac{\pi Z_C}{R_Q} = 1,$$

and corresponds to a regime that has not been previously explored in such systems.

By modulating the flux threading the SQUID loop, used as a tunable Josephson junction, we can tune the Josephson coupling E_J between the electrodes. This allows us to observe the transition between the low coupling regime, well accounted for by the $P(E)$ theory and its extensions, and the strong coupling regime, whose description requires to go beyond the $P(E)$ theory. In particular, we observed enhanced emission in multiphoton processes as well as the breakdown of the E_J^2 scaling rule for 1 and 2 photon emission peaks.

Then, focusing on the single photon emission peak, this strong coupling allowed us to probe a spectacular prediction of Joachim Ankerhold and his coworkers [51]: when the junction is biased at a voltage chosen so that the energy of a Cooper pair transmitted across the junction matches the energy of a photon in the resonator, the presence of a photon inhibits the subsequent tunneling of a Cooper pair and the emission of another photon. This results in a strong anti-bunching of the emitted radiation.

We characterized this anti-bunching by measuring $g^{(2)}(\tau)$ the time resolved second order coherence function of the radiation leaked by the resonator into a $50\,\Omega$ detection environment. To do so, we used an Hanburry-Brown set-up which allows to get rid of the noise of the detection amplifier. In the low Josephson energy, the zero time second order coherence function reaches $g_2(0) = 0.25 \pm 0.1$, in good agreement with the theoretical predictions. As expected, $g_2(\tau)$ reaches 1 with a typical time scale corresponding to the lifetime of photons in the resonator. At higher Josephson energy, $g_2(0)$ increases to reach 0.7, and we observe a saturation of the number of photons in the resonator which is due to the strong fluctuations of the phase induced by our strong coupling regime.

One of the perspectives of this work in to further increase the impedance of the modes by further decreasing their capacitance, using SiN membranes instead of Quartz substrate [26]. This should allow us to reach a characteristic impedance of 4.1 kΩ, for which one expects a perfect anti-bunching. This will allow to take a further step, building on an idea developed by Ash Clerk and his colleagues [72] to stabilize a $N = 1$ Fock state in the resonator. To reach this, achieving $g_2(0) = 0$ is not sufficient: although the presence of a photon in the resonator completely suppresses the emission of another photon, it is still possible for a Cooper pair to tunnel back-wards, re-absorbing the photon. To suppress this process, we will couple a junction to two modes, a high impedance, high quality factor one, and a low impedance, low quality factor one. Then we will bias the junction at a voltage chosen so that the energy of a Cooper pair transmitted through the junction matches the sum of the energies of a photon in the two modes. After a Cooper pair tunnels and emits a photon in either modes, the low quality factor mode loses its photon quickly, prohibiting the backward emission of a Cooper pair, thus stabilizing the $N = 1$ state in the high impedance mode.

Another interesting direction would be to probe the two photon processes: upon increasing the Josephson energy, the photon number in the resonator increases, and stimulated emission processes result in a parametric transition analogous to the one observed in a two photon micro-maser [63]. This transition is marked by a a divergence of the fluctuations of the photon number at the transition. It has been predicted that in the strong coupling regime, the transition is smeared by the quantum fluctuations of the phase, suppressing this divergence.

Beyond these possibilities, an exciting perspective of our high impedance resonators open is the ability to investigate experimentally the influence of strong quantum fluctuations of the phase on the Josephson Hamiltonian itself. Indeed, the Josephson Hamiltonian $H_J = -E_J \cos\phi$

can be derived from the standard tunneling Hamiltonian $H_T = e^{i\phi/2} \sum t_{l,r,\sigma}\, c_{l,\sigma}^{\dagger}\, c^{r,\sigma}$ + h.c. . If the left and right electrodes are in a superconducting state characterized by a gap Δ, one then rewrites the normal quasi-particle creation and annihilation operators $c_{l,,r,\sigma}^{\dagger}$ and $c^{l,r,\sigma}$ in terms of Bogoliubov operators. One thus recovers the standard Josephson Hamiltonian, with the Josephson energy related to the normal tunneling resistance via R_t the Ambegaokar-Baratoff formula:

$$E_J = \frac{\Delta\, R_Q}{2\, R_t}$$

, where $R_Q = h/4\,e^2$ is the superconducting resistance quantum. However, in this derivation, the phase ϕ across the junction is supposed to be a classical quantity, and it is not clear whether this Hamiltionian still holds in presence of large quantum phase fluctuations, especially if their frequency is higher than the gap frequency Δ/h.

One of the most appealing aspects of our resonators is that they should sustain a moderate in plane magnetic field, making their use compatible with semiconductors 2D electron gas (2DEG). Coupling such resonators to a normal quantum point contacts or quantum dot would allow us to probe the physics of dynamical Coulomb Blockade for normal conductors with arbitrary electronic transmission, for which no full theory is available yet [10][28]. Furthermore, using high spin-orbit coupling materials such as the ones I used in IEMN would allow to lift the spin degeneracy, thus making the problem simpler from a theoretical point of view [21].

Last, coupling such resonators with InAlAs nanowires connected to superconducting electrodes would allow us to probe the Coulomb Blockade of multiple Andreev reflections.

In a nutshell, the experiments performed during this thesis work are examples of the many possibilities enabled by high impedance resonators, giving access to a new regime of quantum optics.

Bibliography

[1] C. Altimiras, F. Portier, and P. Joyez. Interacting Electrodynamics of Short Coherent Conductors in Quantum Circuits. *Physical Review X*, 6(3):31002, 2016.

[2] Carles Altimiras, Olivier Parlavecchio, Philippe Joyez, Denis Vion, Patrice Roche, Daniel Esteve, and Fabien Portier. Dynamical Coulomb Blockade of Shot Noise. *Physical Review Letters*, 112(23):236803, 2014.

[3] Vinay Ambegaokar and Alexis Baratoff. Tunneling Between Superconductors. *Physical Review Letters*, 10(11):486–489, 1963.

[4] J. A. Appelbaum. Tunneling in Solids. C. B. Duke. Academic Press, New York, 1969. xii + 356 pp. illus. $16. Solid State Physics, supplement 10. *Science*, 167(3922):1244–1244, feb 1970.

[5] Alain Aspect, Philippe Grangier, and Gérard Roger. Experimental Tests of Realistic Local Theories via Bell's Theorem. *Physical Review Letters*, 47(7):460–463, 1981.

[6] Dv Averin and Kk Likharev. Coulomb Blockade of Single-Electron Tunneling, and Coherent Oscillations. *Journal of Low Temperature Physics*, 62(3-4):345–373, feb 1986. WOS:A1986A232700010.

[7] Girish S. Agarwal. *Quantum Optics*. Cambridge University Press, Cambridge, UK, 1 edition edition, dec 2012.

[8] J. Bardeen, L. N. Cooper, and J. R. Schrieffer. Theory of Superconductivity. *Physical Review*, 108(5):1175–1204, 1957.

[9] C. W. J. Beenakker and H. Schomerus. Counting Statistics of Photons Produced by Electronic Shot Noise. *Physical Review Letters*, 86(4):700–703, jan 2001.

[10] C. W. J. Beenakker and H. Schomerus. Antibunched Photons Emitted by a Quantum Point Contact out of Equilibrium. *Physical Review Letters*, 93(9):96801, aug 2004.

[11] Ya. M. Blanter and M. Büttiker. Shot noise in mesoscopic conductors. *Physics Reports*, 336(1–2):1–166, sep 2000.

[12] N.N. Bogoliubov, V. Tolmachev, and D. Shirkov. A new method in theory of superconductivity. *Journal of Experimental and Theoretical Physics*, 7(1):41, 1958.

[13] Christophe Brun, Konrad H. Müller, I.-Po Hong, François Patthey, Christian Flindt, and Wolf-Dieter Schneider. Dynamical Coulomb Blockade Observed in Nano-Sized Electrical Contacts. *Physical Review Letters*, 108(12), mar 2012. ArXiv: 1006.0333.

[14] M. Buttiker and R. Landauer. Traversal time for tunneling. *IBM Journal of Research and Development*, 30(5):451–454, sep 1986.

[15] M. Büttiker. Scattering theory of current and intensity noise correlations in conductors and wave guides. *Physical Review B*, 46(19):12485–12507, nov

1992.

[16] A. O Caldeira and A. J Leggett. Quantum tunnelling in a dissipative system. *Annals of Physics*, 149(2):374–456, sep 1983.

[17] Carlton M. Caves. Quantum limits on noise in linear amplifiers. *Physical Review D*, 26(8):1817–1839, oct 1982.

[18] A. N. Cleland, J. M. Schmidt, and John Clarke. Charge fluctuations in small-capacitance junctions. *Physical Review Letters*, 64(13):1565–1568, mar 1990.

[19] A. N. Cleland, J. M. Schmidt, and John Clarke. Influence of the environment on the Coulomb blockade in submicrometer normal-metal tunnel junctions. *Physical Review B*, 45(6):2950–2961, 1992.

[20] Simon Dambach, Björn Kubala, Vera Gramich, and Joachim Ankerhold. Time-resolved statistics of nonclassical light in Josephson photonics. *Physical Review B*, 92(5):54508, 2015.

[21] María de la Mata, Renaud Leturcq, Sébastien R. Plissard, Chloé Rolland, César Magén, Jordi Arbiol, and Philippe Caroff. Twin-Induced InSb Nanosails: A Convenient High Mobility Quantum System. *Nano Letters*, 16(2):825–833, feb 2016.

[22] P. Delsing, K. K. Likharev, L. S. Kuzmin, and T. Claeson. Effect of high-frequency electrodynamic environment on the single-electron tunneling in ultrasmall junctions. *Physical Review Letters*, 63(11):1180–1183, sep 1989.

[23] M. H. Devoret, D. Esteve, H. Grabert, G.-L. Ingold, H. Pothier, and C. Urbina. Effect of the electromagnetic environment on the Coulomb blockade in ultrasmall tunnel junctions. *Physical Review Letters*, 64(15):1824–1827, 1990.

[24] Michel H. Devoret. Quantum fluctuations in electrical circuits. 1995.

[25] G. J. Dolan. Offset masks for lift-off photoprocessing. *Applied Physics Letters*, 31(5):337–339, sep 1977.

[26] J. M. Fink, M. Kalaee, A. Pitanti, R. Norte, L. Heinzle, M. Davanço, K. Srinivasan, and O. Painter. Quantum electromechanics on silicon nitride nanomembranes. *Nature Communications*, 7:12396, aug 2016.

[27] Jean-Charles Forgues, Christian Lupien, and Bertrand Reulet. Experimental Violation of Bell-like Inequalities By Electronic Shot Noise. *Physical Review Letters*, 114(13):130403, 2015.

[28] I. C. Fulga, F. Hassler, and C. W. J. Beenakker. Nonzero temperature effects on antibunched photons emitted by a quantum point contact out of equilibrium. *Physical Review B*, 81(11):115331, mar 2010.

[29] D. A. Gandolfo, A. Boornard, and L. C. Morris. Superconductive Microwave Meander Lines. *Journal of Applied Physics*, 39(6):2657–2660, may 1968.

[30] Gabriel Gasse, Christian Lupien, and Bertrand Reulet. Observation of Squeezing in the Electron Quantum Shot Noise of a Tunnel Junction. *Physical Review Letters*, 111(13):136601, sep 2013.

[31] L. J. Geerligs, V. F. Anderegg, C. A. van der Jeugd, J. Romijn, and J. E. Mooij. Influence of Dissipation on the Coulomb Blockade in Small Tunnel Junctions. *EPL (Europhysics Letters)*, 10(1):79, 1989.

[32] S. M. Girvin, L. I. Glazman, M. Jonson, D. R. Penn, and M. D. Stiles. Quantum fluctuations and the single-junction Coulomb blockade. *Physical Review Letters*, 64(26):3183–3186, 1990.

[33] D. C. Glattli, J. Gabelli, L.-H. Reydellet, G. Fève, J. M. Berroir, B. Plaçais, and P. Roche. Hanbury Brown and Twiss Noise Correlations to Probe the Statistics of GHz Photons Emitted by Quantum Conductors. In *AIP Conference Proceedings*, volume 780, pages 466–471. AIP Publishing, aug 2005.

[34] Roy J. Glauber. Coherent and Incoherent States of the Radiation Field. *Physical Review*, 131(6):2766–2788, sep 1963.

[35] K. Gloos, R. S. Poikolainen, and J. P. Pekola. Wide-range thermometer based on the temperature-dependent conductance of planar tunnel junctions. *Applied Physics Letters*, 77(18):2915–2917, oct 2000.

[36] H Grabert, G.-L Ingold, and B Paul. Phase diffusion and charging effects in Josephson junctions. *Europhysics Letters (EPL)*, 44(3):360–366, nov 1998.

[37] Vera Gramich, Björn Kubala, Selina Rohrer, and Joachim Ankerhold. From Coulomb-Blockade to Nonlinear Quantum Dynamics in a Superconducting Circuit with a Resonator. *Physical Review Letters*, 111(24):247002, 2013.

[38] Hermann Grabert and Michel H. Devoret, editors. *Single Charge Tunneling*, volume 294 of *NATO ASI Series*. Springer US, Boston, MA, 1992.

[39] R. Hanbury Brown and R. Q. Twiss. A Test of a New Type of Stellar Interferometer on Sirius. *Nature*, 178(4541):1046–1048, nov 1956.

[40] H. A. Haus and J. A. Mullen. Quantum Noise in Linear Amplifiers. *Physical Review*, 128(5):2407–2413, 1962.

[41] M. Hofheinz, F. Portier, Q. Baudouin, P. Joyez, D. Vion, P. Bertet, P. Roche, and D. Esteve. Bright Side of the Coulomb Blockade. *Physical Review Letters*, 106(21):217005, may 2011.

[42] T. Holmqvist, M. Meschke, and J. P. Pekola. Double oxidation scheme for tunnel junction fabrication. *Journal of Vacuum Science & Technology B*, 26(1):28–31, jan 2008.

[43] T. Holst, D. Esteve, C. Urbina, and M. H. Devoret. Effect of a Transmission Line Resonator on a Small Capacitance Tunnel Junction. *Physical Review Letters*, 73(25):3455–3458, 1994.

[44] C. K. Hong, Z. Y. Ou, and L. Mandel. Measurement of subpicosecond time intervals between two photons by interference. *Physical Review Letters*, 59(18):2044–2046, nov 1987.

[45] Serge Haroche and Jean-Michel Raimond. *Exploring the Quantum: Atoms, Cavities, and Photons*. Oxford University Press, Oxford ; New York, 1 edition edition, oct 2006.

[46] Gert-Ludwig Ingold and Yu V. Nazarov. Charge Tunneling Rates in Ultrasmall Junctions. In *Single Charge Tunneling*, volume 294 of *NATO ASI Series*, pages 21–107. Plenum press, Boston Ma, 1992. ArXiv: cond-mat/0508728.

[47] R. C. Jaklevic, John Lambe, A. H. Silver, and J. E. Mercereau. Quantum Interference Effects in Josephson Tunneling. *Physical Review Letters*, 12(7):159–160, 1964.

[48] B. D. Josephson. Possible new effects in superconductive tunnelling. *Physics Letters*, 1(7):251–253, 1962.

[49] P. Joyez and D. Esteve. Single-electron tunneling at high temperature. *Physical Review B*, 56(4):1848–1853, 1997.

[50] Philippe Joyez. Self-Consistent Dynamics of a Josephson Junction in the Presence of an Arbitrary Environment. *Physical Review Letters*, 110(21):217003, may 2013.

[51] Björn Kubala, Vera Gramich, and Joachim Ankerhold. Non-classical light from superconducting resonators coupled to voltage-biased Josephson junctions. *Physica Scripta*, 2015(T165):14029, 2015.

[52] Rolf Landauer. Electrical resistance of disordered one-dimensional lattices. *Philosophical Magazine*, 21:863–867, 1970.

[53] J. Leppäkangas, G. Johansson, M. Marthaler, and M. Fogelström. Input–output description of microwave radiation in the dynamical Coulomb blockade. *New Journal of Physics*, 16(1):15015, 2014.

[54] Juha Leppäkangas, Mikael Fogelström, Alexander Grimm, Max Hofheinz, Michael Marthaler, and Göran Johansson. Antibunched Photons from Inelastic Cooper-Pair Tunneling. *Physical Review Letters*, 115(2):27004, 2015.

[55] Juha Leppäkangas, Göran Johansson, Michael Marthaler, and Mikael Fogelström. Nonclassical Photon Pair Production in a Voltage-Biased Josephson Junction. *Physical Review Letters*, 110(26):267004, 2013.

[56] Rodney Loudon. *The Quantum Theory of Light*. Oxford University Press, Oxford ; New York, 3 edition edition, nov 2000.

[57] L. MANDEL and E. WOLF. Coherence Properties of Optical Fields. *Reviews of Modern Physics*, 37(2):231–287, 1965.

[58] Rohat Melik and Hilmi Volkan Demir. Implementation of high quality-factor on-chip tuned microwave resonators at 7 GHz. *Microwave and Optical Technology Letters*, 51(2):497–501, 2009.

[59] S. S. Mohan, M. del Mar Hershenson, S. P. Boyd, and T. H. Lee. Simple accurate expressions for planar spiral inductances. *IEEE Journal of Solid-State Circuits*, 34(10):1419–1424, oct 1999.

[60] Leonard Mandel and Emil Wolf. *Optical Coherence and Quantum Optics*. Cambridge University Press, sep 1995. Google-Books-ID: FeBix14iM70C.

[61] Yuli V. Nazarov and Yaroslav M. Blanter. *Quantum Transport: Introduction to Nanoscience*. Cambridge University Press, may 2009. Google-Books-ID: YNr4OcCExUcC.

[62] Philippe Nozieres and David Pines. *Theory of Quantum Liquids*. Sceince and advanced math. Westview press edition, oct 1999.

[63] Ciprian Padurariu, Fabian Hassler, and Yuli V. Nazarov. Statistics of radiation at Josephson parametric resonance. *Physical Review B*, 86(5):54514, 2012.

[64] O. Parlavecchio, C. Altimiras, J.-R. Souquet, P. Simon, I. Safi, P. Joyez, D. Vion, P. Roche, D. Esteve, and F. Portier. Fluctuation-Dissipation Relations of a Tunnel Junction Driven by a Quantum Circuit. *Physical Review Letters*, 114(12):126801, mar 2015.

[65] Olivier Parlavecchio. *Dynamical Coulomb Blockade: from electronic fluctuations to quantum microwaves, PHD Thesis*. PhD thesis, unviersité Pierre et Marie Curie, 2015.

[66] Frederic Pierre. *Interaction électron-électron dans les fils mésoscopiques*. PhD thesis, Paris VI, Saclay, 2000.

[67] David M. Pozar. *Microwave Engineering*. John Wiley & Sons, Hoboken, NJ, 4th Revised edition edition edition, dec 2011.

[68] L.-H. Reydellet. *Bruit quantique electronique et photons micro-ondes*. PhD thesis, Université Pierre et Marie Curie - Paris VI, 2003.

[69] D Rogovin and D. J Scalapino. Fluctuation phenomena in tunnel junctions. *Annals of Physics*, 86(1):1–90, 1974.

[70] W. Schottky. Über spontane Stromschwankungen in verschiedenen Elektrizitätsleitern. *Annalen der Physik*, 362(23):541–567, jan 1918.

[71] Gerd Schön and A. D. Zaikin. Quantum coherent effects, phase transitions, and the dissipative dynamics of ultra small tunnel junctions. *Physics Reports*, 198(5):237–412, 1990.

[72] J.-R. Souquet and A.A. Clerk. Fock-state stabilization and emission in superconducting circuits using dc-biased Josephson junctions. *Physical Review A*, 93(6):60301, 2016.

[73] Marlan O. Scully and M. Suhail Zubairy. *Quantum Optics*. Cambridge University Press, sep 1997. Google-Books-ID: 20ISsQCKKmQC.

[74] Ingo Wolff. *Wiley: Coplanar Microwave Integrated Circuits - Ingo Wolff*. Wiley edition, 2006.

[75] B. Yurke. Input-Output Theory. In Professor Peter D. Drummond and Dr Zbigniew Ficek, editors, *Quantum Squeezing*, number 27 in Springer Series on Atomic, Optical, and Plasma Physics, pages 53–96. Springer Berlin Heidelberg, 2004. DOI: 10.1007/978-3-662-09645-1_3.

[76] Bernard Yurke and John S. Denker. Quantum network theory. *Physical Review A*, 29(3):1419–1437, mar 1984.

[77] E. Zakka-Bajjani, J. Ségala, F. Portier, P. Roche, D. C. Glattli, A. Cavanna, and Y. Jin. Experimental Test of the High-Frequency Quantum Shot Noise Theory in a Quantum Point Contact. *Physical Review Letters*, 99(23):236803, 2007.

[78] Eva Zakka-Bajjani, J. Dufouleur, N. Coulombel, P. Roche, D. C. Glattli, and F. Portier. Experimental Determination of the Statistics of Photons Emitted by a Tunnel Junction. *Physical Review Letters*, 104(20):206802, 2010.